Crossing the scales: From microscopic neuronal dynamics to macroscopic brain activity

D I S S E R T A T I O N

zur Erlangung des akademischen Grades

doctor rerum naturalium
(Dr. rer. nat.)
im Fach Biophysik

eingereicht an der
Mathematisch-Naturwissenschaftlichen Fakultät I
der Humboldt-Universität zu Berlin

von
M.Sc. Bartosz Marek Teleńczuk

Präsident der Humboldt-Universität zu Berlin:
Prof. Dr. Jan-Hendrik Olbertz

Dekan der Mathematisch-Naturwissenschaftlichen Fakultät I:
Prof. Dr. Andreas Herrmann

Gutachter:
1. Prof. Dr. Gabriel Curio
2. Prof. Dr. Andreas Herz
3. Prof. Dr. Richard Kempter

Tag der mündlichen Prüfung: 27.09.2011

Abstract

During its normal function the brain generates strong and measurable electric signals. This phenomenon, which has been known for more than a century, makes it possible to investigate the signal processing in the brain. Nowadays the cellular processes taking part in the generation of the electric signals are well understood. However, most of the neuronal events recruit large populations of cells, whose activities are coordinated spatially and temporally. This coordination allows for summation of activities generated by many neurons leading to extracellular electric signals that can be recorded non-invasively from the scalp by means of electroencephalography (EEG). The temporal structure of the EEG signal does not depend only on the properties of single neurons, but also on their interactions that may be very complex. The complexity hinders the evaluation of the recoded signal with respect to the number of active neurons, the type of response, the degree of synchronisation and the contribution of other processes (such as, learning and attention). In the thesis, the relations between the microscopic (single-neuron) and their macroscopic (EEG) properties will be investigated by means of experimental, data-analytic and theoretical approaches.

Zusammenfassung

Während seiner normalen Funktion generiert das Gehirn starke elektrische Signale, die technisch gemessen werden können. Das schon seit über einem Jahrhundert bekannte Phänomen ermöglicht es die Signalverarbeitung im Gehirn räumlich und zeitlich zu beobachten. Heute versteht man die zellulären Prozesse die zur Generierung der elektrischen Signale in einzelnen Neuronen führen. Jedoch rekrutieren die meisten neuronalen Ereignisse große Populationen von Zellen, dessen Aktivität zeitlich und räumlich koordiniert ist. Diese Koordinierung führt dazu, dass ihre elektrische Aktivität auch weit von den Quellen gemessen werden kann, sodass die Beobachtung des Gehirns auch nicht invasiv auf der Schädeloberfläche mittels dem sogenannten Elektroenzephalogramm (EEG) möglich ist. Der zeitliche Verlauf des Signals hängt nicht nur von den Eigenschaften einzelner Zellen ab sondern auch von ihrer Wechselwirkung mit anderen Neuronen, die oft komplex oder gar nicht bekannt ist. Diese Komplexität verhindert die Auswertung der gemessen Signale im Bezug auf die Anzahl von aktiven Neuronen, die Art der Antwort (Inhibition, Exzitation), die Synchronisationsstärke und den Einfluss anderer aktiver Prozesse (wie zum Beispiel: Lernen, Aufmerksamkeit usw.). In dieser Arbeit werden die Zusammenhänge zwischen diesen mikroskopischen Parametern (einzelne Neurone) und ihrer makroskopischen Wirkung (EEG) experimentell, datenanalytisch und theoretisch untersucht.

Im ersten Kapitel werden die physikalische Prozesse die zur Generierung von elektrischen EEG Potenzialen an der Kopfhaut führen qualitativ und quantitativ beschrieben. Aus dieser grundlegenden Beschreibung folgen wichtige Konsequenzen für die EEG-Amplitude und die relativen Beiträge verschiedener neuronaler Prozesse zum Gesamtsignal. Unter anderem wird gezeigt wie viele Neurone aktiv sein müssen damit ihre unterschwelligen und überschwelligen Signale auf der Kopfhaut nachweisbar sind.

Die neuronale Signalverarbeitung wird oft durch wiederholte Präsentation von gleichen sensorischen Reizen untersucht. Die Annahme hinter dieser Methode ist, dass für bestimmte Stimuli die Neurone eine bestimmte Antwort generieren weswegen man die Signale über mehrere Präsentationen mitteln darf. Im zweiten Kapitel wird eine Einzelreiz Analyse durchgeführt, in der die Spike-Burst Antworten von Einzelzellen beim Affen auf der Basis heterogener Binnenstrukturen untersucht werden. Durch verschiedene Klassifizierungsverfahren stellt sich heraus, dass die neuronalen Antworten auf den gleichen Stimulus sehr variable sind, aber die gesamte Variabilität aus wenigen stereotypierten Klassen (Spike Mustern), die abwechselnd auftreten, besteht.

Die niederfrequenten Komponenten des EEGs werden hauptsächlich durch die Sumation von unterschwelligen synaptischen Potenziale wie EPSPs/IPSPs ("excitatory/ inhibitory post-synaptic potentials") generiert. Das hat die Folge dass die tatsächlichen Ausgaben der neuronalen Verarbeitung, nämlich die Aktionspotenziale (Spikes) nicht direkt im EEG ausgeprägt sind. Hingegen wurde gezeigt, dass die durch elektrische Stimulation von Nervus Medianus evozierten hochfrequenten EEG Oszillationen (> 600 Hz, hf-EEG) kollektiv synchronisierte Spikes (so genannte "population bursts") darstellen. Hinausgehend, im Kapitel 3 zeigen wir dass die Amplitude von hf-EEG eine Funktion der in Cluster gruppierten

spike-burst Antworten ist. Dieser Aspekt ist insbesondere von hoher Revelanz, da er grundlegend für die Verknüpfung des invasiven hf-EEG mit den Details kortikaler Spike-Antworten sein kann.

Die ungewöhnlichen Korrelationen zwischen einzelzelligen Spike Mustern und hf-EEG Oszillationen wird mit theoretischen Mitteln in Kapitel 4 weiter analysiert. Zu diesem Zweck wird ein vereinfachtes Modell von einzelnen Zellen entwickelt das sehr genau, sowohl die experimentell bestimmten gemittelten Antworten, als auch die Einzellreiz-Statistik abbildet. Eine Simulation des Modells in der der durchschnittliche synaptische Eingang langsam variiert wird, zeigt dass die oben genannte Korrelation auch durch intrakortikale Prozesse (wie zum Beispiel Aufmerksamkeit) generiert werden kann.

Im Kapitel 5 wird der Zusammenhang zwischen mikroskopischer und makroskopischer neuronaler Dynamik auf abstrakter Ebene weiter untersucht. Insbesondere, wird weiter gezeigt dass die Kopplung zwischen einzelnen neuronalen Elementen eine grundlegende Auswirkung auf die evozierten EEG Potenziale ("evoked responses", ERs) hat in dem sie es ermöglicht zwei verschiedene Arten der ER-Generierung in einem Modell darzustellen. Dieser Formalismus schafft eine Einigung von bislang entgegengesetzten Ergebnisse die in der wissenschaftlichen Literatur veröffentlicht wurden.

Zusammengefasst verbessert die Kombination von drei verschieden Ansätzen, dem experimentellen, datenanalytischen und theoretischen, unser Verständnis für die Zusammenhänge zwischen Einzelzelleaktivitäten und deren makroskopischen Korrelaten (EEG) und eröffnet dabei die Möglichkeit die neuronale Signalverarbeitung nichtinvasiv am Menschen zu untersuchen.

Contents

1. Introduction

Recall the last time you were on a walk in a forest. If you watched the surroundings carefully, you may have pondered on the diversity of tree species and their forms, looked out for birds singing in the canopy or even, with a bit of luck, glimpsed a herd of deer grazing on a hidden meadow. And while you admired the beauty and complexity of nature, you might still miss the abundance of life just below your feet or within the reach of your hand. If you had looked closer you would have probably seen a group of ants carrying food to their nest, a sprouting tree searching for a ray of light and a multitude of lichens on the nearby tree trunk, which in themselves are a complex symbiosis of several organisms. On the other hand, if you could look at the same forest from far above, you would see it still differently. You might then see a patch-like distribution of trees which adapt to local availability of natural resources or the signs of a fire that destroyed a large area of the forest decades ago.

This everyday example shows that we are predisposed to observe objects of dimensions not much different from our own and to events that happen at familiar time scales: minutes, hours or days. However, the ecosystem we belong to consists of nested temporal and spatial scales: from the microscopic world of cells, which build all living organisms, through complex interactions between fauna and flora to the whole ecosystem, which may cross the political and ethnic boundaries. In order to understand the ecosystem as a whole, we need to understand how the complexities at one of its scales emerge from the properties of those below it.

Similarly, levels of organisation of neural systems form a hierarchy. At its finest scale we can look into the dynamics of single ions: how they move and interact. At this level we may describe a number of phenomena using just the basic laws of physics. However, such a description would be too detailed to study some of the most fundamental problems of neuroscience, such as: what is the neural code, how memories are stored or what are the neural correlates of conciousness. At the other end of the hierarchy one could focus only on the "inputs" and "outputs" of the nervous system: the external stimuli and the behaviours. Based on the relation between the inputs and outputs, one could map sensory signals to motor commands, but without an appreciation of the neuronal events underlying the process. Neither the description at high nor at low levels of neural organisation alone can bring the complete view on the function of real neural systems.

In order to understand the brain in all its details, neuroscientists investigate it at all organization levels. They do it the same way you might have observed the forest: they match the level of their description to the scale of their measurement tools, which are, in a way, their "augmented senses". Most mechanistic theories of neural systems, such as membrane theory and neural coding, describe microscopic properties of neural

tissue studied in vitro or in vivo in animal models. On the other hand, most of our knowledge of the operation of the human brain concerns the level of macroscopic brain structures investigated with non-invasive techniques. Unfortunately, both fields stay separated from each other with moderate cross-communication. One of the reasons behind it is that experts working in those separate areas use very specific experimental methods optimised for the scale of their favourite system. So far there is little knowledge about relations between tools at microscopic and macroscopic scales. How do they differ? Which neuronal processes are they sensitive to? Under what conditions are they comparable? Is it possible to draw conclusions about processes happening at one of the scales from the findings about the other? These are some of the questions that we will try to answer in the present work.

Along the way we will take an integrative approach combining experiments, data analysis and neural modelling. We believe that putting these three elements on an equal footing will help us to address the questions and this way to bridge the gap between the microscopic scale of single neurons and macroscopic scale of a functional brain.

In this chapter we start with a brief overview of the experimental methods used to investigate neural systems at microscopic and macroscopic scales. We compare the spatial and temporal resolutions of these methods, present the basis of their generation in theoretical terms and finally discuss the main neuronal processes they correlate with. We finish the introduction with a description of experimental methods that were used to collect the data from the primary somatosensory cortex of macaque monkeys – the main neural system that is investigated in this thesis.

In Chapter 2 we study the system at the microscopic scale. To this end, we analyse the responses of single cortical neurons to peripheral stimulation of the median nerve. We show that the responses even to identical stimuli are highly variable. Next, we demonstrate that the variability may be described by means of a few temporal spike patterns that reoccur in the stimulation train. The discussion is concluded with general remarks on the mechanisms of spike pattern generation.

In Chapter 3 we move to the macroscopic level of neuronal responses and analyse high-frequency activity recorded with electrodes placed on the dura above the somatosensory cortex (high-frequency electroencephalogram, hf-EEG). This activity is shown to be closely related to the timing of action potentials in the cortex. We apply single-trial analysis to quantify the trial-to-trial variability of hf-EEG amplitudes. Next, we investigate the relation between the microscopic single-cell and the macroscopic hf-EEG activity, and we find that a significant fraction of the hf-EEG variability may be explained by the spike-pattern variations. We close the chapter with a general discussion of possible mechanisms behind the co-variations between these spatial scales.

We test one of the hypotheses regarding the mechanisms of single-cell and hf-EEG co-variation in Chapter 4. To this end, we develop a model of single-neuron activity and show that it reproduces well the previously-described shape and distribution of experimental spike patterns. From this model we derive numerically the expected

population responses and demonstrate that they correlate well with the hf-EEG estimated experimentally.

In Chapter 5 we discuss the relations between stimulus-evoked macroscopic activity recorded non-invasively and the underlying microscopic properties in more general terms. Using computer simulations and theoretical considerations we derive the conditions under which findings at macroscopic level can be translated directly to the microscopic level and identify the level of spatial synchrony between the microscopic neuronal sources as a crucial parameter determining the discrepancy between both scales.

1.1. Eavesdropping on in vivo neurons

The human brain consists of about 10^{12} neurons whose collective activity creates complex human behaviours, encodes human feelings and may be the correlate of conscious experience. To understand how these phenomena emerge from the neuronal structure would require one to record simultaneously from a substantial number of neurons of diverse types localised in widespread anatomical areas of a working brain. Therefore the progress in neuroscience is closely related to the search for the optimal recording technique, a "virtual electrode". The hypothetical "virtual electrode" should have the following properties:

- large number of independent recording channels,
- high spatial and temporal resolution,
- ability to record from an intact human brain,
- high specificity to the activity of selected cells,
- direct access to membrane potential fluctuations and other state variables.

An intensive engineering effort has brought about a multitude of different methods based on various physical principles, but none of them implements all of the properties of the "virtual electrode". Each method has its advantages and shortcomings and can be applied to address specific neuroscientific questions. Some of the methods are complementary and can be combined together to provide more information about the neuronal activity underlying different behaviours or perceptions.

Various recording methods represent neuronal activity at different spatial (from the size of a single ion channel to large functional brain areas) and temporal scale (from the timescale of channel opening and closing to circadian rhythms). A comparison of spatio-temporal resolution of common recording techniques is shown in Figure 1.1.

Since no neuroscientific question can be answered without an appropriate recording technique, below some of the popular methods are briefly reviewed and ordered according to the scale they are most commonly used at.

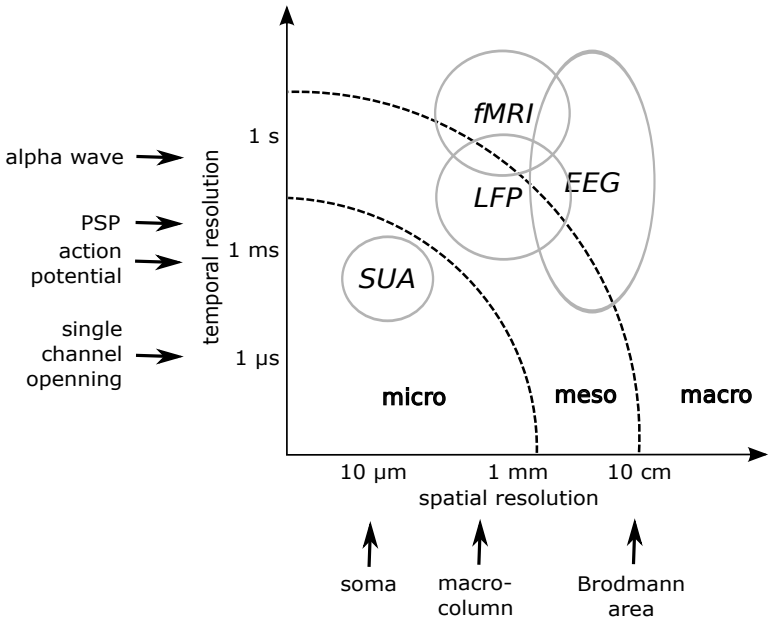

Figure 1.1.: Comparison of spatial and temporal resolutions of different neurophysiological recording methods. SUA – single-unit activity recorded with microelectrodes; LFP – local field potentials; EEG – electroencephalography; fMRI – functional magnetic resonance imaging

1.1.1. Microscale: single-unit activity

The microscale usually refers to the activity of single neurons, for example action potentials. At this level many theoretical and experimental studies were done, leading to important findings, such as membrane theory, properties of neuronal receptive fields, mechanisms of synaptic transmission and plasticity, and quantitative models thereof.

Action potentials produce large extracellular currents that can be detected by an electrode whose tip is placed in the vicinity of an active neuron (Mountcastle et al., 1991). The extracellular recording technique of single-unit activity (SUA) can be used in vivo in behaving animals and led to significant progress in neuroscience. However, this method allows one to study only a small subpopulation of neurons active during normal operation of the nervous system. Therefore, much of the effort today is directed towards the increase of the number of single neurons that can be recorded simultaneously (Buzsaki, 2004).

The state-of-the-art technique uses multiple microelectrodes (tetrode or shank electrodes), each of which possesses several electrical contacts. Each of the contacts provides an independent measurement (channel) of the extracellular potentials elicited by nearby neurons.

The amplitude and shape of action potentials of the same cell differ across the chan-

nels and electrodes because of the different distances from the origin of the potential. All action potentials belonging to a single cell can be discriminated automatically or semi-automatically with a procedure called spike sorting (Lewicki, 1998). This method makes use of the amplitude and shape information from different contacts to discriminate between action potentials elicited by different cells.

In Chapter 2 we will show how this technique can be used to discriminate various firing patterns of single neurons.

1.1.2. Mesoscale: multi-unit activity and local field potentials

The mesoscale is an intermediate scale and is commonly considered to relate to the dynamics of neural networks whose size may range from a few millimetres to a few centimetres (for example cortical macrocolumns, Mountcastle, 1997). Typical measures used to study neuronal processes at this scale are multi-unit activity and local field potentials.

Multi-unit activity (MUA) is obtained by means of high-pass filtering of the microelectrode recordings (cut-off frequency 250 Hz). Similarly to the single-unit activity discussed in the previous section, the MUA reflects the spiking output of neuron. However, the MUA combines the contributions not of one but of a group of cells surrounding the electrode and no effort is made to sort apart the activities of single units.

In contrast to SUA and MUA, local field potentials (LFPs) do not reflect the timing of action potentials, but rather they are correlated to slowly-changing graded potentials such as post-synaptic potentials, subthreshold membrane potential oscillations and spike after-potentials (Mitzdorf, 1985). LFPs are typically obtained from the microelectrode recordings by means of low-pass filtering (1 – 250 Hz). However, this definition of LFPs varies across studies as many different electrode systems and cut-off frequencies are in practice used.

Depending on the recording site, experimental paradigm and electrodes used for the recordings the spatial range of LFP can vary substantially. The estimates of the maximal distance of the sources contributing to LFP to the recording electrode range from several hundred micrometers to a few millimetres (Katzner et al., 2009).

1.1.3. Macroscale: electroencephalography

The macroscale reflects the activity of the whole brain and large brain structures (thalamus, brainstem, cortical areas) often recorded non-invasively in humans.

Hans Berger (1873-1941) obtained the first non-invasive recording of human brain activity using scalp electrodes and called it “das Elektrenkephalogramm” (electroencephalogram, EEG) (Berger, 1929). His publication was followed by a wealth of intensive basic and clinical studies which are still continued today. EEG consists of small amplitude electrical potentials ($\sim 10\,\mu$V) which can be picked up from the human scalp with surface electrodes. Similarly to LFPs they are believed to reflect mainly slowly-changing post-synaptic potentials (with frequencies < 100 Hz), but

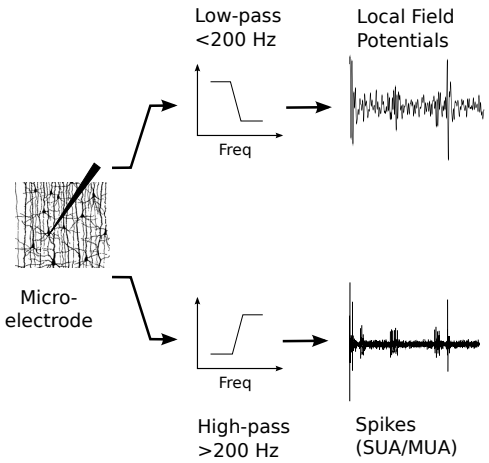

Figure 1.2.: Obtaining local field potentials (LFPs) and multi-unit activity (MUA) from microelectrode recordings.

summed over larger population of neurons. The EEG spectrum is often divided into separate frequency bands with different neurophysiological and clinical interpretations (see Section 1.3.5)

One of the disadvantages of EEG is its poor spatial resolution that is limited mainly by volume conduction (see below) and the spatial filtering introduced by the scalp (Nunez and Srinivasan, 2005). Although there are inverse methods available for three-dimensional localisation of EEG sources inside the skull (Lagerlund and Worrell, 2004), EEG can only rarely reach the spatial resolution of invasive as well as some non-invasive methods. On the other hand, EEG provides an excellent temporal resolution that can be only surpassed by invasive microelectrode recordings. This makes EEG especially useful in applications where fast-varying phenomena are under study.

1.2. Neurophysics of EEG

The main objective of the present work is to establish a link between the microscopic and macroscopic descriptions of the neuronal activity. To this end, it is necessary to understand how the neurophysiological phenomena give rise to the measured signals. Below we give a short overview of the physical theory at the interface between biology and measurement technology.

1.2.1. Maxwell's equations in matter

The propagation of an electromagnetic field in a vacuum is described by Maxwell's equations (Griffiths, 1999). In conductive media, which consist of a large number of free and bound charges, such as biological tissue, the corresponding fields must be averaged across an ensemble of particles (Jackson, 1998). The resulting "macroscopic"

equations constitute the Maxwell's equations in matter:

$$\nabla \circ \mathbf{D} = \rho \tag{1.1}$$

$$\nabla \times \mathbf{E} = -\frac{\partial \mathbf{B}}{\partial t} \tag{1.2}$$

$$\nabla \circ \mathbf{B} = 0 \tag{1.3}$$

$$\nabla \times \mathbf{H} = \mathbf{J} + \frac{\partial \mathbf{D}}{\partial t} \tag{1.4}$$

where $\nabla = \left(\frac{d}{dx}, \frac{d}{dy}, \frac{d}{dz}\right)$ is the nabla operator, $\mathbf{E}$ is the electric field, $\mathbf{D}$ is the electric displacement field, $\mathbf{H}$ is the magnetic field, $\mathbf{B}$ is the magnetic induction, $\mathbf{J}$ is the free current density, ρ is the free charge density.

In comparison with microscopic Maxwell's equations this system introduces two additional fields: the displacement field $\mathbf{D}$ and the magnetic induction $\mathbf{H}$. As a result it is underdetermined and can not be solved unless additional information is included. This information can be determined empirically and depends on the properties of the medium. For linear media the following relations are fulfilled (the so called constitutive relations):

$$\mathbf{J} = \sigma \mathbf{E} \qquad \text{(Ohm's law)} \tag{1.5}$$

$$\mathbf{D} = \epsilon \mathbf{E} \qquad \text{(linear dielectric)} \tag{1.6}$$

where σ and ϵ are material properties (electric conductivity and electric permittivity, respectively).

1.2.2. Basic laws of linear electrophysiology

For many practical purposes, biological tissue can be considered a linear medium, in which electric field and current differ from the field in a vacuum only by a multiplicative factor (equations 1.5–1.6; see also Malmivuo and Plonsey, 1995). This property simplifies the calculations and ensures that measured macroscopic quantities are linearly related to their microscopic sources (linear volume conduction).

Another useful simplification relies on the fact that in the low-frequency band (<1 kHz), which is of interest for most EEG studies, the magnetic and electric fields are effectively decoupled. This decoupling allows one to treat both fields separately depending on which one of them is recorded in the experiment. Since in this thesis we focus mainly on EEG and similar methods, we will describe the laws describing electric fields.

Based on the assumptions discussed above we can now list the basic field equations of linear electrophysiology (after Nunez and Srinivasan, 2005):

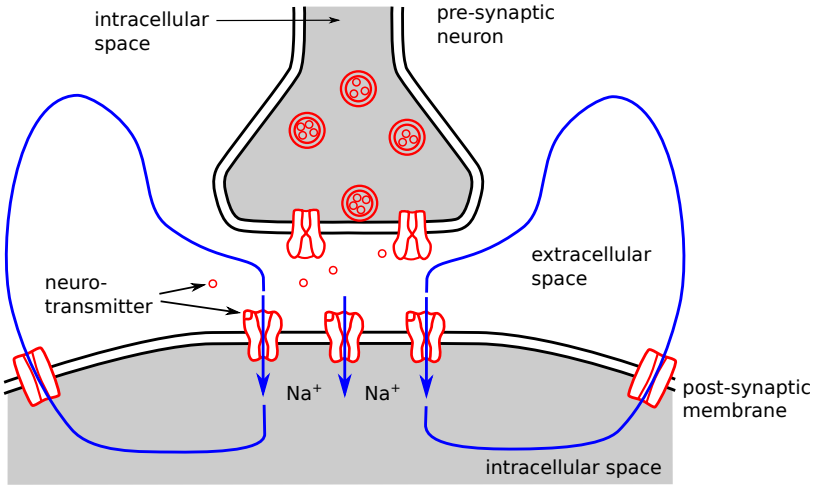

Figure 1.3.: Origin of post-synaptic currents

$$\mathbf{J} = \sigma \mathbf{E} \qquad \text{(Ohm's law)} \tag{1.5}$$

$$\mathbf{D} = \epsilon \mathbf{E} \qquad \text{(constitutive law for linear dielectrics)} \tag{1.6}$$

$$\nabla \cdot \mathbf{J} + \frac{\partial \rho}{\partial t} = 0 \qquad \text{(conservation of charge)} \tag{1.7}$$

$$\nabla \cdot \mathbf{D} = \rho \qquad \text{(Gauss' law)} \tag{1.8}$$

$$\mathbf{E} = -\nabla \phi \qquad \text{(definition of scalar potential)} \tag{1.9}$$

where ϕ is the scalar potential.

1.2.3. Poisson equation for currents

EEG fields in conductive media are due to transmembrane currents initiated by synaptic action or active conductances (Figure 1.3) operating at the neuronal membrane. The excitatory synaptic inputs induce a current flowing inward through the postsynaptic membrane thus generating a *current sink*. This current flows in the intracellular fluid and leaves the cell at more distant (distributed) locations to form closed current loops. This return path for the current causes an outward current flow through the membrane called a *current source* (Malmivuo and Plonsey, 1995; da Silva and van Rotterdam, 2004). The total inward membrane current must be equal to the total outward current as a result of charge conservation (1.7). For the inhibitory inputs the current sinks and sources are exchanged.

The surface potential due to such currents injected at the neuronal membrane can be calculated from the charge conservation law (1.7), Ohm's law (1.5) and the

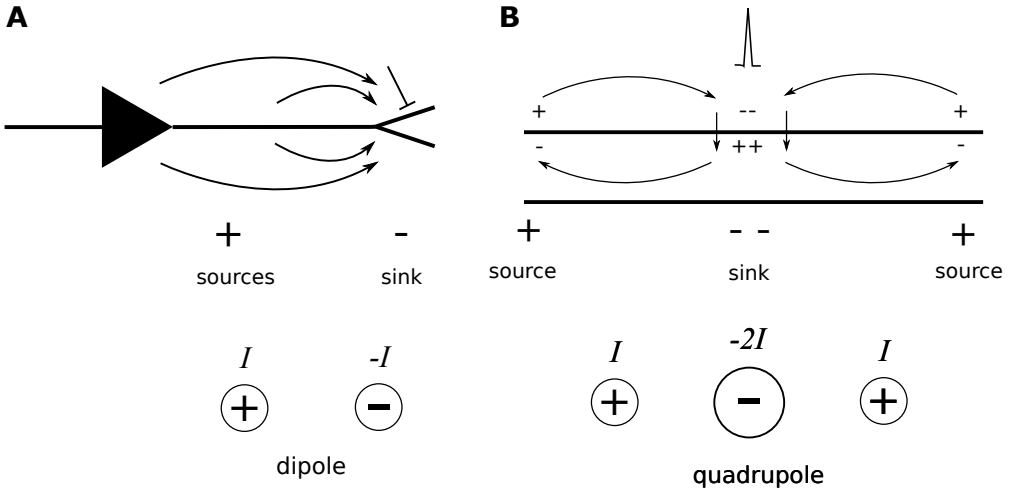

Figure 1.4.: (A) Sources and sinks due to synaptic potentials. Excitatory inputs arriving at dendrites produce a current sink that is balanced by a reverse current flow of equal magnitude (passive current source) at the soma. The resulting distribution of sources and sinks will have a dipole configuration. (B) Sources and sinks due to an action potential propagating along an axon.

definition of the scalar potential (1.9). Using these equations, one can obtain:

$$\nabla \cdot [\sigma(\mathbf{r}) \nabla \phi(\mathbf{r})] = -s(\mathbf{r}, t) \quad \text{(Poisson equation for currents)} \tag{1.10}$$

where $\sigma(\mathbf{r})$ is the tissue conductivity, which in the general case is a tensor depending on position and direction; $s(\mathbf{r}, t) = -\nabla \cdot \mathbf{J}_s(\mathbf{r}, t)$ is the volume current source function and $\mathbf{J}_s$ is the current density injected in the medium (for example, a transmembrane current density caused by synaptic activity in a neuron).

The equation called the Poisson equation for currents is mathematically equivalent to the Poisson equation for charge densities known from electrostatics. Therefore, after careful relabelling the physical quantities, one may re-use the solutions to standard problems of electrostatics to solve (1.10). For example, for a distribution of point sources with current intensities I_i localised at points $\mathbf{r}_i$ one can obtain:

$$\phi(\mathbf{r}) = \frac{1}{4\pi\sigma} \sum_i \frac{I_i}{|\mathbf{r} - \mathbf{r}_i|} \tag{1.11}$$

where $|\mathbf{r} - \mathbf{r}_i|$ is the distance of the source i from the measurement site $\mathbf{r}$.

1.2.4. Current dipole

The extracellular potential due to synaptic events is determined by the full distribution of membrane sources and sinks. The manner in which they are distributed depends on the conductivities of intra- and extracellular fluids and on both the con-

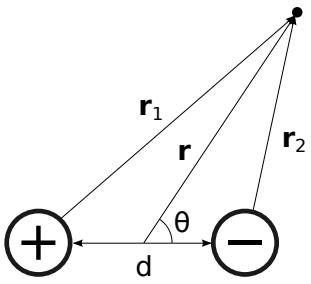

Figure 1.5.: Current dipole

ductivity and capacity of the membrane. Owing to the complicated three-dimensional geometry of neurons, the details of the source-sink distribution and the resulting extracellular potential can be difficult to calculate. However, in most EEG applications, we can bypass the complexity by traversing the spatial scale of current generation and defining an effective current dipole moment for each tissue volume (Figure 1.4A, Nunez and Srinivasan, 2005). The far-field electric potential ϕ of such a dipole in an infinite homogeneous medium is well approximated by:

$$\phi_{\text{dipole}}(r, \theta) \approx \frac{Id \cos\theta}{4\pi\sigma r^2}, \tag{1.12}$$

where I is the current density, d is an effective spatial separation of the sink and source, θ is the angle measured from the dipole axis, σ is the tissue conductivity and r is the distance from the dipole (Figure 1.5).

In order to estimate the EEG field from a given distribution of current dipoles, it is enough to sum the contributions of respective dipole moments in each tissue volume. Importantly, due to the inverse square dependence on distance from the source r, superficial cortical sources contribute more substantially to the total EEG field than deep brain structures such as the thalamus or brainstem.

1.2.5. Current quadrupole

The dipole approximation holds only for mesoscopic EEG sources that can be well described by a single pair of a current source and sink. In particular, microscopic sources at moderate distances the dipole approximation may not sufficient and it is necessary to expand the electric potential with higher-order terms which can be presented in this symbolic form (Malmivuo and Plonsey, 1995; Griffiths, 1999):

$$V(r) = \underbrace{a_1 \frac{1}{r^2}}_{\text{dipole}} + \underbrace{a_2 \frac{1}{r^3}}_{\text{quadrupole}} + \underbrace{a_3 \frac{1}{r^4}}_{\text{octapole}} + \ldots \tag{1.13}$$

The equation represents a so-called multi-pole expansion of a far-field potential due to an arbitrary distribution of current sources and sinks. The first term in the expansion is the familiar dipole term, and the subsequent terms describe fields due to

current quadrupole, octapole and so on. The contribution of the terms to the overall potential is scaled by an increasing power of the inverse distance between the source and measurement sites and multiplied by coefficients a_i that are a function of current intensity and separation between the sources and sinks. For example, a propagating action potential displays a triphasic sink-source configuration (Koch, 1999) whose dipole terms cancel out and it can be well approximated by a quadrupole (Figure 1.4B). The complete expression for the far field of such a quadrupole is:

$$\phi_{\text{quadrupole}}(r,\theta) \approx \frac{Id^2}{32\pi\sigma r^3}\left(3\cos^2\theta - 1\right), \tag{1.14}$$

with the symbols as defined previously.

1.3. Neuronal substrates of EEG signals

Although EEG signals are routinely used in clinical and scientific practice, the exact neuronal processes underlying the measured scalp potentials are often unclear. The relative contributions of different processes depend on the frequency range of interest, the location of the electrodes and the experimental paradigm. Based on the theoretical considerations presented in the previous section, we may now address the problem quantitatively.

1.3.1. Synaptic activity

Experimental and theoretical studies have pointed to post-synaptic currents (PSCs) as the main component contributing to scalp EEG (Nunez and Srinivasan, 2005; Peterson et al., 1995). In order to estimate how large their contribution is, let us calculate the macroscopic potential due to post-synaptic potentials triggered by a single action potential from a pre-synaptic neuron. Since the distribution of current sinks and sources due to synaptic currents can be well approximated by a current dipole (see Section 1.2.4), one can use the equation (1.12) to calculate the electric potential. The quantal amplitude of a post-synaptic current due to a single vesicle release is on average 10 pA (Stern et al., 1992; Lisman et al., 2007). Since each neuron makes on average 10,000 synaptic contacts, the total current can be approximated by:

$$I = 1 \text{ active neuron} \times 10\,000 \text{ synapses/neuron} \times 10 \text{ pA/synapse} = 100 \text{ nA}$$

The resistivity of the neuronal tissue can be approximated by $\eta = \sigma^{-1} \approx 3.5\ \Omega \cdot \text{m}$ (Nunez and Srinivasan, 2005). To estimate the sink-source separation we assume that the post-synaptic potentials penetrate the dendrites with exponentially decaying amplitude (Pettersen and Einevoll, 2008). The typical length constant of the decay is $d = 0.1\,\text{mm}$ (Koch, 1999). Finally, the recording electrode is assumed to be located

along the dipole axis (connecting the source and dipole) to yield maximal potential ($\theta = 0$).

Inserting the values into (1.12) we obtain the following estimates for the measured potential:

- at cortical surface (distance from the source $r = 2.5\,\mathrm{mm}$):

$$phi^{\mathrm{PSCs}}_{\mathrm{cortex}} = \phi_{\mathrm{dipole}}(2.5\,\mathrm{mm}) \approx 445\,\mathrm{nV}$$

- at scalp (distance from the source $r = 1.5\,\mathrm{cm}$):

$$\phi_{\mathrm{dipole}}(1.5\,\mathrm{cm}) \approx 12\,\mathrm{nV}$$

  After multiplying by a factor of 1/4 to account for lower skull resistivity (Nunez and Srinivasan, 2005):

$$\phi^{\mathrm{PSCs}}_{\mathrm{scalp}} \approx \frac{1}{4}\phi_{\mathrm{dipole}}(1.5\,\mathrm{cm}) \approx 3\,\mathrm{nV}$$

The ratio between potentials recorded at dura and scalp shows how fast the contributions from the synaptic potentials decay with distance: $\phi_{\mathrm{cortex}}/\phi_{\mathrm{scalp}} \approx 144$. Nevertheless, the value may be over-estimated because of the assumption that the source is localised. For coherent activation extending over larger areas of cortex the source and sink distribution is better described by a dipole layer (Nunez and Srinivasan, 2005). In such a configuration the decrease of the amplitude with distance is partially compensated by a larger area "visible" by the electrode and thus the fall-off is much slower.

The average amplitude of a spontaneous scalp EEG is between 10 – 100 μV, which means that at least 3,000 – 30,000 neurons need to be simultaneously active to generate a signal of this amplitude. Similarly, low-frequency evoked responses recorded at the scalp, which are mainly due to post-synaptic currents (Creutzfeldt et al., 1966), have an approximate amplitude of 5 μV that would require simultaneous activation of about 1000 – 2000 pre-synaptic neurons. However, in practice the number of active sources can be much higher because of partial cancellation of currents flowing in opposite directions in neighbouring cortical regions and incoherent activity of the neurons.

1.3.2. Somatic activity

The main output of neuronal computation, i.e. action potentials, are believed to make only negligible contributions to standard EEG signals (Murakami et al., 2003, 2002; Murakami and Okada, 2006; Buchwald et al., 1965). In order to quantify the contribution we will estimate the cortical and scalp EEG potential produced by a single action potential initiated in the soma (somatic action potential, sAP). The sAP propagates into a passive dendritic tree (through so-called antidromic spike invasion)

and thus generate a sink in the soma and associated sources in the dendrites. In some pyramidal neurons, such as layer 5 pyramidal neurons, the dendritic tree is elongated in the radial direction with the apical dendrites reaching the superficial layers of the cortex (Shepherd, 2004). In such a geometry the distribution of current sinks and sources due to sAP is well approximated by a current dipole.

At low frequencies the sAP can invade apical dendrites over the length of 1 mm with little attenuation (< 100 Hz) but with no contribution from active processes it is considerably attenuated at higher frequencies (at 1 kHz and 200 μm from the soma the potential is attenuated by a factor 1,000 – see Fig. 3.10 in Koch (1999)). Since typical action potentials are short in duration (average width ≈ 1 ms), they are characterised with wide power spectrum with significant power even above 1 kHz. In order to encompass both low- and high-frequency components of the sAP we place the lumped current source at an intermediate distance from the soma $d = 0.1\,\mathrm{mm}$. The current density involved in the generation of somatic action potential is of the order of $i_m = 5\,\mu\mathrm{A}\cdot\mathrm{mm}^{-2}$, so that for a typical soma with a surface of $S = 1.15\cdot 10^{-3}\,\mathrm{mm}^2$ (equal to the surface of a cylinder with a length of 15 μm and a radius of 8 μm; Traub et al., 2003) total current is approximately $I = i_m S = 5.75\,\mathrm{nA}$. The remaining quantities are equal to the ones estimated for synaptic inputs (see above). From the approximation of the far-field potential generated by a current dipole (1.12) we obtain the following estimate of the sAP contribution to surface potentials:

- at cortical surface:

$$\phi^{\mathrm{sAP}}_{\mathrm{cortex}} = \phi_{\mathrm{dipole}}(2.5\,\mathrm{mm}) \approx 25\,\mathrm{nV}$$

- at scalp:

$$\phi^{\mathrm{sAP}}_{\mathrm{scalp}} = \frac{1}{4}\phi_{\mathrm{dipole}}(1.5\,\mathrm{cm}) \approx 0.17\,\mathrm{nV}$$

Although the potential decays with distance equally fast for somatic action potential and synaptic potential ($\phi_{\mathrm{dipole}}(r) \sim 1/r^2$), the estimated cortical potential contributed by the sAP is approximately 20 times smaller. This decline arises mainly from the difference in the total current involved in the generation of the sAP and associated PSCs. A single pre-synaptic neuron may elicit thousands of synchronous post-synaptic currents in its targets, but most of them will not lead to the initiation of a sAP and thus will contribute to scalp potentials only through synaptic mechanisms.

1.3.3. Axonal activity

Typically an action potential initiated in the soma or axon initial segment will propagate down the axon due to active conductances present in the axonal membrane. This process results in additional contribution to the measured field potentials. As argued previously, the configuration of sinks and sources produced by an action potential propagating in an axon (axonal action potential, aAP) can be approximated by a quadrupole (Section 1.2.5). The separation between the current sink and sources

is equal to the length of the action potential, which in turn is the product of its propagation velocity v_{aAP} and duration T_{aAP}. For an unmyelinated axon:

$$d = v_{\mathrm{aAP}} \cdot T_{\mathrm{aAP}} \approx 0.7\,\mathrm{m/s} \cdot 2\,\mathrm{ms} = 1.4\,\mathrm{mm}.$$

The total current intensity I is equal to the total depolarising current flowing through the membrane during the action potential. For an action potential of an amplitude of $V_{\mathrm{aAP}} = 40\,\mathrm{mV}$ propagating along an axon with a radius of $r_{\mathrm{axon}} = 0.5\,\mu\mathrm{m}$ and membrane resistivity $R_m = 0.1\,\Omega \cdot \mathrm{m}^2$ (Traub et al., 1994, 2003):

$$I = S_m \frac{V_{\mathrm{aAP}}}{R_m} = 2\pi r_{\mathrm{axon}} d \frac{V_{\mathrm{aAP}}}{R_m} \approx 1.75\,\mathrm{nA}$$

where S_m is the area of membrane covered by the action potential (Koch, 1999).

We take the same tissue resistivity as in previous paragraphs and consider the angle at which the far-field potential is maximal ($\theta = 0$). Inserting the quantities into (1.14) we obtain:

- at cortical surface:

$$\phi^{\mathrm{aAP}}_{\mathrm{cortex}} = \phi_{\mathrm{quadrupole}}(2.5\,\mathrm{mm}) \approx 15\,\mathrm{nV}$$

- at scalp:

$$\phi^{\mathrm{aAP}}_{\mathrm{scalp}} = \frac{1}{4}\phi_{\mathrm{quadrupole}}(1.5\,\mathrm{cm}) \approx 0.017\,\mathrm{nV}$$

The ratio between the dura and scalp potential is equal to $\phi^{\mathrm{aAP}}_{\mathrm{cortex}}/\phi^{\mathrm{aAP}}_{\mathrm{scalp}} \approx 864$, which is much larger than the value estimated for the post-synaptic and somatic currents. The reason for the difference is that the potential of a quadrupole decays fast with the distance from the source ($\phi_{\mathrm{quadrupole}}(r) \sim 1/r^3$). Consequently, a significant number of neurons has to be active simultaneously to give rise to macroscopically observable electric fields. For example, to obtain a potential of $2\,\mu\mathrm{V}$ at the scalp, at least 100,000 aAP have to be simultaneously generated (cf. Murakami and Okada, 2006), whereas synaptic potentials require about 10,000 sAPs. In comparison, surface potentials of this magnitude could be generated by as few as 1,000 neurons through post-synaptic activity (Table 1.1). In addition, synaptic currents are much longer in duration allowing for constructive summation of potentials from diverse sources. These properties are one of the reasons why slowly-changing potentials associated with PSPs are the dominant feature of surface EEG.

In summary, both the decay of the respective field with the distance and the degree of synchrony determine the relative contributions from passive post-synaptic currents and action potentials to measured EEG field. Under certain conditions, which we discuss in Chapter 3, cortical neurons can fire in high synchrony allowing for their action potentials to sum up constructively and contribute to the net macroscopic field.

	PSCs	sAP	aAP
Surface potential (nV):			
– cortex	445	25	15
– scalp (without skull attenuation)	12	0.71	0.071
– scalp	3	0.17	0.017
Ratio cortex/scalp	144	144	864
APs in $\phi_{\text{scalp}} = 2\,\mu\text{V}$	650	11 000	112 000

Table 1.1.: Comparison of contributions from post-synaptic currents (PSCs), somatic action potentials (sAP) and axonal action potentials (aAP) to electric potential measured at cortical surface and scalp. Last row represents an approximate number of action potentials required to generate a scalp potential of $2\,\mu$V by each of the mechanisms.

1.3.4. Inhibition vs. excitation

As discussed above, various recording techniques are sensitive to different manifestations of neuronal activity: while SUA and MUA represent mainly the timing of action potentials, standard EEG and LFP recordings are related to the slow synaptic potentials, which only rarely lead to the generation of a spike.

This fact has important consequences for the interpretation of neural activation measured with different techniques (Figure 1.6). According to the basic electrophysiological considerations presented in Section 1.2, the orientation of the current dipole created by synaptic inputs will depend both on the type of the input (excitatory or inhibitory) and its location on the neuron (Speckmann and Elger, 2004). Specifically, excitation arriving at the dendrite will result in a dipole of the same orientation as generated by inhibition located at the soma (Figure 1.6B and C). This ambiguity makes both scenarios indistinguishable by means of standard EEG recordings. In contrast, the result of neuronal computations, that is, the spiking activity will be different. Consequently, the results obtained with standard EEG signals can not be directly related to single-neuron responses.

1.3.5. Oscillations

One feature that discriminates the mesoscale of small neuronal population from the microscopic scale of single neurons is the emergence of oscillatory activity covering frequencies from approximately 0.05 Hz to 500 Hz or even higher (see Chapter 3).

The frequency bands of the experimentally observed oscillations are conventionally labeled with Greek letters and their central frequencies form a geometric progression (Buzsaki and Draguhn, 2004). Neighbouring frequency bands generated within the same neural network are typically associated with different brain states, but many rhythms can temporally coexist and interact with each other. Some of the most commonly observed neuronal oscillations include (Bazhenov and Timofeev, 2006;

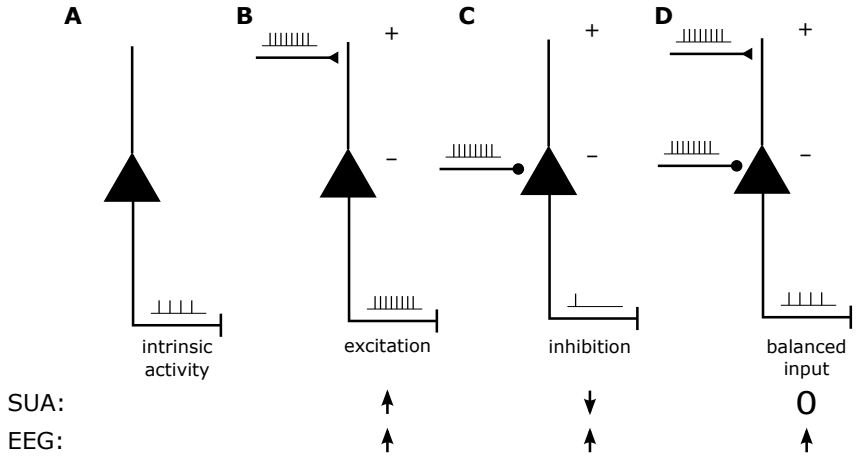

Figure 1.6.: Change of spiking (SUA) and EEG activity due to inhibitory and excitatory synaptic inputs localised at different compartments of the cell. (A) Spontaneous activity of a cell. (B) Change produced by excitatory synaptic inputs arriving at the dendrite. (C) Change produced by inhibitory synapses arriving at the soma. (D) Change due to simultaneous excitation and inhibition. Upward arrows denote increase of the activity measured with the respective input whereas downward arrows down denote decrease. Note that it is not possible to differentiate between these three scenarios with standard EEG recordings.

Niedermeyer, 2004):

- δ-oscillations (< 4 Hz) – particularly prominent over the anterior regions during slow wave sleep,
- θ-oscillations (4 – 7 Hz) – found both in human hippocampus and neocortex and are associated with memory and learning,
- α-oscillations (8 – 12 Hz) – found over posterior regions of the head in a relaxed state (eyes closed),
- β-oscillations (12 – 30 Hz) – found mainly over frontal and central regions where they are associated with the state of alertness,
- γ-oscillations (30 – 100 Hz) – found over sensory areas such as somatosensory cortex and primary visual cortex, involved in sensory and cognitive processing,
- high-frequency oscillations ($\geq$ 200 Hz) – found in the somatosensory cortex in response to peripheral stimulation (hf-EEG, 600 Hz; Hashimoto et al., 1996) and in rat hippocampus (ripples, 200 Hz; Buzsaki et al., 1992).

The amplitudes of these oscillations decay with the inverse of their frequencies. Although it has been proposed that this dependence on the frequency may result from passive low-pass filtering by the biological tissue (Bédard et al., 2006), the tissue

resistivity was recently shown to be almost constant in the physiological range of frequencies (< 1 kHz, Logothetis et al., 2007). An alternative explanation attributes the low-pass filtering to dendritic trees (Nunez and Srinivasan, 2005; Lindén et al., 2010): The distance at which the synaptic currents can penetrate a dendritic tree declines with the frequency of the input (Koch, 1999). As a result, the separation between the current sink and source (d in equation (1.12)) becomes smaller with increasing frequency and the resulting far-field potential at high-frequencies is attenuated.

The amplitude of the macroscopic oscillations depends also on the number of active neuronal elements and the strength of synchronization between them. Due to synaptic and conduction delays neurons synchronise more easily at lower frequencies allowing for tight synchronization of large cortical areas (Buzsaki and Draguhn, 2004). Spatially and temporally coherent activity produces, in turn, large-amplitude macroscopic oscillations.

Synchrony and number of active elements may be affected by sensory stimulation. For example, an external stimulus may recruit new neuronal elements to the oscillations, thus increasing the macroscopic amplitude. Similarly, the same increase in amplitude can be produced by boosting the synchrony among spontaneously active neurons. The differentiation between these two cases is crucial to understand the generation of evoked EEG responses (Sauseng et al., 2007). In Chapter 5 we show that it may not be possible to distinguish between these two mechanisms based on macroscopic oscillations because the relative change in the macroscopic amplitude expected from both mechanisms depends both on the level of spontaneous synchrony and activity.

1.4. Somatosensory system of primates

Most of the analyses and results presented in the thesis will concern the somatosensory system of non-human primates. Here, we will briefly introduce the essential facts about the neuroanatomy of the system and experimental methods used to record neuronal activity at its various levels. Those facts will assist in the discussion presented in the following chapters.

1.4.1. Somatosensory pathway

The somatosensory system is a part of the nervous system responsible for sensation of touch, temperature, pain and body position (proprioception). Sensory information is transduced into the electrical activity of neurons by specialised receptors in skin and muscles. For example, skin mechanoreceptors transduce information about fine touch and transmit it to neurons in the dorsal root ganglion of the spinal cord (Figure 1.7). The neurons carry the information up the spinal cord and form the first synapse either in the cuneate nucleus (fibers from upper body) or gracile nucleus (fibers from lower body) of the medulla oblongata. Axons of the postsynaptic neuron cross the midline of the brain and proceed at the contralateral side in a fiber bundle called

the medial lemniscus towards the thalamus. In the ventral posterior lateral nucleus of the thalamus the axons contact thalamocortical neurons that send their afferents to Brodmann area 3b of the cortex, typically located in the posterior bank of the central sulcus.

Throughout the somatosensory pathway the sensory information is represented in somatotopic fashion, which means that anatomically close neurons carry information about neighbouring areas of the body. The radial part of the palm and the palmar surface of the thumb, index and ring fingers are innervated by the median nerve which sends information to the spinal cord (Figure 1.7). The representation is preserved in the medulla and in the thalamus and forms a part of the ordered representation of the body in the cortex (the so-called homunculus).

1.4.2. Recording protocol

The data analysed in Chapters 2 and 3 have been used in a different study (Baker et al., 2003) in which the experimental protocol is described in more detail. Briefly, neuronal responses were evoked in the hand representation of the primary somatosensory cortex of two awake *Maccaca mulatta* monkeys by electrical median nerve stimulation at the wrist (pulse width: 0.2 ms; repetition rate: 3 Hz; intensity: 150% motor threshold). Single-unit activity was recorded extracellularly using a 16-channel Eckhorn drive (Thomas Recording GmbH; Giessen, Germany; Eckhorn and Thomas, 1993). Each of the platinum/glass electrodes (electrode impedance: 1 MΩ) was advanced into cortex (area 3b, Figure 1.7) until well-isolated neurons were found with one of the electrodes. The receptive fields of the cells were tested by means of manual tapping using a stylus. The local macro-EEG was measured with a bipolar ball electrode placed epidurally over the central sulcus ('epidural EEG' in Figure 1.7). The precise position varied from session to session, but the electrodes always spanned the posterior and anterior edges of the sulcus. Another macroelectrode was implanted in the pyramidal tract at the brainstem level which, due to its proximity to the medial lemniscus, could be used to monitor subcortical input variations ('brainstem electrode' in Figure 1.7). The location of the brainstem electrode in the pyramidal tract was confirmed during surgery by the presence of an antidromic field potential recorded from the surface of the motor cortex and at post mortem by histology.

All experimental procedures were performed according to Home Office UK (Scientific Procedures) Act 1986 regulations and institutional ethical guidelines. Details of the surgical protocol can be found in (Baker et al., 2001).

Prior to the subsequent analyses, field recordings (epidural EEG, brainstem activity) were bandpass filtered (3 Hz to 2 kHz) and sampled with a frequency of 5 kHz (monkey A) or 6 kHz (monkey B).

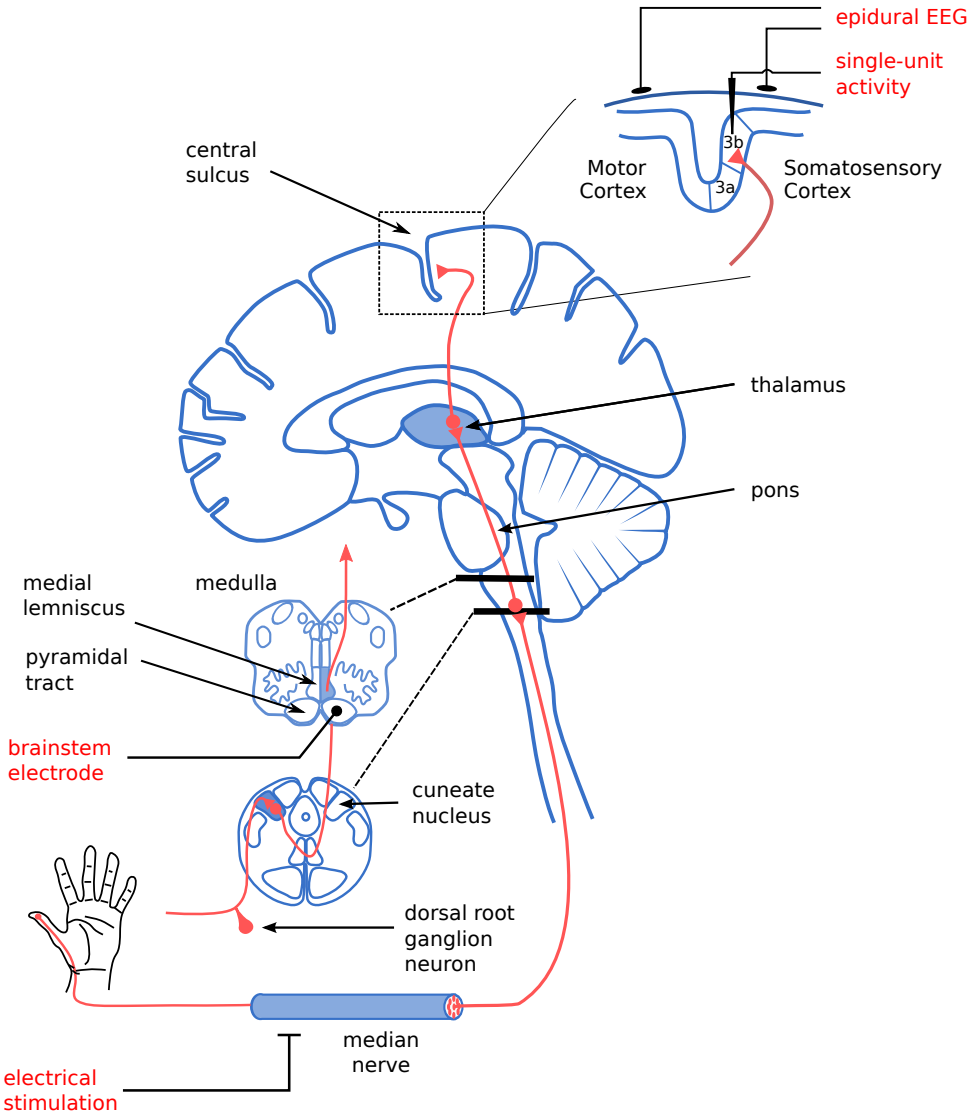

Figure 1.7.: Schematic representation of the somatosensory pathway in primates involved in touch perception. The pathway for touch perception in the palm is shown with red lines. Sensory information from the lateral part of the palm is sent to the cerebral cortex via the dorsal root ganglion, the cuneate nucleus of spinal cord, the medial lemniscus in the brainstem and the ventral posterior lateral nucleus of the thalamus. In addition to anatomical landmarks, the position of recording electrodes at different levels of the pathway is annotated (red labels).

2. Spike-pattern variability of cortical neurons

We start our discussion of the relation between microscopic and macroscopic scales of neuronal activity with an analysis of neuronal variability at microscopic level. In particular, we focus on the trial-to-trial variations in single neuron responses to peripheral nerve stimulation and show that they may be decomposed into stereotypical spike patterns. These spike patterns are then further analysed in Chapters 3 and 4.

Some of the results presented in this chapter were adapted from a published work (Telenczuk et al., 2011). [1]

2.1. Introduction

The output of neuronal computation consists of a series of action potentials, so-called spikes. The timing of these all-of-none events is the main information that can be transmitted between neurons. Therefore, it is of great importance to understand how sensory stimuli, internal states, memories and future actions are encoded in the trains of spikes (Perkel and Bullock, 1968).

One of the hypotheses states that neurons are stochastic units that encode their inputs solely through the firing rate averaged over time or population (firing rate code; Adrian and Zotterman, 1926; Barlow, 1972; Dayan and Abbott, 2001). However, in-vitro recordings have shown that cortical neurons can be very reliable and able to respond to fluctuating stimuli with a sub-millisecond precision (Mainen and Sejnowski, 1995; Keat et al., 2001; Bialek and Rieke, 1992). Such a high firing precision would enable neurons to encode information more efficiently in the time of single action potentials than in their average rate (Theunissen and Miller, 1995). Evidence for the temporal code has been found in multiple systems, including the visual cortex (Reich et al., 2000, 2001), auditory cortex (deCharms and Merzenich, 1996; Yang et al., 2008), somatosensory cortex (Petersen et al., 2001), hippocampus (Huxter et al., 2003) and even neural systems of invertebrates (Nemenman et al., 2008; Hooper, 1998). In spite of these experimental and theoretical advances, there is an

[1] In this work the PSTH-based clustering method, which constitutes the main part of this chapter, was introduced. It was a result of a collaboration with several researchers: Bartosz Telenczuk developed and implemented the classification algorithms and performed the analysis, Gabriel Curio, Andreas Herz and Stuart Baker conceived the project and provided important insights, Stuart Baker and Gabriel Curio performed the experiments. Other results presented in this chapter, specifically the use of the metric-based classification methods and detailed analysis of spike-pattern variability, represent an original and yet unpublished work.

ongoing debate regarding the nature of neural codes in the processing of information (Kumar et al., 2010; Ikegaya et al., 2004; Roxin et al., 2008) .

One of the important consequences associated with different neuronal codes is the interpretation of the variability in timing of individual action potentials. It has long been known that neuronal responses to single stimuli are highly variable (Werner and Mountcastle, 1963; Softky and Koch, 1993). Even without a sensory stimulus cortical neurons are spontaneously active in a way that approximates a random process (Poggio and Viernstein, 1964; van Vreeswijk and Sompolinsky, 1996). Firing rate code disregards spike-timing variability as noise added on top of a signal that can be filtered by averaging across time or ensemble of neurons. On the other hand, temporal code hypothesis proposes that the variability carries additional information about sensory stimuli or their internal context. This information is lost when just the total number of spikes is considered (Rieke and Warland, 1999).

Every neural system must operate under noisy conditions driven by random processes occurring at the molecular and cellular levels (White et al., 2000; Faisal et al., 2008; Azouz and Gray, 1999; Deweese and Zador, 2004). Therefore, an optimal neural code must balance between the capacity to encode new information and robustness against noise (Cover and Thomas, 2006). The robustness can be achieved by encoding the same information using a larger number of spikes as implemented by the firing rate code. However, as discussed earlier, such coarse-graining limits the capacity of the code that should represent the same amount of information with as few bits as possible. An interesting way to find the trade-off between the capacity and robustness is to encode information in stereotyped patterns of spikes with specific temporal relations (Fellous et al., 2004; Tiesinga and Toups, 2005; Tiesinga et al., 2008). If the patterns are sufficiently different from each other, small jitter in spike timing should not confound the information ensuring robustness of the code. This in turn allows for adaptation of the code to the noise level by choosing the optimal number of patterns to maximise the code's capacity.

In practice, it is difficult to test for the presence of such spike patterns in in-vivo recordings, because apparently random variability may be related to internal cortical states that are not under control of the experimenter. Here we study the variability of neuronal responses recorded in primary somatosensory cortex of awake behaving monkeys after electrical stimulation of the median nerve. This fixed sensory stimulation allows us to focus on the internally generated variability. Although on average the responses tended to occur at fixed latencies, we found that the individual responses were to a large extent different. We demonstrate that these variable responses can be differentiated into stereotyped temporal patterns of spikes that appear alternately over repeated presentations of the same stimulus.

2.2. Methods

For experimental protocols see Section 1.4.2.

2.2.1. Spike discrimination

Spike waveforms were first band-pass filtered (1 kHz – 10 kHz) and then sampled with a frequency of 20 kHz. Action potentials of neurons surrounding the microelectrode were detected in the extracellular recordings by means of amplitude thresholding; the threshold was chosen manually to detect spikes whose amplitude was significantly above noise level. The wave shapes of the detected action potentials were parametrised by their amplitude, width and projection coefficients on two main principal components. The spike timings of single units were determined based on these shape features using a manual cluster cutting method that allowed for identification of clusters of arbitrary shapes (Lewicki, 1998; Hazan et al., 2006). To ensure correct clustering the procedure was performed by two operators using different software packages (GetSpike, S. N. Baker; PySpikeSort, B. Telenczuk) and then checked for consistency.

In order to validate the spike discrimination we checked the extracellular action potentials generated by a putative single cell for the consistency of the wave shape and amplitude. Additionally, we searched for interspike intervals (ISIs) shorter than 1 ms; if such short intervals were found the clustering procedure was repeated. Spike trains with evidence of poor spike sorting (inconsistent wave shapes or ISIs < 1 ms) were excluded from subsequent analysis.

The quality of spike sorting was evaluated by means of spike signal-to-noise ratio and an 'isolation score'. Spike signal-to-noise ratio ($\mathrm{SNR_{spk}}$) was calculated as the peak-to-peak amplitude of the spike waveform averaged across all spikes divided by the three standard deviations of concatenated residuals obtained after subtracting the average from the individual spike waveforms. The mean $\mathrm{SNR_{spk}}$ of spikes from a dataset evaluated in the present study was 2.52 ± 0.80 (mean $\pm$ SD, range 0.87 – 5.03). This measure estimates the amplitude of the spike relative to the noise floor, but it is not sensitive to spike sorting errors (spike omissions). Therefore, in addition, we calculated a spike 'isolation score', which evaluates how well the spikes are discriminated (Joshua et al., 2007). This score estimated the probability that an event classified as a spike belonged to the spike cluster of a single unit as opposed to the background activity. The background activity containing noise and spikes of other cells was extracted by amplitude thresholding of the raw microelectrode record. In order to obtain a conservative estimate of the background activity the waveforms of only 2% spikes with smallest amplitude were first averaged, then the peak amplitude of the average was calculated and the threshold was set to half of its value. For perfectly isolated cells the spike isolation takes a value of 1, whereas in the case of complete overlap between background activity and spike cluster it will be smaller than 0.5. According to our evaluation of this 'isolation score' on simulated data, a value greater than 0.9 corresponds to spike discrimination with less than 5% of errors. In addition, the 'isolation score' calculated between spike waveforms elicited by two different cells recorded in independent penetrations was found equal to 1.00. The average isolation score of the single-cell spike trains from the present study was equal to 0.961 ± 0.030 (mean $\pm$ SD; range 0.904 – 0.998, Table A.1 in Appendix).

2.2.2. Selection of bursting cells

After spike sorting a total of 46 cells were identified in both monkeys. From this dataset only cells that responded with bursts of spikes separated by short interspike intervals were taken for the subsequent analysis of spike pattern variability. The receptive fields of the cells were identified to lie within the radial part of the palm and palmar surface of thumb, index and ring finger, i.e., in the territory innervated by the stimulated median nerve. Cells were classified as bursting based on two criteria: a response with more than one spike following at least 4% of stimuli, and a mode of the interspike interval histogram shorter than 1.8 ms. In the complete data set, responses of 30 cells (15 in each monkey) fulfilled these stringent criteria.

2.2.3. Spike patterns classification

After summing responses from these bursting cells over all trials prominent peaks were identified in the peri-stimulus time histograms (PSTH; bin width 0.2 ms, Figure 2.2B). As the within-burst spike composition varied from trial to trial, each trial was described with a binary string whose entries (one or zero) represented the occurrence or non-occurrence of a spike in a sequence of bins bracketing the major peaks of the overall PSTH: the borders between the bins were placed manually in the troughs of the PSTH (Figure 2.2B, C: vertical lines). Each string corresponded to one spike pattern; the length of the string equalled the total number of peaks in the PSTH (depending on the cell 1–4 digits; cf. Table A.1).

2.2.4. Metric-based clustering

The spike-pattern classification described above was compared to an unsupervised clustering method introduced by Fellous et al. (2004). Their method utilises measures of similarity between spike trains to calculate a matrix of pairwise distances between all trials. This matrix is then processed by a clustering algorithm whose goal is to partition single trials into clusters of similar responses. As a result one obtains a grouping that minimises inter-cluster and maximises intra-cluster distances. The advantage of this approach is that it discovers the structure in the high-dimensional data with minimal prior assumptions and no manual intervention.

In this study we employed a spike-train metric proposed by Victor and Purpura (1997). In particular, we applied the D^{spike} measure that takes into account the absolute times of spike occurrences. This metric quantifies the minimal cost of transforming one of the spike trains into the other. The basic operations include spike insertion/deletion (with the cost of 1) and shifting spikes in time (with the cost of $q|\Delta t|$, where Δt is the length of the shift). Here we used $q = 0.5\,\text{ms}^{-1}$, however small variations of the parameter did not have much impact on the findings. The obtained distance matrix was then clustered with Partitioning Around Medoids (PAM) algorithm implemented in the R 2.4.0 environment (Venables and Ripley, 2002). The number of clusters was chosen to maximise the average silhouette width (Kaufman

and Rousseeuw, 1990; Rousseeuw, 1987).

The correspondence between clustering using metric-based and PSTH-based technique was evaluated by means of the adjusted Rand index (Hubert and Arabie, 1985).

2.3. Results

Single-neuron spike responses vary in response latency and spike count.

We studied neurons in area 3b of somatosensory cortex that responded to electrical median nerve stimulation with short latency (approximately 8-10 ms after stimulus) bursts. In the analysis we included only well-discriminated units that in single trials fired several spikes separated by short interspike intervals (for selection criteria see Section 2.2.2). This way we obtained a population of 30 cells. Even in this selected subset there was a significant amount of cell-to-cell response variability. Therefore, we determined the average latencies of subsequent spikes in the burst (defined as the position of subsequent troughs in PSTH) for each cell separately (see Section 2.2.3). The distribution of the latencies found in all bursting cells is shown in Figure 2.1, which represents the degree of cell-to-cell variability observed under physiological conditions. A closer look at the figure allows one to delineate three sources of this variability, namely a first-spike latency (Figure 2.1, circles or stars), a number of spikes per burst (burst order, which is equal to the number of markers connected by a single line) and mean intervals between the spikes (measured in horizontal shift between the markers). The first-spike latency and burst order tend to dominate the overall variability by introducing constant shifts between the curves and by changing the lengths of the responses, respectively. Apart from two outliers, event durations are reasonably consistent and contribute little to the variability. However, in each cell there is a slight decreasing trend in the slopes, which is emphasised in the inset where width distributions of each window separately are drawn. The systematic shift of the distributions towards wider intervals between borders is probably due to increasing within-burst intervals (WBI) (Webster et al., 1997; Szucs et al., 2003).

Single-trial responses can be grouped into stereotyped spike patterns.

In order to quantify the neuronal variability found in the data we decided to cluster single-trial responses into patterns described by a sequence of spike events. In each trial individual spikes were assigned to one of the temporal windows whose borders were localised in the troughs of overall PSTH (Figure 2.2B). Because of unequal within-burst intervals, as discussed previously, the borders are not uniformly spaced. Each trial is assigned a binary sequence defined by the presence (1s) or absence (0s) of spikes in subsequent windows. All trials described by the same binary sequence constitute a spike pattern. Sample spike trains of each class are shown in the raster plot (Figure 2.2C) and the percentage of trials belonging to that class is depicted by the adjacent bar (Figure 2.2D). In the example shown, the most frequent patterns

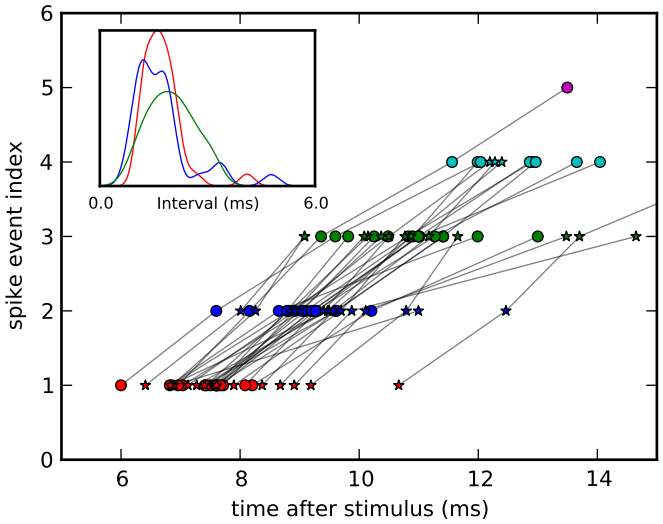

Figure 2.1.: Cross-cell variability: the response latencies (equal to the latency of the first event) and the timing of subsequent PSTH troughs are summarised over all cells in both monkeys (circles and stars, colour reflects the index of spike event). The spike events identified in PSTH of a single cell are connected with lines. Recorded cells responded with a wide distribution of latencies, but subsequent spike events have approximately fixed temporal relation to the response onset, which is reflected in similar slopes of connecting lines. The cross-cell distribution of the intervals between events is shown in the inset (kernel density estimator, color code is consistent with event markers).

are burst of different lengths: singlets (100), doublets (110) and triplets (111). Interestingly enough, the cell also produced other forms of doublets including a late (011) and a long interval (101) doublet. The latter we called a "missing middle spike" pattern for reasons we discuss below. It is important to note that such distribution of patterns across trials could not be predicted from the PSTH alone, since many different single-trial distributions could result in a similar average PSTH.

We additionally tested whether this intriguing variability of spike patterns was not just a sign of a poor spike sorting. First, we verified visually that spikes elicited in the pre-defined bins have the same wave shape (Figure 2.2A). We found that the consecutive spikes were very similar with only slight variations in the amplitude, which could be explained by a non-stationarity of spike waveforms generated within a burst (Lewicki, 1998). Next, we tested whether the spikes elicited within different spike patterns could reflect responses of different cells erroneously classified to the same spike cluster. To this end, we calculated an 'isolation score' (see Section 2.2.1) of spikes elicited within a given spike pattern from spikes of the same cell, but classified to other patterns (background activity). We found that when averaged across all patterns the 'isolation score' was low (mean $\pm$ SD: 0.32 $\pm$ 0.13; range: 0.16 – 0.59) indicating that the spike patterns were elicited by a single cell. Finally, we calculated

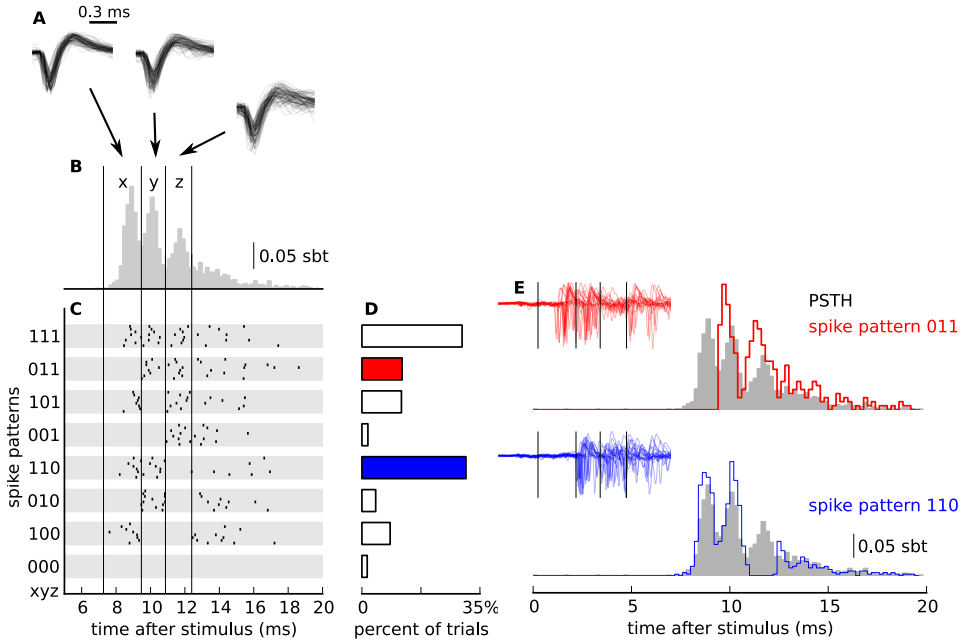

Figure 2.2.: Variable single-unit responses in S1 cortex can be classified into a reduced set of spike patterns. (**A**) Extracellular spike wave shapes are consistent across multiple repetitions of the stimulus (superimposed traces of 100 spikes) and positions within a burst (each panel corresponds to a single spike latency window delimited in B and pointed at by the arrow) indicating that they all were elicited by the same cell and can be addressed as single-unit activity. (**B**) Single-cell responses averaged over all trials (peri-stimulus time histogram, PSTH; sbt = spikes per bin per trial) reveal that spikes occur preferentially at discrete latencies (delimited by vertical lines). (**C**) In single trials multiple spikes are elicited in diverse combinations of preferred latencies resulting in significant trial-to-trial response variability. Spike combinations are classified into spike patterns: Each trial is assigned a binary string (spike pattern 'xyz', from '000' to '111') whose entries (0 or 1) represent the (non-)occurrence of a spike in a sequence of three bins aligned to the peaks of the overall PSTH. Spike timings of eight representative sample responses assigned to each pattern are shown as raster plots. (**D**) Frequency at which the spike patterns occurred over repeated trials. Color-coded spike patterns are shown in detail in (E). (**E**) Normalised sub-group PSTH of two sample spike patterns highlighted in D (red: pattern 011; blue: pattern 110; grey-bars: all trials; sbt = spikes per bin per trial). As expected spike activity is visible only in windows corresponding to the 1s in the binary string. Similarly, raw microelectrode voltage traces (insets, superimposed 100 sample traces) do not contain action potentials in the remaining "empty" windows confirming that the observed spike pattern variability was not due to spike sorting errors (omissions).

the pattern-specific PSTH and plotted it together with raw extracellular recordings from which the spikes were discriminated (for two example patterns, 110 and 011, see Figure 2.2E and insets). Evidently, both PSTHs and raw spike traces show a

lull of activity in bins were no spikes were present (0s in the corresponding digits of the binary string). Interestingly enough, the peaks of pattern-specific PSTH do not completely overlap with the peaks of total PSTH (grey shading in Figure 2.2E) indicating that apart from spike count, also first spike latency and interspike intervals may be variable across patterns.

Spike pattern set is an over-complete representation of responses.

The partitioning of spike trains into the respective classes relies heavily on the allocation of the individual spikes into the firing events. As a result the obtained pattern distributions may be sensitive to the exact location of the borders between the events. In order to test for significance of this effect and validate the obtained partitioning of the data, we repeated the analysis with an independent method based on cluster analysis (see Section 2.2.4). This approach performs an objective partitioning of the data with minimal prior assumptions and few free parameters. In contrast to the PSTH-based method, it does not require a priori grouping criteria, but rather explores pattern variability in an unsupervised fashion.

The unsupervised clustering method exploits the pairwise D^{spike} distances between all single-trial spike responses (Figure 2.3A). The individual responses are grouped into a small number of clusters in a way that minimises the sum of distances between the spike trains belonging to the same cluster (Figure 2.3B). The number of clusters is chosen such that the clusters are compact and well-separated from each other as quantified by average silhouette width (see Section 2.2.4; Figure 2.4, left).

Application of the method to responses of a sample cell led to identification of three different clusters. In order to characterise them and compare them to the results from the PSTH-based approach, the PSTHs of the spike trains assigned to each of the clusters were calculated and plotted separately (Figure 2.4, left). In two of these PSTHs (calculated from responses of Classes 2 and 3) we found prominent peaks that aligned well with the peaks of the overall PSTH (dashed lines denote the troughs between those peaks, cf. Figure 2.2B). The differences between those two PSTHs were almost entirely limited to the third peak confirming that the trial-to-trial variability was contained mainly in the presence or absence of spikes in a discrete set of preferred latencies. Since this type of variability is also leveraged by the PSTH-based approach, it is not surprising that the two classes correspond well to spike patterns extracted using the PSTH-based method: the majority of spike trains belonging to Class 2 were assigned to pattern 111 by the PSTH-based methods while spike trains of Class 3 were represented mainly by patterns of type 110 (Figure 2.4, right).

In contrast to Classes 2 and 3, Class 1 could not be easily characterised solely from PSTH of its responses. The peaks of the PSTH were shifted in time with respect to the peaks of the overall PSTH and they overlapped with the window borders used to determine the spike patterns in the PSTH-based approach (Figure 2.4, left, bottom row). As a result, responses belonging to Class 1 were not directly related to a particular PSTH-based pattern, but they were rather a mixture of patterns not

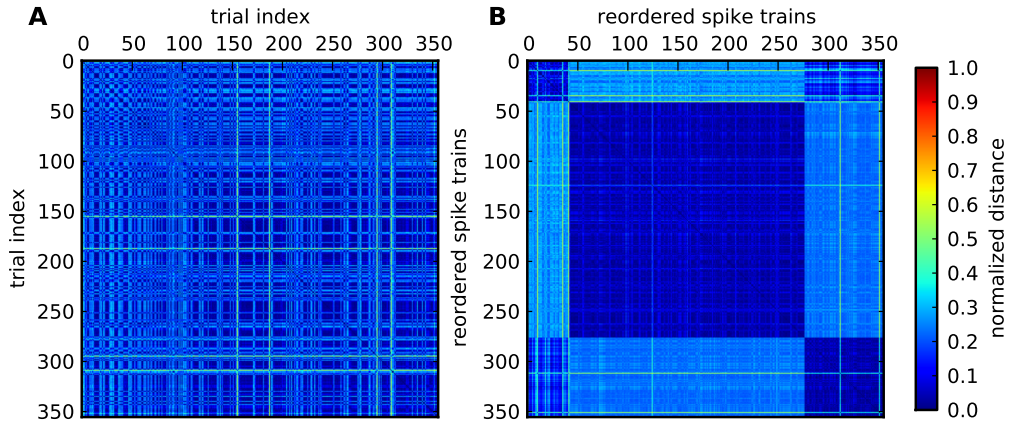

Figure 2.3.: A matrix of pairwise differences between spike trains in the order of their appearance in the responses train (A) and after grouping trials with the same cluster membership (B). The distances are calculated by means of the Victor metric (D^{spike}) with parameter $q = 0.5$ ms^{-1} normalised by the summed number of spikes. The clusters were found by an unsupervised clustering algorithm (Partitioning Around Medoids).

accounted for by the other two classes (Figure 2.4, right). This is also reflected by the low cluster strength as quantified by the silhouette width s.

In order to check whether the different responses present in Class 3 could be further separated, we repeated the unsupervised clustering procedure with an increasing number of clusters K. For each K the metric-based clustering of single-trial responses was compared to the classification by means of the PSTH-based approach. The similarity between response classes determined with both methods was quantified by means of an adjusted Rand index. The value of the index was then plotted as a function of the number of clusters (Figure 2.5B). We found that the metric-based clustering was most similar to the results of the PSTH-based method when three clusters were identified by means of the unsupervised algorithm. Interestingly, the same value maximises the total cluster strength quantified by the average silhouette width (Figure 2.5A). This number is much lower than the total number of PSTH-based patterns identified in the cell (8 patterns) suggesting that the latter method produces an overcomplete representation of the trial-to-trial variability.

The incapability of the metric-based clustering method to differentiate between larger number of patterns could also result from a low number of available response trials so that rare patterns occurring in a small fraction of trials were underrepresented and could not be properly explored by the clustering algorithm. This problem does not occur in the PSTH-based method that provides fixed criteria for pattern classification and may be used to differentiate single trials regardless of their count. The resulting patterns are also easier to describe in terms of simple features

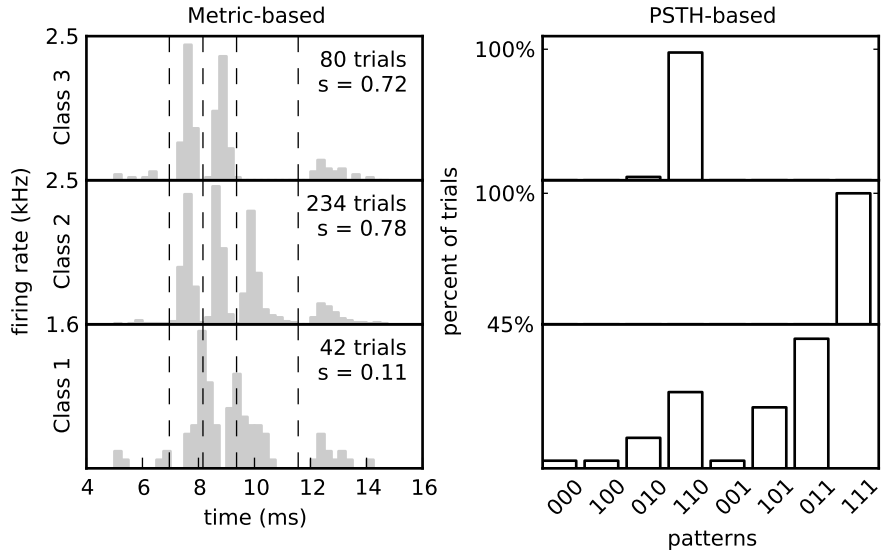

Figure 2.4.: Comparison of two spike-train clustering methods. The left panel shows PSTHs of three spike patterns determined with metric-based clustering (D^{spike} metric, Partitioning Around Medoids algorithm, PAM, see also Methods). For comparison, the vertical lines depict the window borders that are used in the PSTH-based algorithm. The numbers in the upper-right corner of each panel denote the number of trials assigned to a given class and a cluster strength (cluster average silhouette width, s). The right-hand side charts directly compare the partitions obtained by metric-based and PSTH-based methods. The bars show what fraction of trials within Class 1, 2 and 3, respectively, was assigned to each of the PSTH-based patterns. The Classes 2 and 3 (two top panels) are equivalent to a doublet (110) and a triplet (111) pattern determined by PSTH-based method. The Class 1 is not directly related to any of the PSTH-based spike patterns, but rather contains a heterogeneous mixture of remaining trials.

(such as number of spikes, latencies) and can be compared across cells. Therefore, in the following chapter (Chapter 3) we will use the PSTH-based definition of spike patterns.

Spike patterns represent distinct firing modes of the neuron.

In order to find electrophysiological substrates for the different spike patterns, we investigated interspike interval histograms (ISIHs). The distribution of intervals between adjacent spikes elicited by a sample cell is clearly bimodal (Figure 2.6). Its first peak reaching the maximum at about 1.2 ms contains mainly short ISIs produced within the burst, but the second peak was found at a longer time scale (4.2 ms). The variable ISI lengths could reflect prolongation of late intervals occurring within a single burst (WBI) that was described before (Figure 2.1). In order to exclude this possibility we analysed only ISIs occurring within doublets (defined as an isolated pair of spikes separated by less than 7 ms) and found that they also followed

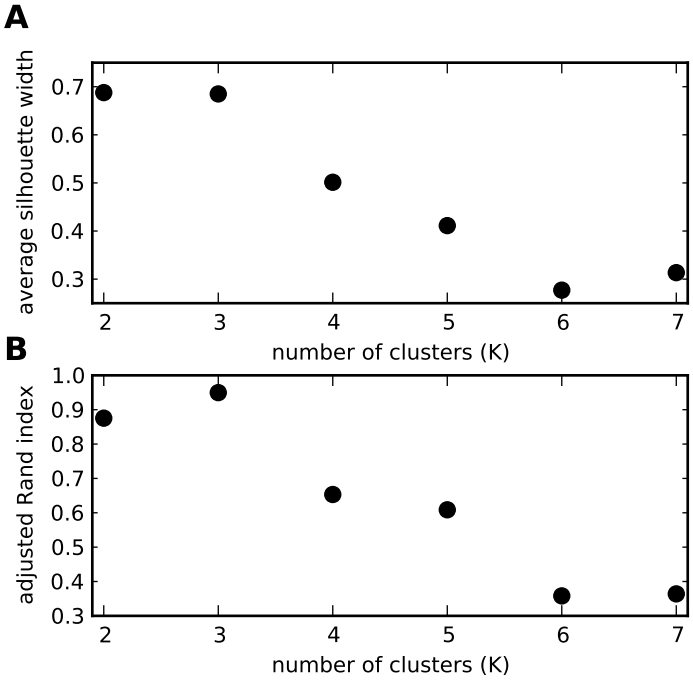

Figure 2.5.: Estimation of optimal number of clusters. (**A**) The average silhouette width decreases when the number of clusters is increased above 3. The number of clusters that maximises the average silhouette width ($K = 3$) is taken as the optimal value. (**B**) The correspondence between spike-pattern classifications using two independent algorithms (metric-based and PSTH-based) evaluated by means of adjusted Rand index is the best when the spike responses are partitioned into three separate clusters by the unsupervised algorithm.

a bimodal distribution. This suggests that the short and long doublets are separated entities that are not generated by the same mechanism.

This observation raises an interesting question: whether these two doublet types are related to two different types of spike patterns discriminated with the PSTH-based classification algorithm. To test the hypothesis we classified the spike patterns based on interspike intervals (ISIs). First, we divided the ISIs into short and long intervals (the demarcation line is shown in the upper left panel of Figure 2.6) and plotted PSTHs of corresponding spikes separately (Figure 2.6, right panel). This segregation resulted in two spike patterns similar to short (110) and long (101) doublets identified by means of the PSTH-based classification. PSTH of these patterns showed remarkable similarity to the PSTH obtained from triplets, the only difference being that some of its peaks were omitted. In particular, doublets with long ISIs produced a spike pattern where a middle spike of the full triplet was missing, hence its name a "missing middle spike" pattern. Although it is tempting to link all patterns of type 101 to the long doublets, it is important to note that such multimodal ISI distributions were found only in a fraction of all bursting cells (by visual inspection: monkey A – 7/15 cells; monkey B – 4/15 cells).

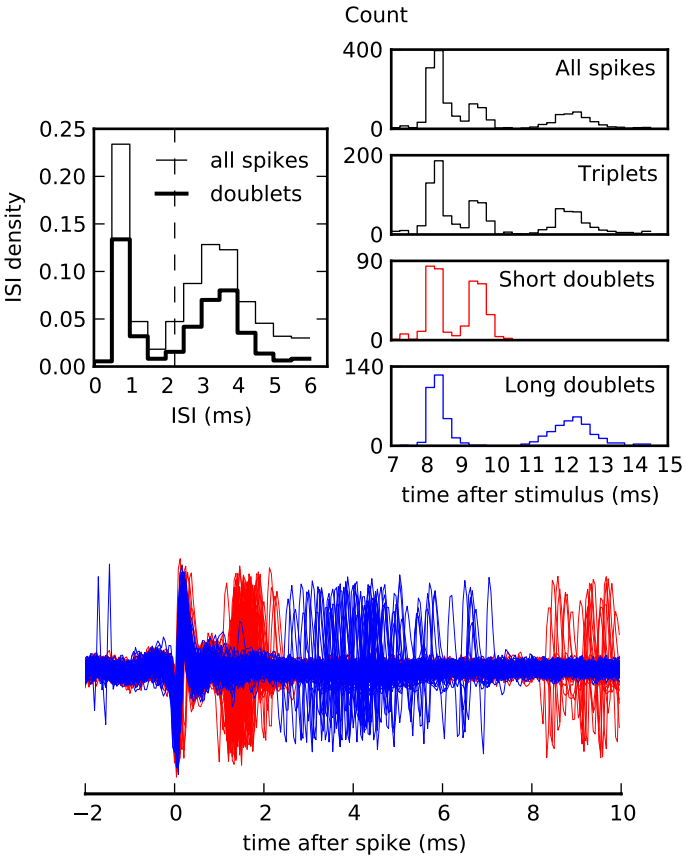

Figure 2.6.: Spike patterns may reveal distinct firing modes of the neuron. (**Left**) The intervals between spikes elicited by the neuron follow a bimodal distribution (thin line). Modes of the histogram do not change when intervals occurring only in doublets are considered (with maximum ISI equal to 7 ms, bold line). The doublets are separated into two classes (short- and long-doublets) with a depicted decision boundary (dashed line). (**Right**) Peri-stimulus time histograms of the patterns classified based on ISI: all trials, triplet, short- and long doublets. Short- and long-doublets resemble a triplet where one of the peaks is missing. Similar classes were obtained with PSTH-based clustering (early doublet pattern, 110, and missing middle spike pattern, 101). (**Bottom**) Raw recording of extracellular potentials with long doublets (blue) and short doublets (red) after alignment to the first spike of the burst. Both classes indeed show differential timing of the second spike (visible as a train of sharp peaks at about 4 ms and 2 ms, respectively)

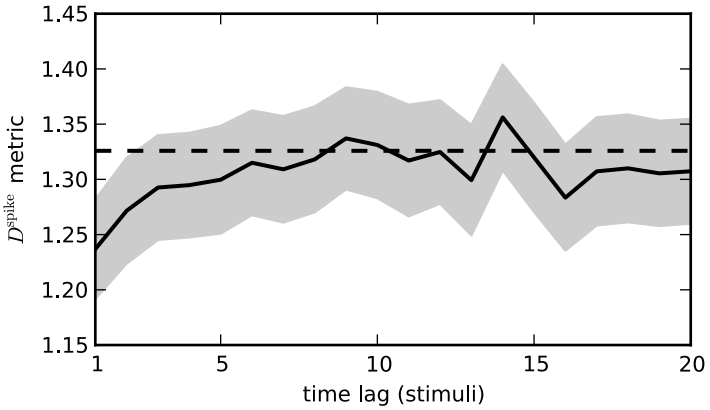

Figure 2.7.: Neuronal responses are modulated by slowly varying processes. Auto-distance between spike burst responses as a function of the number of stimuli (lag) separating the responses. Each data point represents a mean D^{spike} distance between pairs of spike responses lagged by a given number of trials (bold line). The gray shaded area depicts a 95% confidence interval of the mean (mean $\pm$ 1.96 standard error); the dashed line depicts mean distance calculated from all trial pairs. The distance between subsequent responses is significantly lower than the mean distance between all trials.

Neuronal responses vary at the slow time scale.

The variability of single-cell activity was suggested to be related to stochastic forces acting at cellular or molecular level (see also Section 4.3). These processes are normally characterised by very short correlation time. In order to test whether they could contribute to the stereotyped variability of the responses found in the somatosensory cortex, we estimated the temporal correlation of response fluctuations. To this end, we calculated the dissimilarity between single-trial spike trains as a function of their temporal proximity. Single trials were compared pairwise by means of a spike-train metric (D^{spike} metric, see Section 2.2.4). The pairwise distances were then averaged over trial pairs separated by the same number of stimuli and plotted as a function of the separation (stimuli lag). The result bears much similarity to an autocorrelation function, but it expresses the distance between two trials rather than their correlations as a function of a time lag.

The results of the analysis (Figure 2.7) show that temporally close trials tend to be more similar to each other than trials which are far apart: The distance between responses separated by three or less trials remains smaller than the average distance calculated from all response pairs regardless of their separation in terms of stimuli (Figure 2.7, dashed line). This indicates that processes modulating the responses have a time scale of about 1 s (three trials with an inter-stimuli interval of 330 ms), which is much longer than the time scale of most processes operating at molecular and cellular levels.

2.4. Discussion

In this chapter we focused on the variability of evoked neural activity. We showed that single-cell responses to median nerve stimulation are heterogeneous and range from singlets to triplets in different arrangements. By means of a classification algorithm based on absence or presence of spikes in predefined bins we sorted these responses into stereotypical patterns. While many patterns differed mainly by the number of spikes, which is characteristic of the firing rate code, other patterns were defined by the fine temporal structure of its spikes (for example short and long doublets). As discussed in the introduction these temporal patterns may carry additional information about the stimulus or the internal state of the somatosensory cortex.

The presence of spike patterns in neural systems has been a topic of intensive research. Single neurons in various systems encode stimulus features more reliably in the precise temporal sequence of their discharges than in their firing rate (Victor and Purpura, 1996; Middlebrooks et al., 1998; de Ruyter et al., 1997; Middlebrooks et al., 1998; Petersen et al., 2002). Here, we did not examine the relation of discovered spike patterns to the sensory stimulus but instead focused on spontaneous variations during repeated presentation of the stimulus. Moreover, we analysed the single-cell responses on finer time scale (at the order of milliseconds) than reported in previous studies.

Several mechanisms might be involved in the generation of different spike patterns. It has been suggested that reliable spike patterns are shaped by precisely timed input generated, for example, by an external stimulus, synaptic dynamics (Maass and Zador, 1999), or intrinsically generated network activity (Tiesinga and Toups, 2005; Memmesheimer and Timme, 2006). Since the single-cell responses we analysed in the present study occurred at a very short time scale (ISI $\sim$ 2 ms, duration 8 ms) contribution from bursting mechanisms is more likely. Generation of bursts often involves intrinsic cellular mechanisms such as resonant properties (Hunter et al., 1998) or slow spikes (Izhikevich, 2010). Bursting can play an important role in sensory systems increasing the reliability of synaptic transmission or triggering synaptic plasticity (Lisman, 1997). Moreover, the mode of bursting may be controlled by peripheral and feedback inputs (Webster et al., 1997; Krahe and Gabbiani, 2004). Bursting phenomena are a reasonable candidate for the physiological mechanisms underlying spike pattern generation but their contribution to the neuronal activity in primary somatosensory cortex remains to be investigated.

Here, we provide a simple interpretation of selected spike patterns based on the analysis of interspike intervals (ISIs). We show that the intervals within doublets follow a bimodal distribution reflecting differential mechanisms of burst generation. When separated into two subsets, the doublets representing each mode reproduce distinct patterns identified by our classification algorithm (110 and 101). The mechanisms behind this phenomenon may be elucidated by findings from intracellularly recorded cells of the rat somatosensory cortex (Jones et al., 2000). There, the action potentials of regularly spiking neurons were shown to be elicited at preferred latencies

determined by the peaks of high-frequency field-potential oscillations (400 – 600 Hz). Most interestingly, in some cases the neurons failed to elicit spikes at selected latencies but fired normally otherwise. In our analysis the discrete windows of an increased firing probability could constitute such discrete events of preferred firing. Therefore the failures of action potential initiation observed by Jones et al. (2000) could provide an explanation for the patterns with missing spikes found in our data ("missing middle spike" pattern, 101). It is, however, important to note that this mechanism of spike pattern generation does not explain the occurrence of such patterns in neuronal responses whose overall ISI distribution contains only a single maximum.

Reasons behind the occasional failure of an initiation of action potential are not yet clear. If it was driven solely by stochastic processes occurring at cellular level such as failures of synaptic transmission, stochastic channel openings or threshold variations one could expect that such spike omissions would occur at random intervals and thus would not be correlated across the stimulus repetitions (Faisal et al., 2008; White et al., 2000). However, we found significant temporal correlations between neuronal responses separated by up to 1 s. Such long time scales are typical of slow modulations of neuronal excitability that emerge spontaneously in thalamocortical networks during normal waking and sleep (Bazhenov et al., 2002; Compte et al., 2003; Holcman and Tsodyks, 2006). Therefore, we conclude that the neuronal patterns do not arise solely due to stochastic cellular and molecular phenomena but are under the influence of the global state of the thalamocortical system.

In order to clarify some of the origins and functional significance of spike patterns, in the following chapters we study the relation between spike patterns and macroscopic population responses (Chapter 3), and analyse a simple phenomenological model of spike patterns (Chapter 4).

3. From microscopic single-cell responses to macroscopic EEG oscillations

In the previous chapter we discussed the variability of neuronal response at microscopic, single-cell level. Here, we describe variability at much the larger scale of synchronous neuronal ensembles. We provide experimental evidence of a link between those two levels and discuss the possible consequences.

This chapter was adapted from a published study (Telenczuk et al., 2011). [1]

3.1. Introduction

Eight decades after Berger (1929) first described the electroencephalogram (EEG), this non-invasive measure still serves as the main tool for recording human brain activity at high temporal resolution. However, standard EEG recordings ($f < 100$ Hz) primarily reflect mass post-synaptic potentials, rather than spikes, which are the basic output of cortical computations. Since not all synaptic inputs lead to an initiation of action potentials, measurements of summed post-synaptic potentials alone cannot show the net computational effect on neuronal output (see Section 1.3.4). Standard EEG methods do not, therefore, provide definitive conclusions about the contribution of neuromodulatory, feedforward and feedback connections to neural processing, and may even confound excitation and inhibition (Speckmann and Elger, 2004).

Critically, non-invasive EEG recordings also contain signals at a high-frequency range ($f > 400$ Hz) which offer the temporal resolution required to catch short-lived action potentials; unfortunately, such signals are usually much lower in amplitude than the summed slow potentials related to post-synaptic activity (Buzsaki and Draguhn, 2004). High-frequency EEG components have, therefore, at times been neglected or even regarded as noise. However, averaging of scalp EEG responses over repeated electrical stimulations of a peripheral nerve can reveal a distinct high-frequency burst of EEG oscillations ($f > 400$ Hz, hf-EEG) superimposed on the much larger primary post-synaptic response (Cracco and Cracco, 1976). Generators of both burst and post-synaptic responses have been localised to the human primary somatosensory cortex (Curio et al., 1994; Hashimoto et al., 1996).

The cellular substrates of this hf-EEG have been previously investigated by invasive extracellular recordings of single-unit activity in the somatosensory cortex. Neurons

[1] This work is a result of a collaboration with several researchers. Bartosz Telenczuk developed the analysis tools, performed the analysis and wrote the manuscript. Gabriel Curio, Andreas Herz and Stuart Baker conceived the project, helped to develop the analysis tools and provided feedback on the manuscript. Stuart Baker and Gabriel Curio performed the experiments.

localised in cortical area 3b respond to median nerve stimulation either with a burst of two to four spikes separated by very short intervals or with a single spike at preferred latencies (Baker et al., 2003). The timing of spikes generated by both types of neuronal response has a close relation to the hf-EEG: the peaks of the population peri-stimulus time histogram (PSTH) calculated from those responses align with peaks of the averaged hf-EEG (Baker et al., 2003). Mechanistically, this coupling between average single-cell and hf-EEG responses suggests that surface hf-EEG components reflect either synchronous action potentials of cortical neurons or ultrafast postsynaptic potentials (Stern et al., 1992; Curio et al., 1994; Hashimoto et al., 1996; Shimazu et al., 2000; Baker et al., 2003).

In light of these findings high-frequency EEG is the only currently available non-invasive measure of cortical neuronal spiking in human subjects. How close can it bring us to single-neuron activity? In order to answer this question, we studied if and how the observed trial-to-trial variability in the timing of single-neuron spike response described in the previous chapter is reflected in the concomitant surface hf-EEG. If indeed the macroscopic hf-EEG reflects the timing of underlying neuronal activity there should be a significant covariation between single-cell spike patterns and concomitant hf-EEG on a trial-to-trial basis. In the present study we demonstrate this to be the case, validating hf-EEG as a non-invasive probe for fluctuating cortical spike output.

3.2. Methods

Details of the experimental methods used to measure single-unit activity can be found in Section 1.4.2.

3.2.1. Recording of hf-EEG

Somatosensory-evoked EEG potentials (SSEPs) were triggered by electric stimulation of the median nerve and recorded bipolarly using two ball electrodes placed on the dura over the central sulcus. The hf-EEG signals were separated from the wideband response using an acausal band-pass filter (finite impulse response, order 200, Hamming window, cut-off 450–1100 Hz, roll-off 8 dB/decade, attenuation in stop-band 29.1 dB).

In order to assess the quality of hf-EEG recordings the signal-to-noise ratio (SNR) was estimated as the ratio between RMS amplitudes of signal and noise. The signal RMS was calculated in a time window aligned with the hf-EEG burst averaged over all trials (6–13 ms post-stimulus); the noise RMS was calculated from single-trial activity in a later window which did not contain the hf-EEG burst (200–250 ms) and then averaged across all trials. The estimated SNR averaged over all sessions was 0.83 ± 0.10 (mean $\pm$ s.e.m.). For subsequent analysis, only recordings with SNR > 0.9 (60% of original recordings) were selected allowing for a reliable identification of the hf-EEG burst in averages with a low number of trials ($n > 10$). The single-trial SNR

of this reduced set of recordings was 1.21 ± 0.10 (mean ± s.e.m.).

3.2.2. Spike pattern classification

Simultaneously with SSEP the single-unit activity in the somatosensory cortex was recorded using microelectrodes. Spikes of single neurons were discriminated using a cluster cutting method (Section 2.2.1). Spike patterns of bursting neurons were identified by means of PSTH-based clustering algorithm. Full details of the cell selection criteria and clustering algorithm can be found in Section 2.2.

3.2.3. Comparison of hf-EEG wavelets

The hf-EEG were averaged separately over trial sets defined by the neuronal spike patterns. In order to obtain a sufficient SNR for reliable identification of hf-EEG in these averages, only spike patterns that were found in at least 10 trials were further analysed.

The spike-pattern-related hf-EEG averages were compared by means of a root mean square (RMS) measure calculated in the interval covering the entire wavelet (6–13 ms after stimulus onset, cf. bracket in Figure 3.2B). The hf-EEG RMS amplitudes calculated for each waveform separately were compared pairwise and absolute differences were calculated. The significance of the differences was tested by means of a non-parametric bootstrap test (Efron and Tibshirani, 1994). This was implemented by counting how often surrogate hf-EEG RMS differences (calculated after randomly shuffling the trials between patterns) were greater than the original difference (Figure 3.3A). The fraction of such cases in $n = 1000$ random shuffles was taken as the significance level (p-value). Significant deviance ($p < 0.05$) from the shuffled RMS differences was evidence for co-variation between hf-EEG and spike patterns.

As multiple comparisons were performed, the significance level was corrected for each cell separately using the False Discovery Rate method (FDR, q-value) (Benjamini and Hochberg, 1995).

Detailed information on the number of spike patterns detected in all cells and the number of independent comparisons is available in the Appendix (Table A.1).

3.2.4. Variance explained by spike patterns

We estimated the fraction of the total hf-EEG response variance that could be explained by the spike-pattern-related differences. This fraction was calculated as variance in the set of RMS values that were calculated from selective hf-EEG averages related to different spike patterns (cf. Section 3.2.3) divided by the total variance in single-trial hf-EEG RMS values calculated in the same time window without distinguishing different spike patterns.

3.2.5. Correction for subcortical input variations

We tested how much the identified hf-EEG RMS differences might relate to changes in the brainstem responses to the stimulus, which could occur due to changing stimulus efficacy in the periphery, or neural gating of the responses at the brainstem level. All trials were ranked based on the single-trial brainstem hf-EEG power, and then partitioned into 20 subsets each containing 50 trials. From these data, we obtained a recruitment relation between the RMS values of subset-averaged brainstem responses (time window 3–7 ms post-stimulus) and the epidural cortical hf-EEG responses. This relation was fitted with a polynomial (degree 3). Then, for each pair of spike patterns we determined the corresponding brainstem responses and used the polynomial fit to calculate an hf-EEG RMS difference expected from the brainstem responses. This was subtracted from the measured epidural hf-EEG RMS difference, yielding the component of the difference which was unlikely to be explained solely by differences in brainstem responsiveness (Figure 3.4A). Finally, we tested the significance of the residuals using the bootstrap test described in the previous paragraph, for which surrogate RMS values were constructed for both hf-EEG and corresponding brainstem responses.

3.2.6. Timing of spike-pattern-related hf-EEG differences

To investigate how the timing of differences in the hf-EEG related to the timing of spike patterns, we repeated the analysis above using a more narrowly circumscribed temporal window for the calculation of RMS amplitude. Windows were chosen to encompass single peaks of the hf-EEG response, corresponding to single digits of the spike pattern. Statistical testing of differences, and correction for brainstem input fluctuations, were carried out as described above.

3.3. Results

High-frequency surface EEG co-varies with single-neuron response patterns.

In two awake monkeys the median nerve was stimulated electrically to evoke brief (10 ms) epidural hf-EEG wavelets, which were recorded together with extracellular spike responses from S1. Since the focus of this study was on the relation between response patterns of single neurons and hf-EEG we manually discriminated clusters of spike waveforms from extracellular traces and selected only clusters that clearly corresponded to single unit activity (for detailed description of the dataset selection and spike sorting algorithms see Section 2.2.1). In 15 independent recording session selected for the high SNR of hf-EEG signals we identified 17 well-discriminated bursting cells (14 and 3 in each monkey, respectively; see Methods for exact selection criteria and Appendix A for a list of cells). Peri-stimulus time histograms of their spike response exhibited multiple peaks that were well aligned with peaks of the con-

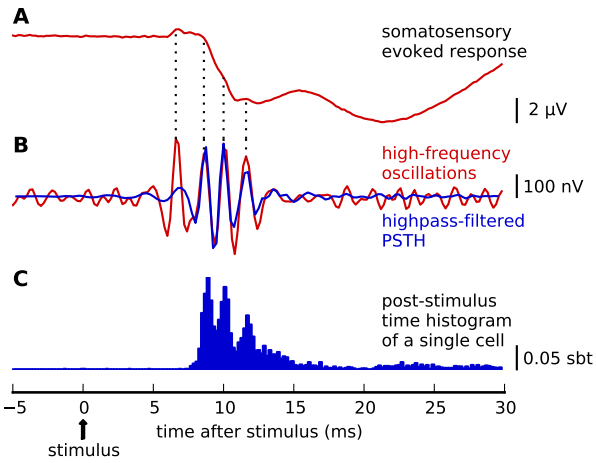

Figure 3.1.: Neural responses to electrical median nerve stimulation. (**A**) Evoked EEG potentials recorded epidurally over the central sulcus (average of 956 trials, bandpass 3 Hz to 2 kHz). The primary somatosensory evoked response consists of slow potential deflections (peaking at 10 ms) related to post-synaptic activity, on top of which small amplitude ripples are superimposed. (**B**) The application of a high-pass filter (450–1100 Hz) reveals that the ripples form a short train of high-frequency oscillations (hf-EEG, red line; note change of amplitude scaling). (**C**) Post-stimulus time histogram (PSTH) of single-neuron spike responses recorded simultaneously with hf-EEG in the somatosensory cortex (normalised PSTH of a sample cell, blue bars; sbt = spikes per bin per trial). Single neurons respond to the stimulation with a burst of spikes which, after trial averaging, sum into a multi-peaked PSTH. Peaks of the PSTH align with the peaks of hf-EEG, which becomes more apparent when the high-pass filtered PSTH (B, blue line) is superimposed on the hf-EEG waveform (B, red line).

comitant hf-EEG (Figure 3.1B,C) indicating that the spikes may directly contribute to hf-EEG (Baker et al., 2003).

As we have previously shown, single-cell spike responses to repeated presentation of the same stimulus varied highly from trial to trial (Chapter 2). These variations were contained in a narrow distribution of spike times around the mean latencies of PSTH peaks and, more interestingly, in the exact arrangement of spikes within a burst. Some temporal spike arrangements recurred often within a single stimulus train allowing for classification into a discrete set of so-called *spike patterns* (see Figure 2.2). Since hf-EEG measured at the dura also manifests considerable variability across stimulation trials, in the following we examined whether there is a trial-to-trial relation between those two processes.

Spike responses of the identified bursting cells were classified into spike patterns with a PSTH-based algorithm (see Section 2.2.3). Next, single-trial hf-EEG wavelets coincident with each of the patterns were split into separate groups and then averaged. Comparing the mean hf-EEG waveforms across spike patterns we found that many diverged in some of the oscillation periods (Figure 3.2B). These differences could not be explained by chance fluctuations, as the root-mean square (RMS) amplitudes of

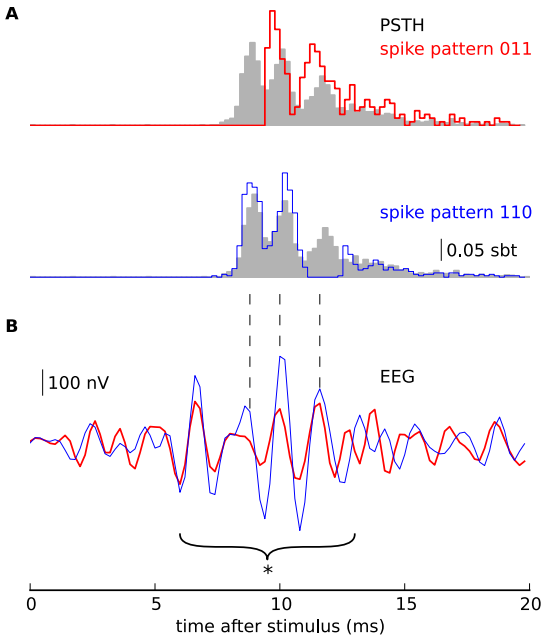

Figure 3.2.: Trial-to-trial variability of single-cell activity is associated with differences in the high-frequency surface EEG recordings. (**A**) Normalised sub-group PSTH of two sample spike patterns in one of the analysed cells (red: pattern 011; blue: pattern 110; grey-bars: all trials; sbt = spikes per bin per trial, cf. Figure 2.2) (**B**) Mean hf-EEG wavelets (red: 114 trials, blue: 293 trials) concomitant with the two different spike patterns differ significantly with respect to their RMS amplitude (calculated over the bracket interval, $^*p < 0.05$, see Methods). The main differences between the waveforms are localised at the peaks of hf-EEG coincident with the major upstrokes of single-cell activity (dashed lines delineate the positions of PSTH peaks). Notably, the first hf-EEG peak at 7 ms is almost identical, reflecting comparable thalamocortical input (Ikeda et al., 2002).

the mean hf-EEG waveforms were significantly different ($p<0.05$, bootstrap test, see Figure 3.3A). Non-matching pairs of other identified spike patterns yielded further instances of significant hf-EEG RMS amplitude differences. The differences were not necessarily localised to the time window concomitant with a missed/extra spike, but rather often extended over multiple PSTH peaks (Figure 3.6).

In the 17 cells selected for analysis we identified a total of 82 spike patterns (median 4 patterns per cell, range 2 to 8). All patterns identified in a single cell were compared pair-wise providing 167 independent comparisons (cf. Table A.1 in the Appendix). In 15 out of 17 cells, at least one pair of spike patterns was accompanied by significantly different hf-EEG RMS amplitudes. Significant differences were found in 50% of all evaluated comparisons (84 out of 167 pairs, corrected for multiple comparison: FDR, $q<0.05$; Figure 3.3B). Spike-pattern-related differences could account for an average of $19 \pm 12\%$ of the total variance in single-trial hf-EEG RMS amplitudes (mean $\pm$ SD, range 3–43%). This fraction is remarkably high given that the remaining variance

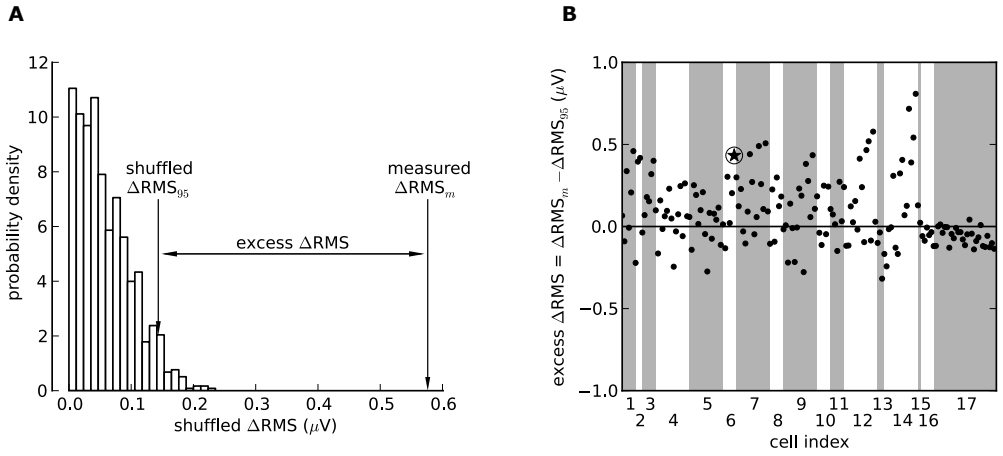

Figure 3.3.: The difference between hf-EEG RMS amplitudes associated with different spike patterns is significantly larger than the difference between random groups of trials. (**A**) The distribution of RMS amplitude differences between spike-pattern-related hf-EEG waveforms after randomly shuffling the trials (see Methods) in an example cell. The real RMS difference between the spike patterns before shuffling (measured $\Delta\mathrm{RMS}_m$) is larger than the 95^{th} percentile of the RMS differences calculated from random shuffles (shuffled $\Delta\mathrm{RMS}_{95}$). (**B**) The excess of the measured ΔRMS over the critical value $\Delta\mathrm{RMS}_{95}$ (excess ΔRMS) for all other identified pattern pairs pooled over all analysed 17 cells (dots; the encircled star denotes the sample pair shown in (A)). The grey and white stripes delimit spike-pattern pairs identified in different cells. A sizeable fraction of points (94 out of 167; 56.3%) lie above the zero line which delimits the significant differences from insignificant ones ($p<0.05$, no correction for multiple comparisons, for corrected values see Results).

includes both neuronal background activity and the band-limited amplifier noise known to permeate EEG recordings.

Input variations can account only partially for the observed variability.

Next, we sought to demarcate possible sources of the correlated trial-to-trial variability between single-cell spike patterns and macroscopic EEG responses. Two possibilities to be distinguished are fluctuations entering the somatosensory pathways either at early stages (periphery, brainstem) or upstream within thalamocortical circuitry. Accordingly, in most sessions (15 of 17 cells) we additionally recorded evoked responses at the brainstem and obtained a calibration curve relating the RMS amplitude of the brainstem evoked potential to that of the cortical hf-EEG (see Section 3.2.5 for details). Pattern-specific averages of brainstem recordings were then compiled (Figure 3.4Aa), and their RMS amplitude determined. These amplitudes were used to read off from the calibration curve the difference in hf-EEG RMS amplitude which would be expected, given the difference in brainstem evoked potential amplitude (Figure 3.4Ab). This was compared with the actual difference in hf-EEG RMS amplitude seen in the pattern-specific averages (Figure 3.4Ac). Although part

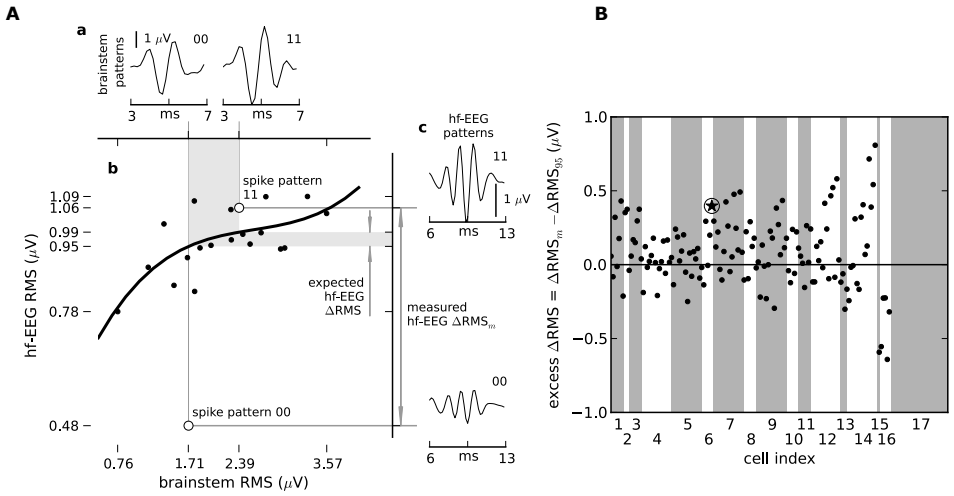

Figure 3.4.: Correction of the measured ΔRMS for subcortical input variations.(**A**) Some spike patterns (for example, patterns 00 and 11 in Ab, open circles) were different not only in terms of cortical (hf-EEG RMS) but also subcortical (brainstem RMS) responses. In order to correct for the subcortical variations, the relation between RMS power of brainstem response and hf-EEG response (dots) was fitted with a 3$^{\text{rd}}$-order polynomial (recruitment curve; Ab, solid line). The recruitment curve was used to transform the difference in RMS of brainstem activations related to two different spike patterns (Aa, two sample patterns with labels in the upper-right corner) into expected hf-EEG ΔRMS that was explained by the subcortical variations (Ab, gray-shaded area). This value was then subtracted from total hf-EEG ΔRMS estimated from real hf-EEG recordings (Ac; measured ΔRMS$_m$) to obtain a corrected measure independent of brainstem variations. (**B**) Significance of input-corrected RMS differences between the spike patterns (compare with Figure 3.3B). After correcting the measured ΔRMS for subcortical input variations still a large fraction of the resulting excess ΔRMS values (86 out of 138; 62.3%) still exceeds the critical value of the statistical test ($p<0.05$, no correction for multiple comparisons, for corrected values see Results). Note that for cells 15 and 17 the brain-stem recordings were not available and corrected ΔRMS could not be calculated.

of the cortical hf-EEG variance could be explained by fluctuations of the subcortical response RMS amplitude, in 78/138 (56%) of single-cell spike pattern pairs with brainstem recordings available there were residual differences exceeding those predicted from the brainstem evoked responses (Figure 3.4B).

Spike-pattern signature is a predictor of hf-EEG RMS amplitude.

To understand which features of the spike patterns are the best predictors for the differences in hf-EEG RMS amplitude, we calculated the mean hf-EEG RMS specific for each pattern and averaged the obtained amplitudes across cells. In agreement with the previous results based on within-cell comparisons, the ensemble analysis revealed co-variations between hf-EEG RMS amplitude and single-cell responses (Figure 3.5).

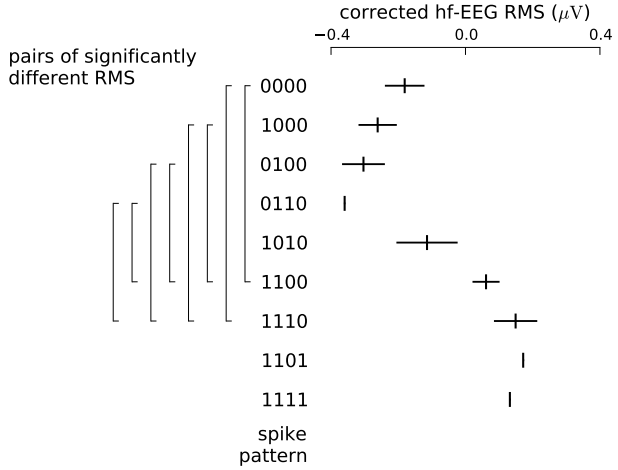

Figure 3.5.: Population-averaged hf-EEG RMS related to different spike patterns (corrected for brainstem variations; ticks and whiskers: mean ± s.e.m.). For some pairs of spike patterns the obtained RMS amplitudes were significantly different (left brackets, pairwise t-test corrected for multiple comparison: FDR $q<0.05$). Note that patterns 0110, 1101 and 1111 were identified in only one cell so that standard error could not be determined.

Nevertheless, the differences were not equally pronounced for all spike patterns: the largest hf-EEG RMS differences were obtained between patterns that differed in number of spikes (Figure 3.5, compare singlets, doublets and triplets), but there was also a tendency for longer first spike latency to be correlated with lower hf-EEG RMS (for example, 0110 and 1100). Thus, both the number of spikes and spike response latency can factor in the prediction of hf-EEG RMS amplitudes.

RMS differences in individual hf-EEG peaks may provide additional information about underlying spike trains.

The significant co-variation between hf-EEG and single-cell spike patterns indicates that there may be a direct relation of the burst of action potentials elicited in a cell and the time course of the very fast components of macroscopic EEG signals. However, the hf-EEG and PSTH measures calculated for pairs of spike patterns reveal differences with unique temporal profiles (Figure 3.6).

Therefore, we investigated quantitatively whether the temporal variations in the hf-EEG amplitude carry additional information about spike patterns. To this end, we looked for spike-pattern-specific differences between RMS values calculated within single hf-EEG peaks (Figure 3.7, lower left) and repeated the significance analysis presented above after centering the hf-EEG RMS window on a single peak of the wavelet at a time. The fraction of cells in which significant RMS differences were found was non-uniformly distributed over the hf-EEG peaks (Figure 3.7, upper right). The shape of the distribution was dependent on the exact pair of compared spike patterns indicating that the individual peak amplitude may provide additional

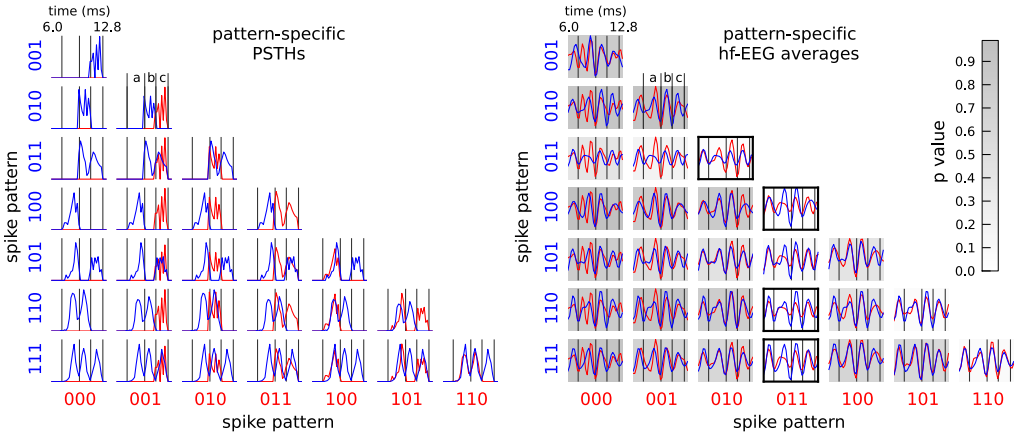

Figure 3.6.: Pairwise comparisons of spike-pattern-specific PSTHs (left triangle) and related hf-EEG averages (right triangle). In each panel neural activity patterns (PSTHs or hf-EEG) related to two different spike patterns are compared: Each waveform represents a single spike pattern whose identity is given by the colour-coded labels at the left or bottom of the panel. (**Left**) Normalised PSTHs show prominent differences in single-neuron activity within discrete bins used for the classification of the spike patterns, documenting a correct classification (spike events labelled by a, b, c and delimited by vertical lines). (**Right**) The corresponding comparison of hf-EEG sub-averages calculated for each spike pattern reveals differences in the amplitude of consecutive hf-EEG peaks. In contrast to PSTHs, these differences are not localised to single spike events (a,b,c); rather, they extend over multiple peaks. Notably, the significance of the total hf-EEG RMS amplitude differences, which is depicted by the panel's background shading (p-value, for calculation details see Methods and Figure 3.3A), is variable across spike-pattern pairs. Significantly different patterns ($p<0.05$) are marked by a black box.

information about the spike pattern underlying a particular hf-EEG response. However, differences in hf-EEG were seen not just at the peaks corresponding to digits which differed between spike patterns (filled bars, Figure 3.7), but also in hf-EEG components before and after the time when spike patterns differed (open bars).

Population data on the timing relation between spike pattern and hf-EEG differences are presented in Figure 3.8 as a contingency table. The area of each square illustrates the number of instances when an hf-EEG peak differed (rows), given a difference in a particular digit of the spike pattern (columns). If the hf-EEG wavelet altered only at the times when the spike pattern was different, the diagonal elements of this contingency table (between solid and dashed lines) would dominate. If hf-EEG peaks were altered only after the time when spike patterns differed (possibly indicating that spike pattern changes cause hf-EEG changes), elements above the dashed line would dominate. Finally, if hf-EEG fluctuations preceded spike pattern differences, elements below the solid line would dominate. Significant effects were seen in all three sections of the contingency table. There is thus no simple relationship between the timing of trial-to-trial variations in spike patterns and hf-EEG.

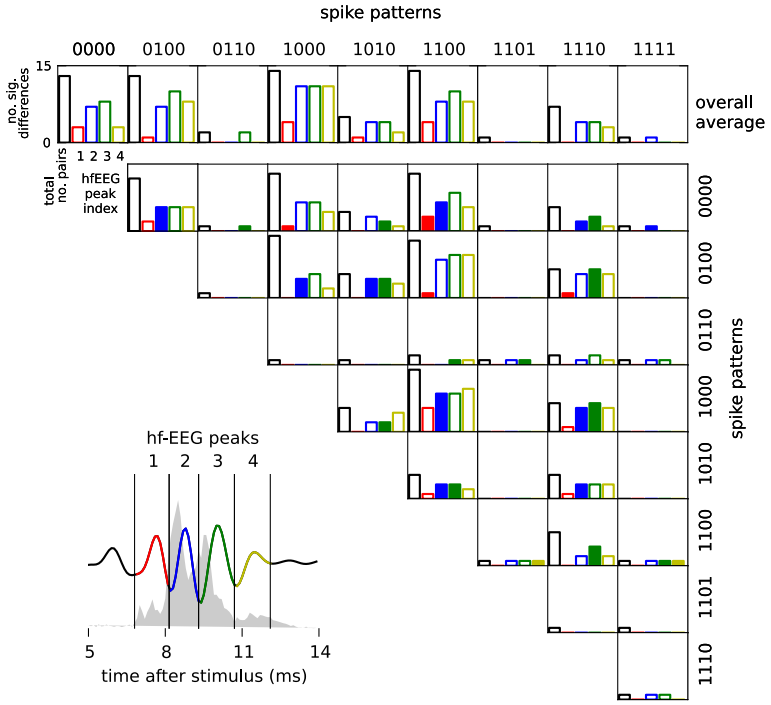

Figure 3.7.: The amplitudes of individual hf-EEG peaks co-vary with spike patterns of a single cell, but they do not show a regular one-to-one relation with individual spike events. Four individual peaks of hf-EEG were identified visually after averaging across all trials and all recorded cells (inset at bottom left, each peak is shown in a different colour). The peaks were segmented into non-overlapping windows (marked by vertical lines) whose positions are superimposed on the ensemble PSTH (grey-shaded area, average across all cells) to emphasize their relation to spike events used for spike pattern classification. The RMS amplitude within each of those hf-EEG windows was corrected for input variations (based on recruitment curves calculated for each window) and compared between all possible pairs of concomitant spike patterns. Each row and column of the mosaic plot (upper right) corresponds either to a single pattern from the pair as identified by its respective label (top and right of the plot; for cells with less than four spike events 0s were appended to the spike-pattern string) or overall average across all trials (top row). Bars within each frame show the total number of comparisons (black bars) and the number of those comparisons that yielded significant ($p < 0.05$) RMS differences in each of the hf-EEG windows (colour-coded bars). In many instances the differences in hf-EEG peaks paralleled differences in spike occurrence in the same latency window (filled bars; compare also the digits of spike patterns labels), but significant RMS differences were also detected in peaks that did not coincide with spike pattern differences (open bars).

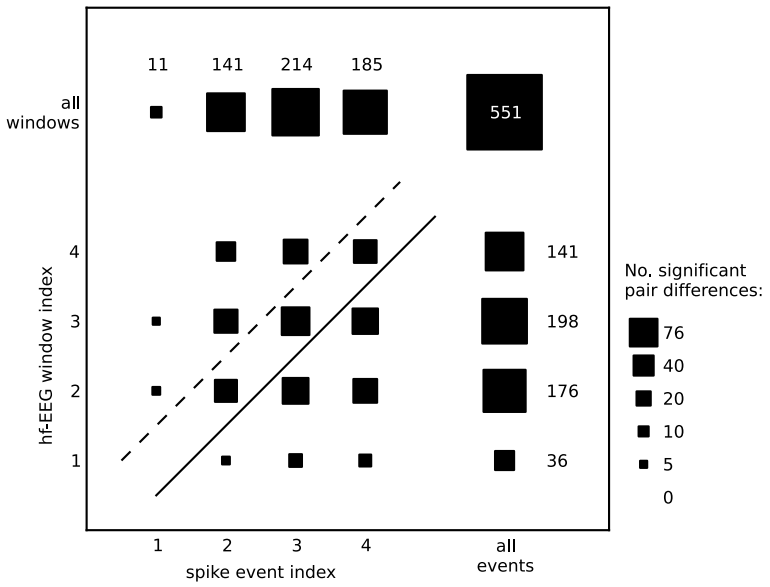

Figure 3.8.: Contingency table summarizing the correspondence between significant differences in hf-EEG peaks and spike occurrence/omissions. The area of each square reflects the number of comparisons where differences in a specific hf-EEG window (rows) and spike event (columns) coincided; the top row and rightmost column show marginals after summing all rows and columns, respectively. The data points can be divided into three main classes: hf-EEG differences following spike pattern differences (above the dashed line), hf-EEG differences occurring simultaneously with spike pattern differences (between the dashed and solid lines) and hf-EEG differences preceding spike pattern differences (below the solid line).

3.4. Discussion

Sources of high-frequency oscillations

High-frequency oscillations (f > 400 Hz) have been described in many brain areas (Baker et al., 2003; Curio et al., 1994; Barth, 2003; Bragin et al., 1999; Funke and Kerscher, 2000; Hanajima et al., 2004) following both direct nerve and natural sensory stimulation, or emerging spontaneously prior to epileptic discharges (Jirsch et al., 2006). Despite this ubiquity, little is known about the microscopic mechanisms underlying hf-EEG. Detailed laminar field potential recordings conducted in monkeys after median nerve stimulation revealed that hf-EEG is generated locally within cortex area 3b and area 1 (Shimazu et al., 2000). Subsequent single-unit recordings in area 3b identified a population of neurons that elicited spike bursts in phase with

peaks of the concomitant hf-EEG (Baker et al., 2003). In the same study neurons that responded only with single spikes also showed a preference for firing in the same latency windows defined by the peaks of hf-EEG.

Here, we investigated whether hf-EEG may be sensitive even to action potentials *patterns* generated by cortical neurons. To this end, we compared single-unit activity and concomitant hf-EEG on a trial-to-trial basis in each cell independently. We found that a limited set of distinct spike patterns sufficed to identify significantly different macroscopic hf-EEG responses. This finding establishes a close link between neuronal spike firing patterns and EEG amplitude, thereby bridging the gap between microscopic and macroscopic levels of neural activity.

Covariation between spike pattern and hf-EEG

Several studies have reported significant correlations between intracortically recorded local field potentials (LFP) in the high-gamma band (30–100 Hz) and multiunit activity recorded from the same electrode. Based on this finding it was concluded that gamma-range LFP power reflects the activity of local neuronal populations surrounding the electrode (Eckhorn et al., 1988; Eckhorn and Thomas, 1993; Gray and Singer, 1989; Frien and Eckhorn, 2000; Fries et al., 2001; Engel et al., 2001; Berens et al., 2008; Belitski et al., 2008; Katzner et al., 2009; König et al., 1995; Siegel and König, 2003). Since surface EEG is remote from the sources of the recorded activity it is less likely to reflect localised spiking of small populations of neurons. Surprisingly, recent experimental studies showed that surface EEG in high-gamma frequencies is correlated with multiunit activity in the visual cortex of alert monkeys during presentation of natural movies (Whittingstall and Logothetis, 2009). These findings raise an important question: Is it possible to enhance the informative value of EEG signals further by considering even higher frequency ranges?

Since the EEG spectrum above 200 Hz has typically very low power these high frequencies are usually not considered to be a measure of neuronal activity, but rather taken as a sign of environmental noise or muscle activity (Whitham et al., 2007). However, as demonstrated by the present study, some high-frequency components are genuine correlates of neuronal activity. Specifically, we found that both the amplitude of hf-EEG and its time course correlate with single-unit activity on a trial-to-trial basis. Our novel analysis based on spike response clustering suggests that the precise temporal sequences of spikes generated by neurons in a single trial are related to the magnitude and time course of the population response recorded by macroscopic epidural hf-EEG activity.

How can such a high specificity of the EEG signal came about? Traditionally EEG is believed to provide only a rather coarse measure of neuronal activity (see Section 1.1.3). In contrast to this widespread assumption, simulation studies have shown that the current dipole generated by sodium spikes can be surprisingly strong, so that a group of 50000 synchronous spikes could generate an extracellular field detectable with scalp EEG (Murakami and Okada, 2006, see also Table 1.1). Nevertheless, it has been hypothesized that under normal conditions single neurons are only weakly

synchronised and temporal spike jitter cancels their contribution to the macroscopic field. Recent modelling studies indicate that even a small increase in synchrony can lead to a substantial amplitude increase of the spontaneous EEG (Nunez and Srinivasan, 2005; Ray et al., 2008; Murakami et al., 2003).

Those results also shed new light on the cellular substrates of hf-EEG. Median nerve stimulation results in massively synchronous activity in the primary somatosensory cortex (Peterson et al., 1995; Baker et al., 2003). Synchronous co-activation of a larger group of neurons could then explain the observed correlation between single-neuron and population responses averaged across trials.

The trial-to-trial co-variation of single-unit activity and hf-EEG found in the present study indicates, in addition, that synchronised activity is not driven solely by the external stimulation (constant across repetitions), but also by endogenous factors, for example intra-cortical connectivity (cf. Averbeck et al., 2006). Mutual interactions could enable a population of neurons to produce the same spike patterns in each trial explaining the cross-pattern differences in hf-EEG amplitude. In this case the spikes composing the spike patterns would summate and generate macroscopic potentials of a time course similar to the PSTH of that specific pattern.

Alternatively, there could be variation in spike patterns across the neuronal population, but the nature of the pattern distribution and consequently the macroscopic population response could change from trial to trial. In this case no one-to-one relation between single-cell PSTH pattern and hf-EEG would be observed, but even then the spike patterns that more frequently coincided with a synchronous population response would also be accompanied by higher-amplitude hf-EEG. The latter hypothesis is supported by the observation that the spike pattern variability is reflected more strongly by the amplitude of hf-EEG (Figure 3.3) than by its shape (Figures 3.6, 3.7 and 3.8). In the following chapter, we will test this hypothesis by means of computational modelling. However, further experimental evidence in favour of either of these hypotheses could be obtained from simultaneous recordings of multiple bursting neurons using microelectrode arrays.

Sources of trial-to-trial variability

As argued in the previous paragraph, the co-variability between hf-EEG and single-neuron activity most likely results from a coordinated modulation of responses of large number of cells. Consequently, one component of the variability of neuronal responses cannot be private to a single cell but must be shared across the population (Tsodyks et al., 1999). One source of shared variability undoubtedly arises at the early stages of the somatosensory system due to variable stimulus efficacy or subcortical processing. However, even after accounting for response amplitude fluctuations at the first relay station of the somatosensory pathway (brainstem, cf. Figure 1.7), we still found a significant covariation between hf-EEG and single-cell spike patterns. This indicates further shared variability upstream to the brainstem, i.e., in the thalamus and/or cortex. Notably, the first EEG wavelet peak has a lower number of significant pair differences than any later peak (hf-EEG window index 1 in Figure 3.8; see also an

example in Figure 3.2B) suggesting that the thalamic input contributes less variability than later intracortically generated response components.

Since the thalamocortical system is involved in the regulation of arousal and attention (Portas et al., 1998), this variability could reflect transitions between different brain states, such as phases of sleep, or variations in the levels of consciousness, attention, expectation and learning (Chapman et al., 1988; Li et al., 1999; Kenet et al., 2003; Rosanova and Timofeev, 2005). The different brain states could then alter sensory responses explaining the trial-to-trial variability of both spike patterns and hf-EEG responses (Fontanini and Katz, 2008; Fox et al., 2006). In the present study subjects stayed awake during the recordings, so that the remaining variability must reflect different attentive states or learning. Since the latter usually occurs at much slower time scale, attentional modulation is left as the most likely source of variability. In support of this, non-invasive experiments performed in healthy human subjects (Gobbelé et al., 2000; Halboni et al., 2000; Klostermann et al., 2001) showed that the amplitude of scalp hf-EEG is sensitive to specific neural conditions preceding the stimulus, such as sleep phases and fluctuating vigilance or attention.

Relation to hf-EEG recorded non-invasively in humans

Since high-frequency response components can be reliably recorded from the human scalp in a standard paradigm for acquisition of somatosensory evoked magnetic fields or electric potentials (Curio et al., 1994; Hashimoto et al., 1996) the present findings have potentially far-reaching implications for human noninvasive neurophysiology. However, the signal attenuation due to the skull resistivity substantially diminishes the signal-to-noise ratio of scalp EEG. While the amplitude ratio between low- and high-frequency EEG responses is similar in scalp and epidural hf-EEG, the signal-to-noise ratio of non-invasive measurements is at least one order of magnitude smaller than in the present invasive study. Nevertheless, rapid advances in EEG amplifier technology (Scheer et al., 2006), de-noising algorithms (Celka et al., 2008) and multimodal recording paradigms (Ritter et al., 2008) may help to alleviate this problem. Consequently, recordings of high-frequency activity may eventually provide a non-invasive window on fluctuating cortical spike activity in man.

4. Minimal model of cortical bursting and population activity

In previous chapters it has been demonstrated that single cells in the S1 cortex can respond to synchronised inputs with barrages of spikes elicited at sub-millisecond precision. Interestingly, the responses to repeated presentation of the same stimulus are quite variable and form discrete classes of temporally arranged spikes, also called spike patterns (Chapter 2). In each of the patterns, spikes occur in narrow temporal windows that are the same for all patterns, but the occupancy of the windows (occurrence or omission of a spike) differ from pattern to pattern. As pointed out before (Section 2.4), the mechanisms of generation of such neuronal responses are not yet clear.

The short intervals (ISI mode $\approx$ 1.3 ms) between consecutive spikes may suggest the contribution of special membrane currents that normally lead to bursting. Fast bursting (ISI $<$ 300 Hz) has been found in a class of cortical pyramidal cells (chattering neurons; Gray and McCormick, 1996). Detailed studies of electrophysiological properties of those cells revealed that the generation of bursts depends on an interplay between depolarising and hyperpolarising currents (Brumberg et al., 2000).

In this chapter, we test an alternative mechanism in which the precise patterns of single-cell responses stem from the interplay between synaptic inputs and intrinsic refractory properties of the cell. To this end, we develop a simple model capturing the two processes and fit the parameters of the model to extracellular recordings of single-unit activity in the somatosensory cortex. The interpretation of the obtained parameters brings a new understanding of the mechanisms of bursting in S1 neurons. In addition, we show that the simple model can explain a wide range of experimental data and make testable predictions regarding the relation between the single-cell response and population activity (Chapter 3).

4.1. Methods

4.1.1. Spike train probability model

We assume that a spike emission is a random point process with the probability:

$$p\left(\text{spike in interval } [t, t+dt] | \{t_i\}\right) = \lambda(t|\{t_i\})dt, \tag{4.1}$$

where $\{t_i\}$ denotes the spiking history and $\lambda(t|\{t_i\})$ is the conditional intensity.

The conditional intensity $\lambda(t|\{t_i\})$ is assumed to have a Markov property i.e. it is

conditioned only on the time of occurrence of the last spike t_{last}: $\lambda(t|\{t_i\}) = \lambda(t, t_{\text{last}})$. A further assumption is that the firing rate modulation and refractory effects are multiplicative (Berry and Meister, 1998):

$$\lambda(t|\{t_i\}) = q(t)w(\Delta t), \tag{4.2}$$

where $q(t)$ is the intensity function, $w(\Delta t)$ is the recovery function and Δt is the time from the last spike.

4.1.2. Model fitting

The parameters of the model: the intensity function $q(t)$ and the recovery function $w(\Delta t)$, are defined on a per-bin basis (bin width: 0.05 ms) and fitted to experimental data by means of the maximum likelihood approach. The likelihood function $L(q; w|\{t_i\})$ is obtained by log-transforming the probability function of an inhomogeneous Poisson process with the conditional intensity (4.2) (Dayan and Abbott, 2001; Johnson and Swami, 1983):

$$L(q; w|\{t_i\}) = -\int_0^T q(t)w(t - t_{\text{last}})dt + \sum_i \ln[q(t_i)w(t_i - t_{\text{last}})]. \tag{4.3}$$

where T is the duration of response ($T = 30$ ms), i is the spike index and t_i denotes the times of occurrence of consecutive spikes. The likelihood function is maximised by means of an iterative expectation-maximization (EM) algorithm, which guarantees that the global maximum is reached (Miller, 1985). In addition, we ensure that after 5 ms the model neuron recovers from refractoriness by setting the recovery function to unity for long intervals, such that $w(\Delta t > 5\,\text{ms}) = 1$.

The results obtained with the spike train probability model were compared to the inhomogeneous Poisson model without refractory period ($w(\Delta t) = 1$ for all $\Delta t > 0$; Dayan and Abbott, 2001). The model is fully characterised by its intensity function $q^{\text{poisson}}(t)$, which we estimated from the experimental spike trains with the post-stimulus time histogram (PSTH, bin width: 0.05 ms).

4.1.3. Model validation

Dataset was divided into two non-overlapping subsets of equal size: the training and validation set. The parameters of the model were fitted to the training set. Based on these parameters 1000 spike trains were simulated. The goodness of fit was evaluated based on the difference between one of two statistics (PSTH, bin size 0.2 ms or spike pattern distribution, see Section 2.2.3) calculated separately for the simulated and validation spike trains. The difference was quantified by the sum of squared and normalised residuals ("model error", χ^2 statistics) (cf. Rauch et al., 2003):

$$Err(\mathbf{X}^{\text{model}}, \mathbf{X}^{\text{validate}}) = \sum_{i=1}^{N} \frac{\left(X_i^{\text{model}} - X_i^{\text{validate}}\right)^2}{X_i^{\text{validate}}}, \tag{4.4}$$

where $\mathbf{X}$ denotes the statistics vector (PSTH or spike pattern distribution), N is the size of the vector (where $\mathbf{X}$ is the PSTH N is the number of bins: $N = 150$; where $\mathbf{X}$ is the spike pattern distribution N is the number of identified spike patterns: $N \leq 16$), i enumerates elements of the statistics vector (bins of PSTH or spike patterns), and $\mathbf{X}^{\text{model}}$ and $\mathbf{X}^{\text{validate}}$ denote the statistics calculated from the modelled spike trains and validation spike trains, respectively.

The model error $Err(\mathbf{X}^{\text{model}}, \mathbf{X}^{\text{validate}})$ was compared against the error between the training and validation set $Err(\mathbf{X}^{\text{train}}, \mathbf{X}^{\text{validate}})$ ("reference error"). The significance of the difference between these two measures was quantified by means of the F-test with $(N-1, N-1)$ degrees of freedom (Barlow, 1989), where:

$$F = Err(\mathbf{X}^{\text{model}}, \mathbf{X}^{\text{validate}}) / Err(\mathbf{X}^{\text{train}}, \mathbf{X}^{\text{validate}}). \tag{4.5}$$

4.1.4. Serial correlations

From the responses of single cells (response window $t \in [0, 50]$ ms after stimulus) we identified spike triplets defined as three consecutive spikes separated by intervals shorter than 4 ms. Next, we calculated Pearson's correlation between the interspike intervals (ISIs) of the first and the second spike and the second and the third spike in the triplet (r_{data}). We compared the estimated r_{data} to the correlation coefficient calculated from surrogate data simulated with a spike train probability model whose parameters were fitted to the experimental spike trains (r_{model}, same number of trials). The significance of the differences between correlation coefficients found in simulated and experimental ISIs was tested by means of a bootstrap test. To this end, r_{model} was calculated from 1000 independently simulated datasets and the resulting coefficients were compared to r_{data}. The fraction of times for which r_{model} was greater (or smaller) than r_{data} was taken as the p value of the test (two-sided bootstrap test).

4.1.5. Population model

Population response was calculated from a simulated ensemble of 5000 identical neurons. The parameters of the spike train probability model were fitted to the responses of the analyzed cell and shared by all model neurons. In each trial j the intensity function of all neurons was modulated by a multiplicative factor (gain, G_j): $q_j(t) = G_j q(t)$, where gain G_j was set randomly to one of two values: $G_j \in \{0.8, 1.2\}$. From the obtained single-trial single-cell responses the total population response was calculated by summing the binned spike responses of all cells (bin size 0.2 ms) and subsequent band-pass filtering (400 – 1200 Hz).

Population correlates of single-cell spike patterns were identified by averaging the population responses sorted according to the co-occurring spike patterns of a single cell randomly selected from the ensemble. The spike pattern classification was based on the occurrence/omission of spikes in a discrete sequence of spiking "windows" (see Section 2.2.3). The RMS amplitude of the pattern-specific average was compared with the experimentally-obtained hf-EEG related to the same spike pattern of a

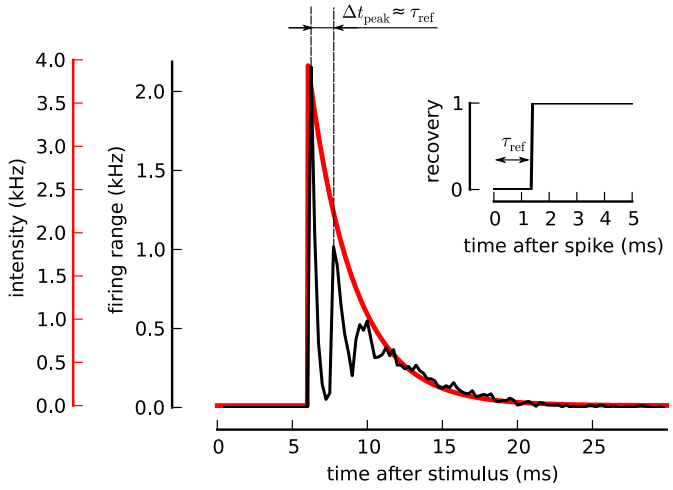

Figure 4.1.: Simulation results of the spike train probability model with arbitrary parameters. Spike trains were generated from the model characterised by an exponentially decaying intensity function ($q(t) = 4\,\exp[-(t - 6\,\text{ms})/3\,\text{ms}]\,\text{Hz}$ for $t \geq 6\,\text{ms}$ and 0 otherwise, red line) and a recovery function implementing the absolute refractory period ($w(\Delta t) = 1$ for $\Delta t \geq \tau_{\text{ref}} = 1.4\,\text{ms}$ and 0 otherwise, inset). PSTH of simulated 1000 response trials (black line) contains characteristic peaks of decreasing amplitudes and increasing widths that are separated by intervals approximately equal to the refractory period ($\Delta t_{\text{peak}} \approx 1.4\,\text{ms}$). Note the similarity to the PSTH calculated from spikes of cortical neurons triggered by the median nerve stimulation (compare with Figure 3.1C).

recorded cell (cf. Section 3.2.3). The similarity of the values across different spike patterns was quantified by means of Pearson's correlation coefficient.

4.2. Results

We propose a phenomenological model of cortical bursting that is based on two observations about the neuronal function: intense and coincident synaptic inputs from thalamocortical neurons (Bruno and Sakmann, 2006; Hanajima et al., 2004; Swadlow and Gusev, 2001; Gil et al., 1999; Cruikshank et al., 2007) and refractoriness limiting the maximum fire rate (Berry and Meister, 1998; Gray, 1967; Kara et al., 2000). In order to illustrate the effects of these two phenomena on neuronal responses we simulated a probabilistic Poisson-like model (the spike train probability model, see Section 4.1.1) with an exponentially decaying intensity function, which may be interpreted as the synaptic drive, and an absolute refractory period $\tau_{\text{ref}} = 1.4\,\text{ms}$ (Figure 4.1). The post-stimulus time histogram (PSTH) of the simulated spike responses reproduces main features of the PSTH obtained from experimental data (see Figure 2.2). Specifically, the absolute refractory period leads to an appearance of multiple peaks in the PSTH that are typical for cortical burst responses triggered by peripheral nerve stimulation (see Chapter 2). Moreover, in agreement with experi-

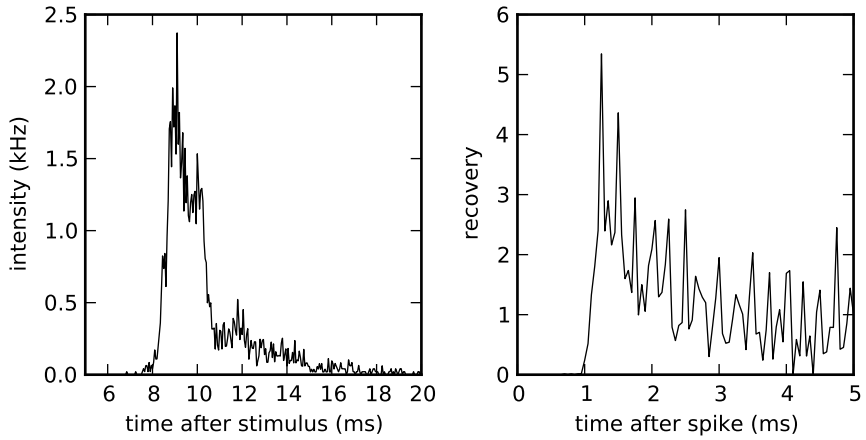

Figure 4.2.: Estimated parameters of the model: intensity function (left) and recovery function (right). The functions were sampled with a period of 0.05 ms. The recovery function for intervals longer than 5 ms cannot be estimated, because there are not enough spikes separated by intervals of this length. Therefore we impose the constraint that $w(\Delta t > 5\,\mathrm{ms}) = 1$

mental findings the first peak of the PSTH is narrowest reflecting the precise spike timing that is induced by the high amplitude of intensity function at the response onset. Subsequent decay of the function leads to a gradual widening of the peaks and decrease of their amplitude.

4.2.1. Fitted parameters

In order to test whether the model can reproduce the fine details of neuronal responses, we fitted its parameters to the spike trains produced by neurons in the somatosensory cortex (area 3b) after electrical stimulation of the median nerve (Figure 4.2, for experimental methods see Section 1.4.2). Although the parameters do not have a straightforward biophysical interpretation, the intensity function can be related to the synaptic input of the neuron as it reflects the stimulus not distorted by a history-dependent nonlinearity (Berry and Meister, 1998; Johnson and Swami, 1983). When compared to the observed firing rate (PSTH, Figure 4.3, left, dark blue) the prominent dips of spike emission probability are largely diminished (Figure 4.2, left). Although the maximum of the function is much above the rate at which individual neurons can fire spikes, the maximum firing rate of the model neuron is limited by refractoriness as quantified by the recovery function (Figure 4.2, right). The recovery function shows that in agreement with properties of biological neurons the model neuron is non-responsive ($w = 0$) for the first 1 ms after emitting a spike (absolute refractory period), but after a few milliseconds fully recovers from the refractoriness returning to the rest state ($w = 1$). Interestingly enough, immediately after the absolute refractory period the recovery function overshoots, largely

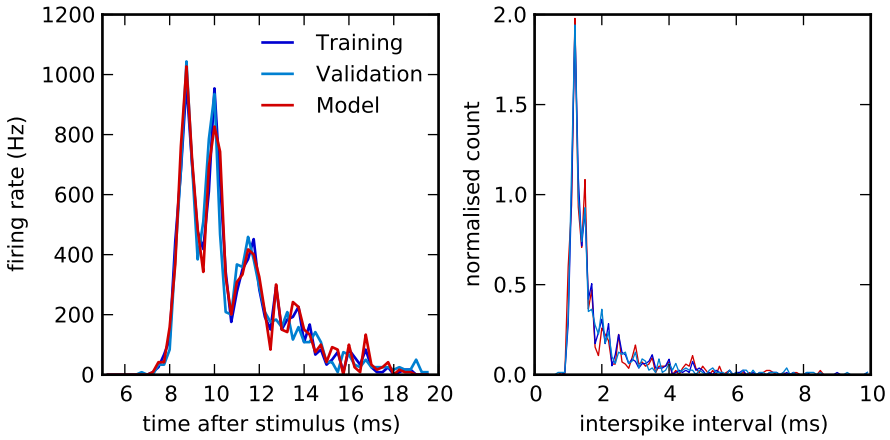

Figure 4.3.: Cross-validation of the spike-train model. Comparison of PSTHs (left) and ISI histograms (right) of the training data (dark blue line), validation data (light blue line) and model data (red line). The validation set was not used in the fitting procedure. Nevertheless, the deviation of the model from the validation data is not much larger than the variation inside the data set ($F = 1.27$, $p < 0.05$, see Methods for definition)

exceeding the rest value. This phenomenon may be interpreted as a facilitation of a spike initiation, which has been found in cellular membranes exhibiting subthreshold resonance (Engel et al., 2008; Hutcheon et al., 1996; Verechtchaguina et al., 2006). However, it may also result from violating the assumptions of the model, for example the independence of the recovery function from the input strength (Koyama and Kass, 2008; Reich et al., 1998).

4.2.2. Model validation

The peri-stimulus time histogram and interspike interval distribution of the fitted data ("training") and corresponding simulated responses ("model") are shown in Figure 4.3 (blue and red lines, respectively). The simulation results fit very well the experimental data thus validating the fitting procedure.

In order to check whether the good match between the model and the data is not a result of an over-fitting, we performed cross-validation. First, the data set was divided into two subsets: training data and validation data. The model was fitted only to the first subset and then the results of the simulation were validated on the second. The PSTH of the simulated spike train reproduces both training and validation data even though it was fitted only to the former (Figure 4.3, left). We quantified the similarity by means of a sum of squared differences between the model PSTH and validation set PSTH ("model error", see Methods). Since a fraction of this difference is due to response variability present in the data set, we compared the "model error" to the error calculated between two different subsets of the same data set: the training subset and a validation subset ("reference error"). The "model

error" and the "reference error" could not be significantly distinguished (F-test, $p < 0.05$) indicating that the model optimally captured the features of both training and validation set without considerable over-fitting.

The parameters of the model were fitted to each of available cells yielding similar results. Importantly, an application of the cross-validation procedure revealed that in 9 out of 17 cells the PSTH simulated with the model was not significantly different from the PSTH calculated from the recorded spike trains (F-test, $F = 0.59 - 1.3$, $p < 0.05$). In 4 cells only small deviations of the modelled PSTH from the real PSTH were found ($F = 1.5 - 2$) and in the remaining 4 cells the deviations were large ($F = 2.96 - 9.1$). Nevertheless, in all of the cases the differences were rather local and all estimates were used in the further analysis.

4.2.3. Model predictions

So far the model has been shown to fit well to the data confirming its assumptions. However, the utility of the model can be only confirmed if it can predict features that are not apparent from the data used to estimate the model parameters. Here, we investigate two properties of the model corresponding to the novel experimental results of the previous chapters: the distribution of spike patterns (Chapter 2) and co-variation between single-cell and population responses (Chapter 3).

Spike patterns distribution

As we have shown in Chapter 2, neuronal responses to identical stimuli are variable. In order to quantify the trial-to-trial variability, we sorted single-trial spike trains into spike patterns as described in Section 2.2.3 (see also Figure 2.2). The distribution of spike pattern in the experimental data (Figure 4.4, blue bars) was found to be similar to the distribution obtained from data simulated with the present model (Figure 4.4, red bars). In contrast, spike patterns produced by a inhomogeneous Poisson model without a refractory period (Figure 4.4, white) appeared at frequencies much different from the experimental data, despite the fact that the overall PSTHs were identical (not shown).

In order to quantify the similarity between the experimental and modelled spike patterns a cross-validation procedure was applied as described in the previous section. To this end, the model was first fitted to the training set and then the residuals between spike patterns distribution in simulated data and validation set were calculated. The sum of squared and normalised residuals was used to quantify the dissimilarity between those distributions (see Methods). Accordingly, the same measure was calculated between the training and validation set to quantify intrinsic variability in the responses. The comparison of both values did not reveal significant deviations of the spike-pattern distribution estimated with the model from the experimental distribution (F-test, $p < 0.05$). In total, in 11 of 17 examined cells we did not find significant deviations between the model and experimental distributions..

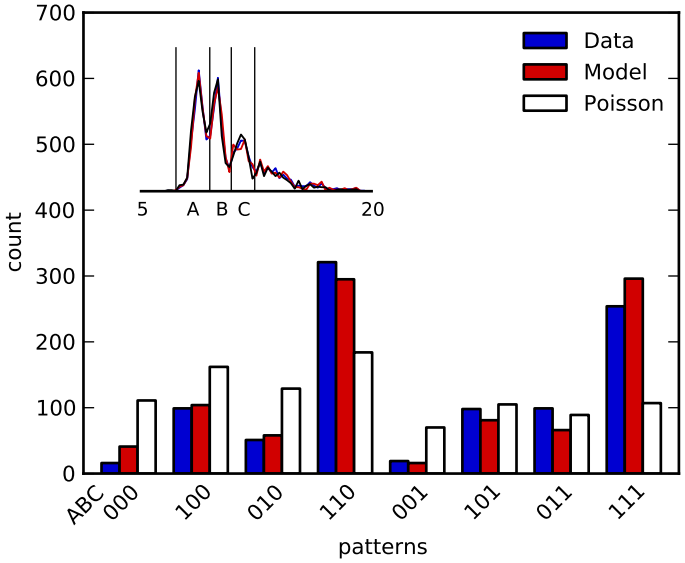

Figure 4.4.: Firing patterns distribution obtained from the data (blue bars), spike train probability model with refractory period (red bars) and the inhomogeneous Poisson model without refractory period (white bars). The firing rate of the Poisson model was estimated by a PSTH with bin size 0.05 ms.

Serial correlations

The good correspondence between experimental and modelled spike-pattern distribution indicates that the shape of the mean firing frequency and interspike intervals (ISIs) histogram is enough to explain the responses of cortical neurons. Specifically, the correlations between consecutive ISIs (serial correlations) do not seem to play an important role. Since this finding provides an important hint regarding the biophysical mechanisms behind the bursting responses to somatosensory stimulation, we corroborated it by direct calculation of the serial correlations in the experimental series of ISIs (Figure 4.5, left). Since serial correlations may be induced by a time-varying spike rate, even if the consecutive ISIs are not causally related, we compared the results to the correlation predicted from the present model (Figure 4.5, right). The latter does not assume any correlations between non-neighbouring spikes, which is equivalent to an assumption of uncorrelated ISIs, so the eventual serial correlations can be solely produced by spike rate variations. Comparison between the simulated and experimental serial correlations revealed that in 8 out of 17 cells they were not significantly different (two-sided bootstrap test, see Section 4.1.4) confirming that the higher-order spike correlations extending over the last spike did not contribute to the cell's responses. In further 6 cells the correlation coefficient was significantly larger or smaller and in the remaining 3 cells the coefficient could not be determined because of a low number of triplets identified in responses. It remains to be investigated whether the prediction of the responses of the cells for which significant serial

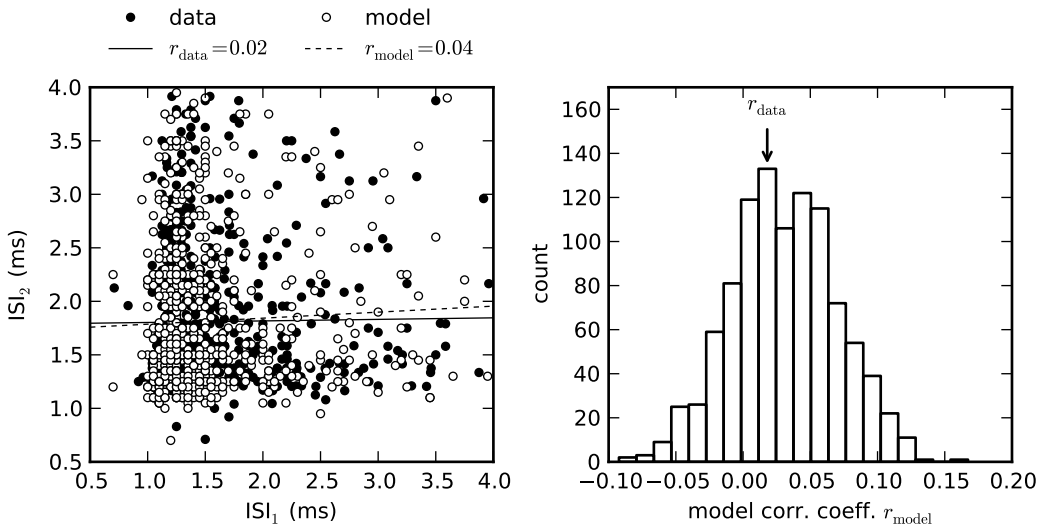

Figure 4.5.: Determination of serial correlations in neuronal responses. (**Left**) Scatter plot of two consecutive interspike intervals (ISIs) within spike triplets calculated from the experimental data (filled circles) and simulated responses (empty circles). Serial correlations (Pearson's correlation coefficient) found in the experimental intervals (r_{data}) differ only slightly from the respective correlations predicted by the model (r_{model}, see values in the legend, solid and dashed lines represent the best linear fit to the experimental and model data, respectively). (**Right**) Repeated Monte-Carlo simulations of the model provide the distribution of serial correlations consistent with the model (empty bars); experimental correlation coefficient (vertical arrow, r_{data}) is likely to be drawn from the estimated distribution and thus we may conclude that it does not significantly differ from the predictions of the model (two-sided test, $p = 0.81$).

correlations were found will improve after including the effects into the model.

Ensemble firing pattern covariation

In Chapter 3 we showed that there is a significant correlation between firing patterns recorded from a cortical neuron and concomitant high-frequency local EEG activation. For each spike pattern we determined the mean EEG waveform and then the RMS amplitude of all the obtained waveforms were compared pairwise. In many of such comparisons we found significant differences between hf-EEG waveforms related to single spike patterns (see Figure 3.5). In Chapter 3 we stipulated that the relation between responses of a single cell and macroscopic EEG activity may result from coordinated activity of multiple neurons.

In order to test the hypothesis, it is necessary to extend the model to a population of multiple neurons. We assume that the neurons are correlated because of shared inputs, which could reflect, for example, feed-forward inputs from lower stages of the processing pathway (Shadlen and Newsome, 1998), mean activity in a recurrent

network (Shu et al., 2003) or neuromodulatory signals (Gil et al., 1997).

These inputs could modulate various neuronal properties, including the total synaptic drive, time of recovery after spiking or response latency. In the model we chose to vary the intensity function reproducing the changes in neuronal responses due to fluctuations in excitability, synaptic strength or total synaptic input. In order to investigate the effect of the modulation on population response we simulated 5000 identical model neurons with the parameters estimated from the experimental data. From the simulated spike trains we estimated the population PSTH and applied a high-pass filter to obtain an estimate of a high-frequency population signal. The simulation was repeated with different input intensities modelled by means of scaling the intensity function by a gain factor G (see Methods). In Figure 4.6A we compare the population signals obtained by simulating the modified model with a low (G=0.8) and high gain (G=1.2): the signals differ slightly in amplitude, yielding a higher amplitude of population signal in response to inputs modulated by a higher gain.

Next, spike responses of a single neuron from the population were registered over 1000 independent repetitions for both low and high gain. The resulting spike trains were classified into spike patterns to find how frequently each pattern reappears over repeated simulations (Figure 4.6B). Again we found that the frequencies of individual spike patterns co-varied with the gain: some patterns (for example 100) occur more frequently at low gain, while others (for example 110) tend to occur more often at high gain.

The concurrent dependence of population signals and single-cell spike pattern distribution on the common input (gain, G), may explain the correlation between single cell responses and macroscopic population activity found in experimental data. Spike patterns which are more frequent at low gain will coincide predominately with a low amplitude population signal, whereas those elicited more frequently at high input gain will, on average, coincide more often with a high amplitude population signal. Consequently, the RMS amplitude of the population signals averaged across all trials coincident with the same pattern of a single cell varies across different patterns (Figure 4.6C).

The co-variation between single-cell and population response resembles the relation between hf-EEG RMS and spike patterns of a concurrently active cortical neurons (Figure 3.5). In order to test whether gain modulations could explain those experimental results the RMS amplitude of the simulated population response was compared with the spike-pattern-specific hf-EEG RMS calculated from experimental data. We found that the amplitudes of experimental hf-EEG RMS and modelled population RMS were strongly correlated (Pearson's $r = 0.99$, Figure 4.6D).

Overall, we found a positive correlation coefficient in 12 of 16 cells that produced at least 3 different patterns. This fraction is significantly above the chance level expected from uncorrelated quantities (two-tailed binomial test, $p<0.05$).

4.3. Conclusions

In this report a simple phenomenological model of high-frequency bursting in the cortex was introduced. The goal of the modelling was not to describe the specific biophysical mechanisms which underlie the phenomenon, but rather to develop a minimal model that could reproduce statistics of the experimental spike trains.

Role of synaptic inputs and refractory period in spike pattern generation

Although the model is based on two simple and biologically plausible assumptions, the statistics of simulated spike trains agree well with the experimental data. We conclude that such good correspondence supports the hypothesis that the synaptic inputs and refractoriness are enough to explain the phenomenon of bursting in the somatosensory cortex. In line with the argument, similar models were also found to describe well the history-dependence of synaptic efficacy (Sen et al., 1996).

In contrast to intrinsic bursting mechanisms (Krahe and Gabbiani, 2004; Brumberg et al., 2000), the mechanism we propose does not depend on the presence of specialised ionic currents, but their contribution can not be excluded. Consequently, the phenomenon may be classified as "forced bursting", that is fast firing triggered and sustained by an intense synaptic input.

One of the successful predictions of the model is the distribution of the firing patterns that matches experimental data. The distribution was not reproduced by the inhomogeneous Poisson model without refractoriness demonstrating that the first-order spike statistics, that is correlations between pairs of spikes, are crucial for spike patterns' generation. It is well-known that such correlations can increase the regularity of spike trains, especially unde r high input regimes (Gabbiani and Koch, 1999; Berry and Meister, 1998).

Contribution of second-order spike correlations to neuronal responses

The presented model assumes that there are no higher-order correlations involving triplets of spikes. We could test this assumption by calculating serial correlations (Farkhooi et al., 2009) between consecutive inter-spike intervals in the experimental data and comparing them to those calculated from simulated responses. In the majority of cells (8 of 14 cells for which the estimation was possible) we did not find significant deviation of the serial correlation from the value obtained from the model showing that higher-order correlations did not play an important role in the spike response generation. However, in a subset of cells (6 cells) such correlations were found to contribute significantly to the recorded spike responses. This finding is consistent with some estimates of serial correlations in spontaneous neuronal activity generated by cortical neurons (Nawrot et al., 2007). These correlations could reflect neuronal adaptation of firing frequency to input strength (Benda and Herz, 2003), short-term synaptic plasticity (Tsodyks and Markram, 1997), or bursting mechanisms (Szucs et al., 2003). Including these phenomena in the present model might further

improve its performance and shed new light on their contribution to the generation of spike patterns by neurons in the somatosensory cortex.

Intrinsic and extrinsic sources of spike-pattern variability

The trial-to-trial variability of single neuron responses may result from the intrinsic stochastic phenomena and input variability. The former may arise from the random processes acting at the level of a single synapse or involved in spike initiation (Faisal et al., 2008; Allen and Stevens, 1994), while the latter is caused by uncorrelated synaptic inputs (van Vreeswijk and Sompolinsky, 1996). In fact, it has been shown that already small fluctuations in the synaptic input can considerably improve the reliability of neuronal response to repeated presentation of the same stimulus (so called, frozen noise) (Mainen and Sejnowski, 1995). If so, the synaptic variability could help to generate repeatable spike patterns that could code for the incoming stimuli or internal state (de Ruyter et al., 1997, see also Chapter 2). Moreover, the variability of neuronal responses can increase the information capacity of a neuronal population by decreasing mutual correlations (Averbeck et al., 2006) or enhancing the dynamic range of encoded stimulus intensities (Whitsel et al., 1977).

Pseudo-random variability of the neuronal responses has been also attributed to a chaotic dynamics generated within recurrent networks. Such states have been shown to occur in a deterministic network when the excitatory currents are precisely balanced by inhibitory currents, thus increasing the total input variance without changing the mean input. Interestingly enough, the detailed balance can be achieved autonomously without a need for precise regulation of the network parameters (van Vreeswijk and Sompolinsky, 1996). These findings could help to explain the random spontaneous activity observed in single cortical neurons (Koch, 1999).

Coordination of spike-pattern responses by shared inputs

In addition to the intrinsic sources, the variability in neuronal responses can be also introduced by the variability of synaptic inputs (Fellous et al., 2003; Stevens and Zador, 1998). This phenomenon was reproduced in the model by including a shared source of variability in an ensemble of model neurons. To this end, inputs to all neurons were modulated by multiplicative gains randomly selected in each trial from a binary distribution. After this modification the model correctly predicted the relation between the single-cell and population responses, even though the population signal did not enter the fitting procedure.

The crucial assumption of the population model was that the control of the neuronal responses is mediated by the magnitude of the total synaptic drive. This mechanism could reflect gating of neuronal signals through attention, expectation, sleep and waking (Fontanini and Katz, 2008). Such neuronal gating could be implemented in a realistic neural models through, for example, concurrent modulation of excitation and inhibition (Chance et al., 2002; Vogels and Abbott, 2009) or short-term synaptic depression (Rothman et al., 2009). In fact, periodic shifts between depo-

larised and hyperpolarised states observed *in vivo* and *in vitro* in cortical neurons (Shu et al., 2003; Steriade et al., 2001) have been postulated as functional markers of such modulations. Alternatively, the fluctuations in synaptic drive could reflect variable feed-forward inputs from the lower stages of sensory processing (for example, the thalamus) that can be controlled by sleep-wake cycle or attention. In this study, the gain distribution was chosen to reflect the bimodal states of cortical excitability observed in the cortex (Shu et al., 2003), but also more complex distributions could be easily incorporated.

Limitations of the model

Although the model provides an accurate description of the experimental spike trains, it has a few disadvantages. Firstly, the model is based on a quite large set of free parameters which might lead to over-fitting. Therefore, we tested whether the over-fitting could explain the good match between the simulated and experimental data. To this end, we used a validation procedure and showed that the model fitted to the training data could still explain the validation set data. We cannot, however, exclude that the over-fitting decreased the overall performance of the model. Therefore, it may be advantageous to use a class of models in which the number of degrees of freedom is under control, such as generalised linear models with spline basis functions (Kass and Ventura, 2001).

Secondly, the values of estimated parameters do not have a straightforward biophysical interpretation. We have shown that removing the effects of the refractory period diminishes the deep dips visible in the post stimulus time histogram, but the complete explanation of shape of the intensity function would require a detailed model involving the lower stages of the processing pathway. Moreover, the overshoot in the recovery function can be a sign of a deviation from the model assumption. Finally, the model of population response assumes that the observed macroscopic potentials are directly related to the spikes of underlying neurons. Although this assumption is sensible in the high-frequency range considered here (see also Section 3.1), for the low-frequency components of EEG signals the contributions of post-synaptic currents may be much more important. All of the problems should be addressed by a biophysical model of the phenomenon, which is a natural next step towards an understanding of sensory-evoked cortical bursts and high-frequency EEG signal.

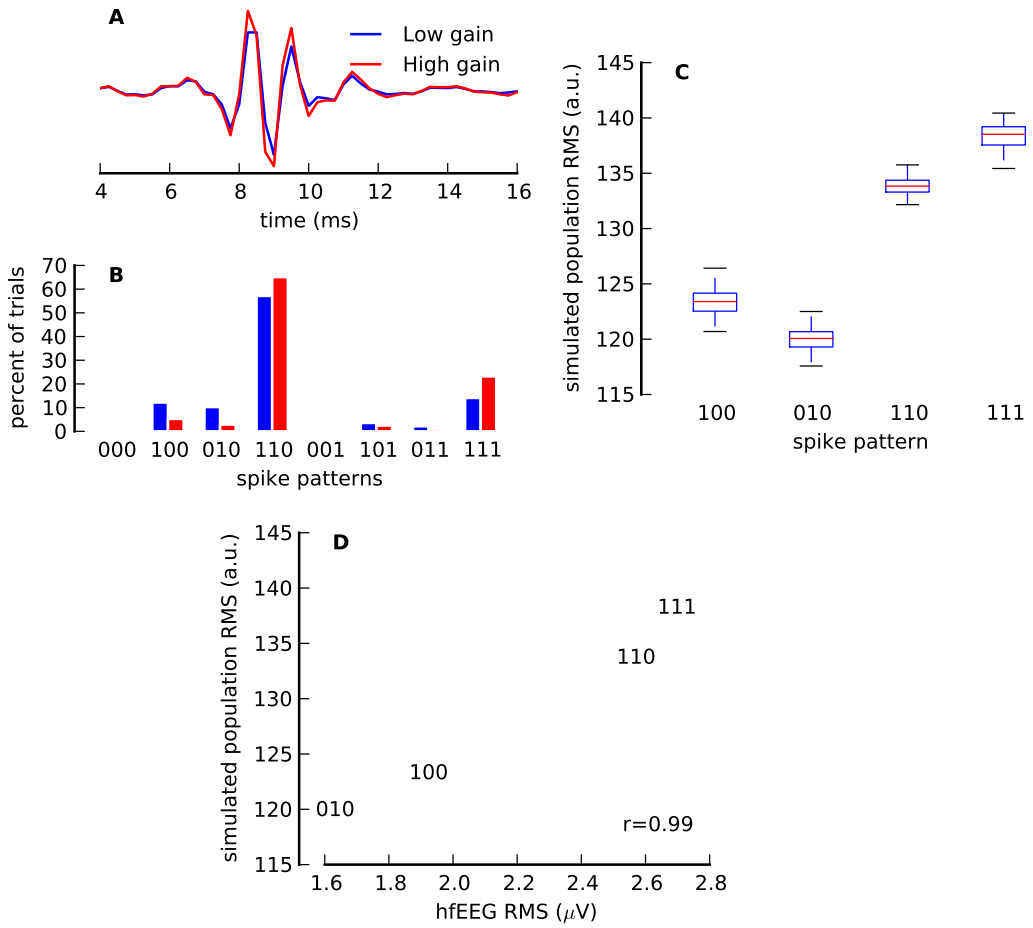

Figure 4.6.: Coordination of spike patterns patterns in the population. (**A**) Two simulations of 5000 identical units were performed. The parameters were the same as shown in Figure 4.2, but in each repetition the intensity function $q(t)$ was multiplied by a different gain factor G ($q_{\text{new}}(t) = G \times q(t)$). From the simulated spike trains the population PSTH was calculated and then high-pass filtered to obtain an estimate of population response. The amplitude of the population response was found to vary slightly with the gain: high gain ($G = 1.2$, red) is associated with a high amplitude of population response and low gain ($G = 0.8$, blue) with a low amplitude. (**B**) Similarly, distributions of spike patterns of a single cell in 1000 repetitions of the simulation with a low (blue) and high gain (red) are different. As a result, the spike patterns which occur more frequently at high/low gain will be also associated with higher/lower amplitude population responses. (**C**) The simulation was repeated over 2000 trials, the gain was set in each trial at random to either high or low value and responses of a single cell were recorded. After sorting the spike responses into spike patterns and averaging the population responses accordingly, we found that the RMS amplitude of the averaged population response was dependent on spike patterns (box plot). (**D**) The simulated population RMS amplitudes were found to correlate well with experimental hf-EEG RMS related to the same pattern (hf-EEG RMS).

5. Role of neuronal synchrony in the generation of evoked EEG/MEG responses

In Chapter 3 we made a link between the stimulus-evoked microscopic (single-cell) responses and macroscopic evoked potentials (hf-EEG). We also stipulated that the strong correspondence between those two levels is possible due to high synchrony within the neuronal ensemble. In this chapter, we further discuss the importance of synchrony in determining relations between microscopic and macroscopic phenomena. To this end, we study how synchrony may affect two popular models of macroscopic evoked responses: phase reset and added energy, and show that they describe correctly the underlying microscopic processes only if the level of synchrony is high.

This chapter is adapted from Telenczuk et al. (2010).[1]

5.1. Introduction

Evoked responses (ERs) in EEG/MEG are the primary objective real-time measures of cognitive, perceptual and motor activity in the human brain. They are usually seen as phase-locked upward or downward deflections in electric/magnetic fields best visible after averaging of many epochs.

While ERs are used frequently in basic and cognitive neuroscience, their neurophysiological generator mechanisms are still debated. ER parameters, such as amplitude, latency, and the anatomical locus of generation are commonly compared between different experimental conditions/tasks and conclusions are drawn without referring to the exact mechanisms by which ERs are generated. However, such an approach allows only for a correlative appreciation of underlying neuronal activities without insight into how information is actually processed in the brain and what possible differences in ERs might indicate.

Three basic generic models of ER generation have been proposed so far. (1) In the added-energy model stimuli produce ERs that are superimposed on the ongoing neuronal activity; the latter is considered to be noise and typically is averaged out (Dawson, 1950; Shah et al., 2004; Mäkinen et al., 2005; Mazaheri and Jensen, 2006).

[1] This work is a result of a collaboration with several researchers. Bartosz Telenczuk and Vadim Nikulin (equal contributions) conceived the project and wrote the initial version of the manuscript. Bartosz Telenczuk performed simulations and analysis described below. Gabriel Curio offered important insights and provided feedback on the manuscript.

The model implies that a phase-locked neuronal activation, such as postsynaptic potentials, is triggered by the stimulus. (2) In the phase-reset model there is no added component, but stimuli reset the phase of ongoing oscillations to a specific value such that after averaging phase-locked evoked responses become discernible (Sayers et al., 1974; Makeig et al., 2002; Fell et al., 2004; Hanslmayr et al., 2006). (3) In the baseline-shift model ERs are produced through the amplitude modulation of ongoing oscillations which do not have zero mean (Nikulin et al., 2007; Mazaheri and Jensen, 2008).

Here, we focus primarily on the first two models, i.e., added-energy and phase-reset. For the last thirty years these two mechanisms have been scrutinized in explaining the generation of visual (Makeig et al., 2002; Hanslmayr et al., 2006; Mazaheri and Jensen, 2006; Becker et al., 2008), auditory (Sayers et al., 1974; Mäkinen et al., 2005; Klimesch et al., 2006) or somatosensory ERs (Valencia et al., 2006), and a number of criteria have been advanced in order to distinguish between these two scenarios.

In parallel, the concept of phase reset was studied at the level of single neurons to describe their responses to injection of brief current pulses (Guttman et al., 1980; Reyes and Fetz, 1993). While the main phenomenon is the same – the stimulation modifies the phases of ongoing oscillations without affecting their amplitude – there is a significant difference in the spatial scales at which the phase reset occurs. In the EEG/MEG literature the phase reset model concerns commonly the observed phase of ensemble activity (macroscopic phase reset) while in cellular neurophysiology it relates either to spike timing of a single cell or the phase of its membrane potential (microscopic phase reset).

The main objective of this chapter is to clarify some common misconceptions originating in the ER research due to varying definitions of the spatial scale at which the phase reset occurs. We first show theoretically that an ER generation through either the microscopic added-energy or phase-reset mechanisms cannot be, in principle, differentiated on the basis of macroscopic EEG/MEG recordings alone. Next, we consider specific criteria regularly used for proving one or another mechanism and demonstrate that they provide only ambiguous results regarding microscopic processes as they are based on a specific manifestation of neuronal interactions (specifically, coupling strength in an ensemble of responsive cellular units), which are not accessible readily to non-invasive EEG/MEG techniques. Finally, we study how synchrony between neuronal elements, which is mediated, for example, by mutual interactions, affects the macroscopic properties of evoked responses and subsequently show that both the phase-reset and added-energy ER models can be unified within one framework.

Based on these results we conclude that without knowledge of the extent/strength of synchronization between microscopic neuronal oscillators the added-energy and phase-reset mechanisms of evoked response generation can not be reliably distinguished. Since the spatial synchronization is a microscopic ensemble property that cannot be assessed with state-of-the-art EEG/MEG, these techniques might not aid to disentangle the mechanisms of ER generation.

5.2. Methods

5.2.1. Model of microscopic neural sources

Microscopic neural elements are modeled by a population of N simplified phase oscillators with the following phase dynamics (Tass, 2005):

$$\frac{d\Psi_j}{dt} = \omega - \frac{K}{N}\sum_{k=1}^{N}\sin(\Psi_j - \Psi_k) + X(t)\sin(\Psi_j) + \gamma_{\text{indep}}F_j(t) + \gamma_{\text{common}}G(t), \quad (5.1)$$

where j is the index of an oscillator. The phase of each oscillator advances linearly with the angular eigenfrequency ω. The individual oscillators are pairwise coupled; the interaction is described by the coupling coefficient K multiplied by a phase-resetting curve (PRC) (Pavlidis, 1974). The PRC is a periodic function of phase, thus it can be represented in terms of Fourier series. Here, we choose the first non-constant term of the series, which is already sufficient to synchronize the population of oscillators (Kuramoto, 1984; Strogatz, 2000; Tass, 2005). Other shapes of PRC and their effects on results are addressed in the Discussion section. The external stimulus $X(t)$ applied by the experimenter is modeled by a pulse of intensity I which is switched on at a time t_{onset} and after a stimulation period T is switched off again, so that:

$$X(t) = \begin{cases} I & \text{if } t_{\text{onset}} \le t \le t_{\text{onset}} + T\,, \\ 0 & \text{otherwise.} \end{cases} \quad (5.2)$$

Each oscillator's phase can be advanced or delayed due to the external stimulation depending on its value at the time of stimulus' arrival. The stimulus-induced phase shift is assumed to be produced by synaptic elements with dynamics similar to those involved in mutual coupling and therefore is described by the same PRC curve as defined above, i.e., it is proportional to the sine of the phase at stimulation onset (Tass, 2007) (Figure 5.1).

In addition, the oscillators are driven by white noise sources $F_j(t)$ and $G(t)$ with standard deviations γ_{indep} and γ_{common}, respectively. Intrinsic noise sources $F_j(t)$ are independent between oscillators, whereas $G(t)$ represents random inputs common for the whole population.

5.2.2. Model of macroscopic activity

At the microscopic level the model describes only the evolution of phases and the oscillations are assumed to have unit amplitude. This is consistent with theoretical findings where microscopic systems with periodic dynamics, such as an ensemble of periodically firing neurons with weak interactions, can be uniquely described by their phases (Kuramoto, 1984; Brown et al., 2004; Gutkin et al., 2005). However, an electric or magnetic field measured far from such ensemble represents a superposition

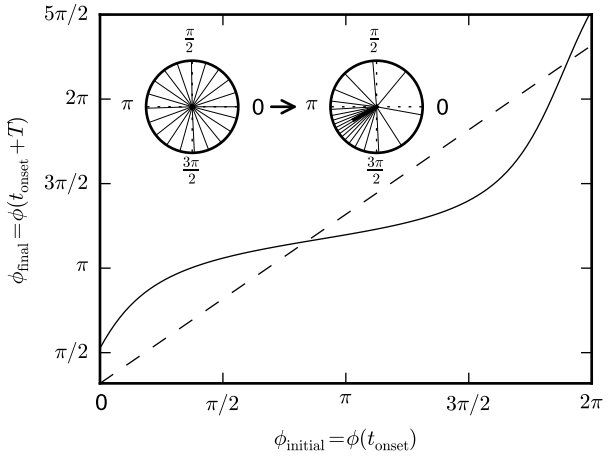

Figure 5.1.: The effect of an external stimulus on the phase of a single neuronal oscillator. The phase of the oscillator after stimulation (ϕ_{inital}) is dependent on its phase before stimulus onset (ϕ_{final}). The mapping between initial and final phases of the forced oscillator (stimulus intensity I=1.5, solid line) compared to a freely advancing oscillator (stimulus intensity I=0, diagonal dashed line) shows periods of phase advance and delay. The crossing point between both lines lying between $\pi/2$ and π corresponds to an attractor, which draws all of the phases in the course of the stimulation. Inset: A sample evolution of a population of N=20 oscillators whose phases are initially uniformly distributed (thin lines): after the stimulation the phases are concentrated around the fixed point, which results in an increased ensemble amplitude (thick line). Model parameters: γ_{indep}=0, γ_m*indep*=0, T=1, ω=1, K=0.

of fields generated by many individual elements/oscillators (Malmivuo and Plonsey, 1995; Nunez and Srinivasan, 2005). We calculate the macroscopic activity of the whole population as a circular sum (Winfree, 1980):

$$Z(t) = \sum_{k=1}^{N} \left[\cos(\Psi_k) + i\sin(\Psi_k)\right] + \gamma_{\text{meas}}\eta(t) = \sum_{k=1}^{N} \exp\left[i\Psi_k(t)\right] + \gamma_{\text{meas}}\eta(t), \quad (5.3)$$

where i is the imaginary unit, $\eta(t)$ is a Gaussian white noise modeling additive measurement errors due to environment and amplifier noise, and γ_{meas} is the standard deviation of the measurement noise.

In the whole ensemble the contributions of individual oscillators can sum constructively or destructively depending on their relative phases. The cancellation of incoherent oscillations or, respectively, the enhancement of coherent ones will result in an amplitude modulation of the net activity. The macroscopic amplitude dynamics are described by the ensemble amplitude $R(t) = |Z(t)|$, whereas ensemble phase $\varphi(t) = \arg(Z(t))$ corresponds to the ensemble phase dynamics.

5.2.3. Quantitative measures of evoked responses

We simulate M trials by calculating numerical solutions to Equation (5.1) with the same stimulus $X(t)$ but each time re-initialising the phases with random numbers drawn from a uniform distribution in the interval [-π, π]. In each run of the simulation the complex amplitude is calculated from Equation (5.3), where index $l = 1, 2, \ldots, M$ enumerates the trials. From these simulation results we calculate the average evoked response ($\mathrm{ER}_{\mathrm{avg}}$):

$$\mathrm{ER}_{\mathrm{avg}}(t) = \frac{1}{M} \sum_{l=1}^{M} \mathrm{Re}\left(Z^{(l)}(t)\right) \tag{5.4}$$

its envelope ($\mathrm{ER}_{\mathrm{env}}$):

$$\mathrm{ER}_{\mathrm{env}}(t) = \left| \frac{1}{M} \sum_{l=1}^{M} Z^{(l)}(t) \right|, \tag{5.5}$$

phase-locking index (PLI) (Tallon-Baudry et al., 1996):

$$\mathrm{PLI}(t) = \left| \frac{1}{M} \sum_{l=1}^{M} \exp\left[i\varphi^{(l)}(t)\right] \right|, \tag{5.6}$$

and the average of single-trial amplitude envelopes:

$$\mathrm{ST}_{\mathrm{env}}(t) = \frac{1}{M} \sum_{l=1}^{M} R^{(l)}(t), \tag{5.7}$$

where $\varphi^{(l)}(t) = \arg(Z^{(l)}(t))$ and $R^{(l)}(t) = \left|Z^{(l)}(t)\right|$ are the ensemble phase and amplitude in the simulation trial l.

5.2.4. Comparison to baseline

In order to estimate the change in the $\mathrm{ER}_{\mathrm{avg}}$, $\mathrm{ER}_{\mathrm{env}}$, PLI and $\mathrm{ST}_{\mathrm{env}}$ induced by the stimulation, we compare the measures to the corresponding values derived from a stimulus-free baseline. The baseline is calculated by running the simulation with the same initial conditions and model parameters but with the stimulus $X(t)$ set to 0 for all t. As a result, the simulation is run twice: with stimulation (target) and without stimulation (baseline); in both runs the initial conditions and the random number generator are reset. Next, we calculate the above-defined measures for the baseline and target trials, separately. Finally, the results obtained from the baseline simulation are subtracted from the target measures and the difference is averaged within the window defined by the stimulus duration ($t_{\mathrm{onset}} \leq t \leq t_{\mathrm{onset}} + T$).

5.3. Results

Phase reorganization at microscopic level may mimic both, phase-reset and added-energy mechanisms of macroscopic ER generation: an overview.

Prior to a detailed quantitative analysis, we introduce the key findings of the study with a simplified illustration. It is generally accepted that the amplitude of ongoing ensemble activity depends both on the synchrony among the microscopic elements and the number of elements being active (Nunez and Srinivasan, 2005). Thus, any increase of the ensemble activity may be caused by a stronger coherence and/or by the recruitment of additional synchronous units. To scrutinize this point we consider

Figure 5.3.: Schematic illustration of ongoing neuronal activity and evoked responses generated by means of recruitment of additional oscillators (top panel, I), microscopic phase reset in an asynchronous population (middle panel, II) and in a synchronous population (bottom panel, III). Neuronal recruitment: (**Ia**) Schematic representation of a small sub-population of continuously oscillating neuronal sources (ongoing sources, red cells) and sources which are silent before the onset of the stimulus (transient sources, blue cells). The phases of ongoing sources are random (filling color reflects the instantaneous phase of the oscillation) corresponding to an uniform distribution on a unit circle (polar plot: the angle of each vector encodes the phase of oscillation in a single source, the colored background depicts the mapping of phases to the cells' color shading). (**Ib**) Oscillations produced by ongoing (red lines) and transient (blue lines) sources prior to the stimulation. Before the stimulation no significant ensemble macroscopic activity is observed (thick black line, single trial, not in scale with microscopic activity). (**Ic**) An external stimulus (dashed line denotes stimulus onset) activates the transient sources which produce coherent oscillations that are visible in the ensemble activity (thick black line). (**Id**) Schematic representation of the microscopic sources in the post-stimulus period (t=20, for the symbol description see (Ia)). The responses to the stimulation are associated with activation of the additional pool of neurons (blue cells) with a narrow distribution of phases (polar plot, blue vectors). Microscopic phase-reset in an asynchronous population (**IIa-d**): All labels and symbols in this and following panels are consistent with panel (I). Although pre-stimulus activity (IIa,b) and the macroscopic response (IIc, thick black line) are identical to the neuronal recruitment scenario, the effects of the stimulation are essentially different: here, the transient sources remain silent (IIc, blue lines), but instead the ongoing sources become coherent (IIc, red lines; IId, red vectors in the polar plot) thus summing up constructively to produce a visible macroscopic response. Microscopic phase-reset in a synchronised population (**IIIa-d**): The mechanisms of stimulus response are identical to scenario (II), but here the ongoing sources are spontaneously synchronized prior to the stimulation (IIIa). The subsequent stimulation results neither in further increase of the synchrony (compare IIIa and IIId) nor in the consequent change of the amplitude of macroscopic oscillations (compare IIIb with IIIc, thick black line). Nevertheless, the post-stimulus macroscopic oscillation is aligned with the stimulus onset independent of its initial phase (note the phase reset at stimulus onset). In all panels, for simplicity, we do not show the slow decay of macroscopic amplitude due to the return of transient sources back to their quiescent state (I) or desynchronisation of ongoing sources (II and III).

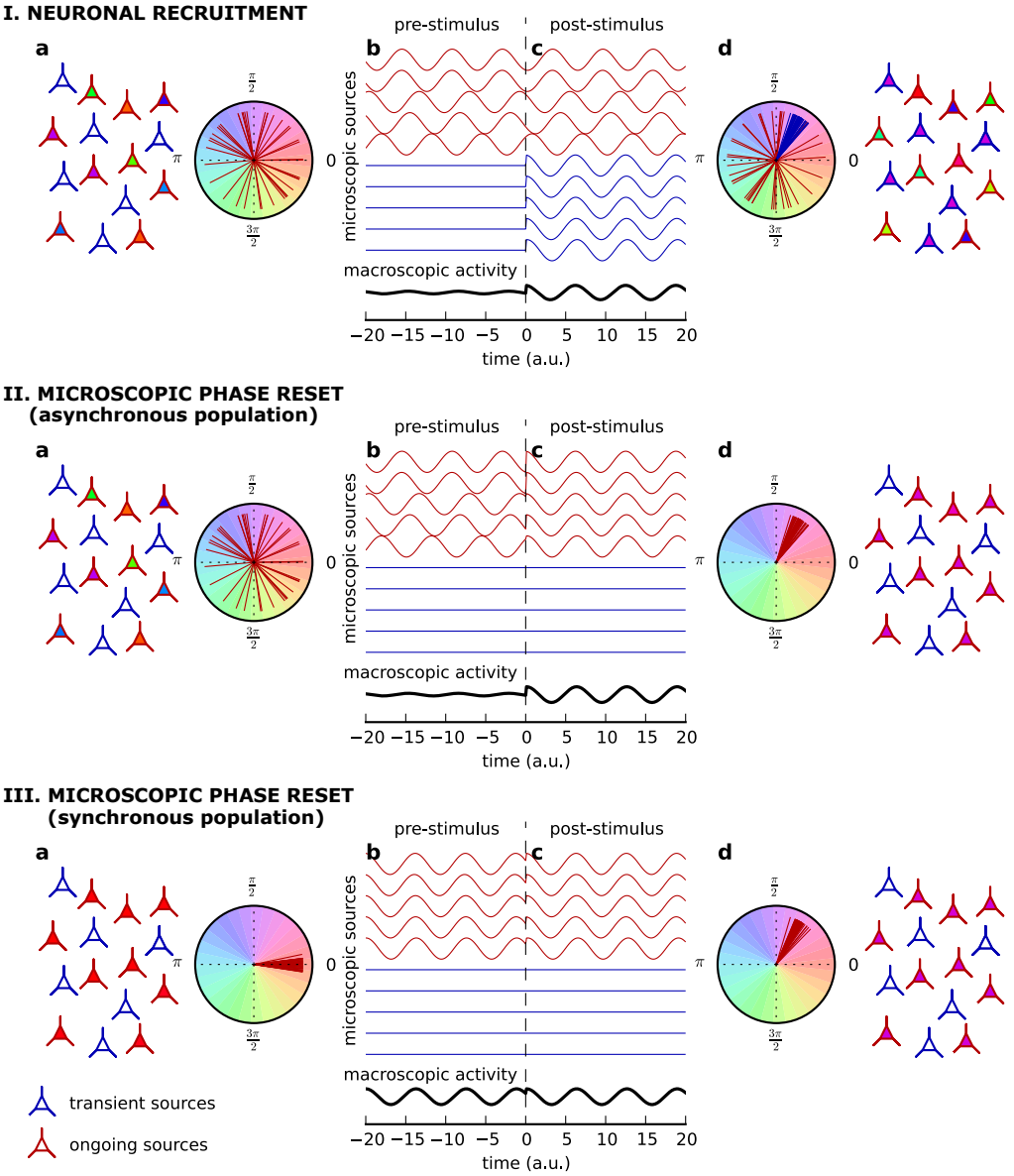
I. NEURONAL RECRUITMENT
II. MICROSCOPIC PHASE RESET
(asynchronous population)
III. MICROSCOPIC PHASE RESET
(synchronous population)
a
b
c
d
pre-stimulus
post-stimulus
microscopic sources
macroscopic activity
time (a.u.)
transient sources
ongoing sources

the case of a group of simplified neural sources. If the sources are not interacting their activities will be incoherent (Figure 5.3, Ia/IIa). Since neuronal tissue acts as a volume conductor the fields generated by individual neural sources sum up linearly resulting in cancellation of the incoherent activity and enhancement of the coherent one. Therefore, uncoupled sources (coupling coefficient K=0) while being active would not produce observable macroscopic potentials/fields measured with EEG/MEG (Figure 5.3, Ib/IIb).

Incoming stimuli may increase the amplitude of the macroscopic potentials/fields by modifying the synchrony or number of active elements. According to the added-energy model of ER generation, the response is produced by additional neural activity induced by the stimulus. Mechanistically, this corresponds to the recruitment of a previously inactive set of neurons without interference with the spontaneously active population. In this scenario, schematically represented in Figure 5.3 (I), the measured macroscopic EEG/MEG response reflects activity of the neurons that are recruited with a fixed phase to the stimulus processing (Figure 5.3, Ic,d). The stimulus-driven activity of the otherwise quiescent neurons results in an increase of the signal power, which is considered a hallmark of ERs generated by the added-energy model.

Critically, however, a similar increase in power can also be produced by the reorganization of the incoherent ongoing activity present prior to the stimulation – a scenario essentially different from the recruitment model considered above. In this case the external stimulus drives oscillation phases towards a specific value (it "resets" the phases) thus rendering them more coherent. Since at the microscopic level multiple oscillators are simultaneously active, the phase of each of them is modified accordingly. As a result of this mechanism, called microscopic phase reset, the microscopic oscillations become more coherent and they sum up constructively generating visible macroscopic (e.g., EEG/MEG) oscillations (Figure 5.3, IIc-d). In both mechanisms, i.e., in the recruitment of inactive neurons as well as in the microscopic phase reset of ongoing activity, the macroscopic responses to a single presentation of the stimulus are identical: there are no oscillations in the pre-stimulus period (Figure 5.3, Ib and IIb, black line), but there are stimulus-locked oscillations in the post-stimulus period (Figure 5.3, Ic and IIc, black line).

Let us now consider a situation in which the microscopic sources are coupled and thus spontaneously synchronized prior to the stimulus (Figure 5.3, IIIa-b). In this case, the external stimulation can not increase the synchrony further and, consequently, the microscopic phase reset will not affect the amplitude of macroscopic oscillations (Figure 5.3, IIIb-c). Although the amplitude is not affected, the phases of microscopic and consequently macroscopic oscillations are aligned to the stimulus onset (Figure 5.3, IIIc-d). The resulting post-stimulus activity is identical to the one observed in the previous two scenarios, but the pre-stimulus period contains large ongoing oscillations absent in the other scenarios. Such a response is consistent with the macroscopic phase-reset model as discussed in the EEG/MEG literature.

In the following, we construct an ER model based on the microscopic phase-reset phenomenon and provide a detailed quantitative analysis of the obtained responses.

Standard macroscopic ER measures might confuse microscopic phase reset with recruitment model.

In order to study the effect of microscopic phase-reset on macroscopic ER quantitatively, we simulated an ensemble of uncoupled noisy phase oscillators (coupling coefficient K=0, see Methods – Section 5.2.1) each of which represents a local neural unit. The initial phases are uniformly distributed so that at the beginning of the simulation the oscillations are asynchronous. However, the application of an external stimulus common to all oscillators changes the phase distribution in a specific manner. The effect of such stimulation on any single oscillator is phase-dependent: a stimulus arriving at the end of the oscillation period delays the oscillations while a stimulus arriving at the beginning of the period advances them. In effect, after the stimulation the distribution of phases over the ensemble tends to be concentrated around a preferred mean phase (Figure 5.1). The situation is similar to the scenario presented in Figure 5.3 (II), where the hard "reset" of the phase was replaced by a more realistic phase shift.

We repeated the simulation procedure (M=100; each run with different initial phases) to obtain a set of independent trials/epochs. Based on these simulation trials we calculated four indices routinely used to differentiate between mechanisms of evoked response generation: the average evoked response ($\mathrm{ER}_{\mathrm{avg}}$), its amplitude envelope ($\mathrm{ER}_{\mathrm{env}}$), the phase locking index (PLI) and the averaged single-trial amplitude envelope ($\mathrm{ST}_{\mathrm{env}}$, see Methods – Section 5.2.3) (Sayers et al., 1974; Tallon-Baudry et al., 1996; Makeig et al., 2002; Jansen et al., 2003; Valencia et al., 2006).

Stimulus-locked averaging of the macroscopic simulation trials (Figure 5.4a) exhibits a significant increase of activity (Figure 5.4b) analogous to ERs recorded with EEG/MEG. In order to elucidate the mechanism of ER generation we compared the oscillatory power of single-trial macroscopic signals following the stimulus to the baseline condition without stimulation (see Methods – Section 5.2.4). Estimating an instantaneous power modulation in experimental data involves applying rectification/squaring of band-pass filtered recordings (based on Hilbert or wavelet transform) prior to trial-averaging which avoids cancellation of phases variable over trials (Le Van Quyen et al., 2001). Accordingly, the simulated macroscopic responses were first rectified using an analytical calculation of the amplitude envelope (see Methods – Section 5.2.3) and subsequently trial-averaged. The resulting average single-trial envelope $\mathrm{ST}_{\mathrm{env}}$ showed a prominent increase following stimulus onset (Figure 5.4c). Similarly, the prominent trial-averaged ER ($\mathrm{ER}_{\mathrm{avg}}$, Figure 5.4b) has an amplitude envelope ($\mathrm{ER}_{\mathrm{env}}$, Figure 5.4e) which closely followed the single-trial power modulation. This presence of single-trial power increase accountable for trial-averaged ER is in agreement with the predictions of the added-energy mechanism of ER generation. Crucially, however, the microscopic mechanism underlying the simulated data is a pure phase reset where neither amplitude nor the number of active oscillators has been changed. The same ambiguity is inherent also to other often-employed measures, such as phase-locking index (PLI, see Methods – Section 5.2.3): When applied to the simulated data PLI revealed strong and significant coherence between

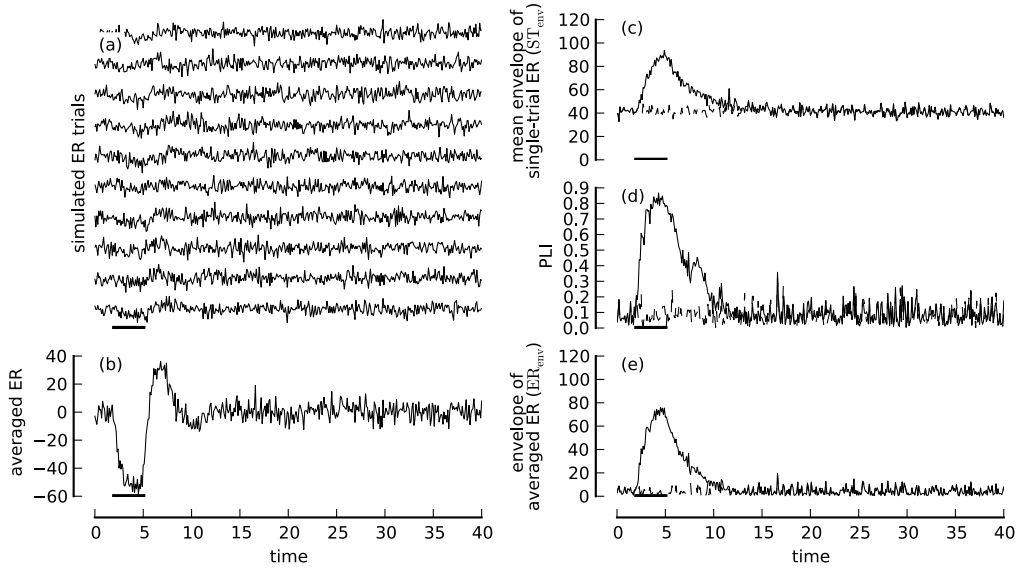

Figure 5.4.: Macroscopic evoked responses in an uncoupled population. (**a**) Ten sample simulated single trials of evoked responses (ERs). The horizontal bar in this and the following panels depicts the stimulus onset and duration. (**b**) Trial-average of M=100 simulated trials ($\mathrm{ER}_{\mathrm{avg}}$): a prominent response locked to the stimulus onset is visible. (**c**) Average of amplitude envelopes calculated from single-trial ERs ($\mathrm{ST}_{\mathrm{env}}$, bold line) and from non-stimulated baseline oscillations (calculated by setting the stimulus intensity to I=0, dashed line): the amplitude of single-trial ERs increases rapidly shortly after the stimulus presentation. The positive shift of the baseline corresponds to the amplitude of measurement noise ($G(t)$) superimposed on single EEG/MEG trials. (**d**) Cross-trial coherency of single-trial ERs phases (PLI, bold line) and baseline oscillations (dashed line): Rapid increase of PLI heralds the appearance of stimulus-locked macroscopic oscillations. (**e**) Amplitude envelope of the evoked response shown in (b) ($\mathrm{ER}_{\mathrm{env}}$): The magnitude and the time course are similar to the envelope of single-trial responses (compare with (c)) in agreement with the notion that the macroscopic ER reflects stimulus-induced single-trial ensemble oscillations. Parameters: N=100, M=100, γ_{indep}=0.63, γ_{indep}=0.63, γ_{meas}=50, t_{onset}=2, T=3, I=1.5, K=0, ω=1

the simulation trials shortly after the stimulus onset (Figure 5.4d). Naturally, high coherence is expected in all mechanisms of ER generation, because only those components that are locked to the stimulus onset will survive trial averaging and thus contribute to the ER (Mäkinen et al., 2005).

It is important to emphasize that the energy increase measured in macroscopic EEG/MEG signals owing to microscopic phase reset is not specific to model details. On the contrary, it can be shown theoretically that macroscopic signals can be represented equivalently in terms of microscopic processes involving either phase or amplitude dynamics (see Appendix B). This ambiguity can not be resolved unless the microscopic phase and amplitude distributions are known or can be experimentally measured.

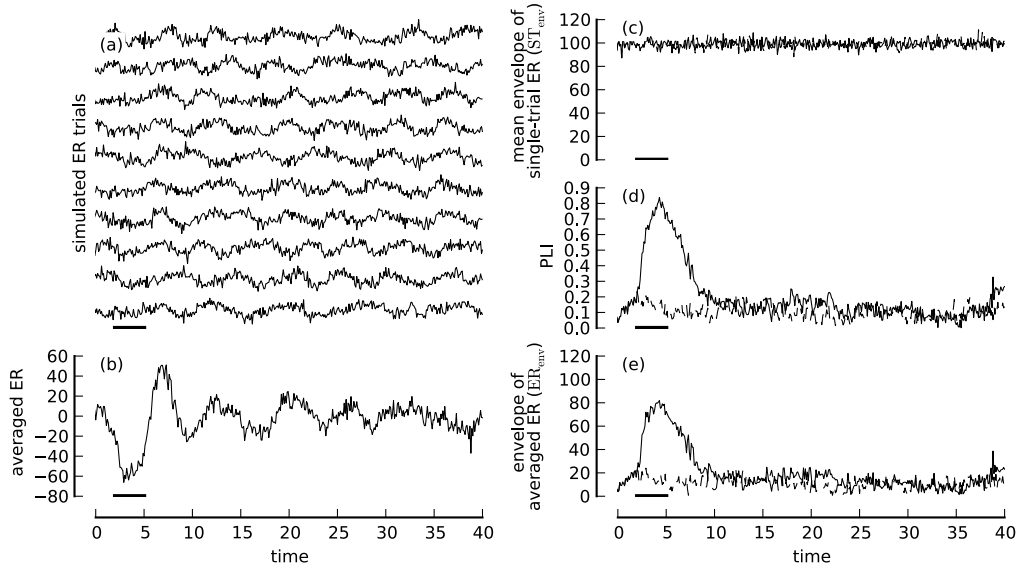

Figure 5.5.: Macroscopic evoked responses in a population of coupled oscillators. Microscopic oscillators synchronize spontaneously due to mutual interactions. For the legend to the panels see caption to Figure 5.4. (**a**) Synchrony at microscopic level leads to generation of visible macroscopic oscillations in single trials. (**b**) Trial-averaging reveals that in post-stimulus period the oscillations are locked to the stimulus-onset, producing prominent ER. (**c**) In contrast to the phase of on-going oscillation, the amplitude is not affected by the stimulus, but it stays at a constant and high level. (**d**) Since the amplitude envelope does not change, the ER can be produced solely by increasing cross-trial coherency as evidenced by PLI. (**e**) The mismatch between amplitude envelopes in single trials (c) and the average (e) suggests the contribution of a phase-reset mechanism to ER generation. Parameters as defined in caption of Figure 5.4, but with K=1.5.

The degree of synchrony across the microscopic sources can bias inferences about the mechanism of macroscopic ERs.

In order to investigate how different levels of neuronal synchrony affect a post-stimulus amplitude increase, we simulated an ensemble of coupled phase oscillators. The single oscillators resemble those described above, but here all oscillators are globally coupled between each other (coupling coefficient K=1.5, see Methods – Section 5.2.1). This coupling enables them to synchronize their activity spontaneously thereby making the phases more clustered. In contrast to the uncoupled ensemble studied above, the pre-stimulus activity in the coupled model does not cancel out upon summing over the whole ensemble and, consequently, it produces ongoing (pre-stimulus) macroscopic oscillations (Figure 5.5a). The external stimulation has no or little effect on the synchrony within the coupled ensemble and consequently the amplitude of the single-trial macroscopic oscillations remains unchanged at a level higher than in the uncoupled case (ST_{env}, cf. Figure 5.4c, uncoupled, vs. 5.5c, coupled).

Interestingly, although there is no single-trial power increase induced by the stimulation, a prominent ER locked to the stimulus is observed after averaging (Figure 5.5b). The reason is that the instantaneous intra-ensemble synchrony does not imply cross-trial coherence in ongoing (pre-stimulus) oscillations. On the contrary, the ongoing activity, which is not locked to the stimulus, will largely cancel out after trial averaging. However, the external stimulation, while not affecting the (already strong) ensemble synchrony, aligns the ensemble oscillations in each trial, so that macroscopically ER peaks become visible after trial averaging. This phenomenon is reflected in the time course of PLI (Figure 5.5d): being low initially it increases strongly after stimulation onset. These post-stimulus oscillations being locked to stimulus onset survive averaging and produce a visible ER whose amplitude envelope is similar to the uncoupled case (Figure 5.5e). After the end of the stimulation, the stimulus locking will decay as a result of random inputs common to all oscillators, but the ensemble synchrony will not change owing to the strong endogenous mutual coupling.

The models discussed so far represent two opposite ends of a "synchrony" spectrum: in the uncoupled ensemble the phases of all microscopic oscillators are independent whereas in the strongly coupled ensemble they are close to identical. What happens in the intermediate range of coupling strengths? To answer this question, we simulated the model with varying coupling coefficient (K) and calculated the stimulus-induced increase of single-trial amplitudes ($\mathrm{ST}_{\mathrm{env}}$) and the amplitudes of evoked responses ($\mathrm{ER}_{\mathrm{env}}$) in relation to their respective baselines. We found that while the amplitude of ERs does not change much, there is a smooth transition from a significant amplitude increase in the low-coupling case to no single-trial increase in the high-coupling case (Figure 5.6). These findings indicate that the standard ER generation mechanisms (phase-reset and added-energy) described in the literature (Sayers et al., 1974; Arieli et al., 1996) represent the outermost instances of a continuous spectrum of "mixed" models.

The macroscopic measures obtained by simulation of microscopic phase reset mechanisms under different coupling strengths are compared with predictions of macroscopic phase reset and added-energy models in Figure 5.7. Summarizing the results presented above, the figure shows that three different microscopic scenarios are qualitatively consistent with the predictions of the macroscopic added-energy model (Figure 5.7A, gray background): neuronal recruitment at low and high neuronal coupling, and microscopic phase reset at low coupling (Figure 5.7B, gray background). Conversely, the remaining scenario of microscopic phase-reset in a highly coupled ensemble (Figure 5.7B, white background) produces responses in agreement with macroscopic phase reset (Figure 5.7A, white background).

5.4. Discussion

The above results show that one generic microscopic mechanism for evoked responses, i.e., the one which is produced by phase reset of ongoing oscillations in an ensemble

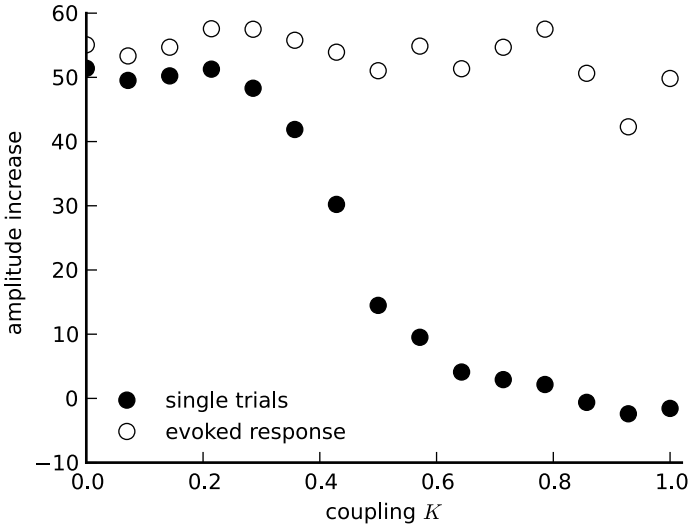

Figure 5.6.: Effect of spatial neuronal synchronization on the signal energy increase in ER. Population synchrony does not significantly influence the mean amplitude of evoked response (ER_{env}, open circles), whereas the increase of single-trial oscillatory energy (ST_{env}, closed circles) decays with the increase of a coupling parameter K. The points show the mean value of the indices in the stimulus window ($t_{onset} \leq t \leq t_{onset} + T$). In a weak-coupling case (K<0.2) averaged and single-trial ERs have similar amplitudes in agreement with the predictions for the added-energy mechanism of evoked response generation. The large discrepancy between these amplitudes in a strong coupling case (K>0.8) is usually taken as indication of a phase-reset contribution. In between these two extremes there is a continuous transition from large single-trial energy increase to complete absence of such increase suggesting mixed contributions from both mechanisms. In fact, the only responsible mechanism at the microscopic level in all cases is a phase reset of the underlying oscillators. The amplitude increase is calculated as a difference between mean amplitude in the stimulation period and the mean baseline amplitude (no stimulation) and averaged over M=100 trials. All model parameters except K which is shown on the ordinate are the same as in the caption to Figure 5.4.

of neuronal single units, can be consistent with either the macroscopic phase-reset or added-energy models of ER generation depending on the strength of spatial synchronization between the neurons. Consequently, usage of EMG/EEG recordings without exact knowledge of intra-ensemble coupling strength makes it difficult to decide which microscopic mechanisms are responsible for the generation of evoked responses.

Phase reset vs. added-energy mechanism

The most fundamental criterion, which is frequently used for differentiating between phase-reset and added-energy mechanisms of ER generation, is the presence/absence of a single-trial energy increase in the post-stimulus interval. If present, such increase is usually taken as evidence for the added-energy mechanism, where new activity is

added to ongoing neuronal oscillations (Dawson, 1950; Shah et al., 2004; Mäkinen et al., 2005). On the other hand, the absence of such energy increase is considered to be an indication for phase reset, i.e., ongoing oscillations merely undergo a phase reset while their amplitude remains unaffected (Sayers et al., 1974; Makeig et al., 2002; Fell et al., 2004). However, the previous studies considered only the temporal coherence of macroscopic oscillations across trials. When, in addition, the spatial coherence across multiple microscopic oscillators within a single trial is taken into account, an amplitude increase can be achieved easily by a (microscopic) phase reset in an ensemble of oscillating cells with a very low level of spatial synchronization. Thus, at the macroscopic level of EEG/MEG, an observed amplitude increase is consistent with both recruitment of additional cellular oscillators and microscopic phase-reset mechanisms. Consequently, this most frequently used criterion, which captures the differential essence of the two ER mechanisms, cannot be used as a reliable criterion for deciding on the genuine neuronal processes underlying the observed macroscopic ER.

Another frequently used prerequisite (Sauseng et al., 2007) or criterion (Shah et al., 2004; Becker et al., 2008) associated with phase reset is the presence of ongoing neuronal oscillations. While it is true that a phase reset is possible only in the presence of oscillations (otherwise there is nothing to reset), the present results show that oscillations at the microscopic level might not be easily observed in macroscopic EEG/MEG recordings in case of a low level of spatial synchronization in a given ensemble of oscillating neurons. Such macroscopically "masked" oscillations could lead to the conclusion that ERs are produced without the presence of ongoing oscillations (a result favoring the added-energy mechanism), which would be a premature statement if there were no information available about the strength of the spatial synchronization.

Another ambiguity for both phase-reset and added-energy mechanisms is the so-called phase concentration in the post-stimulus interval (measured, for example, by PLI). It is present for both mechanisms and while it is important for obtaining phase-locked responses, it does not allow one to differentiate between the two models.

While further secondary criteria were proposed for distinguishing between the phase-reset and added-energy mechanisms, such as a similar spatial location for the generation of oscillations and evoked responses (Barry, 2009) or sensitivity to the phase/amplitude of ongoing oscillations (Sauseng et al., 2007; Becker et al., 2008), they also can not be resolved unambiguously in favor of one or another model at the level of EEG/MEG (Sauseng et al., 2007).

The possible mechanistic connection linking a microscopic phase reset to an macroscopically apparent added-energy measured with EEG/MEG is the main topic of this chapter. While it is a direct consequence of established electrophysiological facts concerning the generation of EEG, it has not yet been rigorously studied. Although Sauseng et al. (2007) mentioned that phase resetting of a large population of neurons may result in EEG power increase, they did not provide a quantitative analysis and, specifically, did not address the question of under what conditions such a power

increase may occur, what the parameters influencing its magnitude are and how the notion of a variable spatial synchronization can reconcile within one framework the apparently contradictory findings favoring phase-reset vs. added-energy mechanisms. Here, we developed a stringent argumentation conceptually sharpening the issue and report on detailed simulations and theoretical analysis supporting the multifaceted insights.

Role of spatial synchronization

The key parameter manipulated in the model is the coupling between the neuronal sources, which affects the amount of spatial synchronization prior to the stimulus. In the low coupling regime, a stimulus-triggered simultaneous phase reset of multiple oscillators produces a post-stimulus increase in macroscopic single-trial energy. However, when the intra-ensemble coupling is increased, many of the individual sources become spontaneously synchronized and can behave almost as a single macroscopic oscillator producing spontaneous on-going EEG/MEG oscillations. The response of this oscillator to the presentation of a stimulus is consistent with the notion of phase reset as regularly used in the ER literature: the pre-stimulus macroscopic oscillations become aligned to the stimulus onset thereby increasing the post-stimulus cross-trial coherency. Only in this scenario, in which tightly-coupled neuronal oscillators are phase-reset by the stimulus, one could correctly conclude about microscopic mechanisms from their macroscopic manifestation. Notably, in practice, this situation may be difficult to discern from an added-energy mechanism because an added component may be masked by noise or by ongoing oscillations and consequently the response may be incorrectly interpreted as a phase reset (Becker et al., 2008).

Experimental estimates of coupling strength come from the measurements of the synchronization of alpha oscillations (which are most often implicated in the generation of evoked responses through a phase reset) recorded from very closely spaced electrodes. These measurements show that the spatial synchronization can be attenuated by 50% within just a few millimeters (Bullock et al., 1995). In another study in cats it was also found that the neuronal synchronization between neurons attenuated rapidly within just a few millimeters (Destexhe et al., 1999). Both results suggest that the coupling between neuronal sources is low. Clearly, in such situations, the amplitude of macroscopic EEG/MEG oscillations depends strongly on the amount of synchronization between the neurons (Naruse et al., 2010).

Baseline-shift model of ER

The third model for ER generation states that the amplitude modulation of ongoing oscillations with non-zero mean can lead to ERs (Nikulin et al., 2007, 2010; Mazaheri and Jensen, 2008) even when these oscillations are not visible at the macroscopic MEG/EEG level. This is because a low spatial synchronization between neurons can abolish macroscopic oscillations, but it would have no effect on the corresponding changes of the baseline shifts arising from the modulation of non-zero-mean oscilla-

tions (Nikulin et al., 2010). In such situation one would tend to believe that ERs are generated through an added-energy mechanism; yet, again, without knowledge of the spatial synchronization such a conclusion would be premature. In general, the formal inclusion of this third ER model would further increase the uncertainty about the mechanisms thus strengthening the main point of our conclusions.

Details of the phase oscillator model

The phase oscillator model employed in this study is a widely used approach for simulation of coupled oscillators (Schuster and Wagner, 1990; Sompolinsky et al., 1990; Hansel et al., 1993; Pikovsky et al., 2002; Seliger et al., 2002). The dynamical properties of such models and their dependence on the parameters were studied in depth both analytically and using computer simulations (Acebron et al., 2005). In particular, the conditions under which the individual oscillators synchronize their activities are well-understood (Kuramoto, 1984; Strogatz, 2000). Building on these fundamental findings, we chose here a specific model that is general enough to reproduce different regimes of neuronal dynamics affecting ER generation and that avoids the plethora of details of more complex models that could obscure the present main point.

The parameters for the model were chosen to reflect either experimental findings or theoretical work on the neuronal dynamics. Specifically, the phase-resetting curve (PRC), which quantifies the coupling between different neurons and between neurons and stimulus (Figure 5.1) can be measured experimentally and calculated analytically. The biphasic PRC employed here is qualitatively similar to the PRC obtained, for example, by an analytical reduction of a realistic axon model (Brown et al., 2004), or recorded experimentally from in vivo neurons (Tateno and Robinson, 2007). However, monophasic PRCs are also found in some in vivo and in silico neurons (Reyes and Fetz, 1993; Gutkin et al., 2005). Oscillators interacting via such monophasic PRCs, in contrast to the present simulations based on a biphasic PRC, desynchronize their activities (Hansel et al., 1995) unless a non-instantaneous response of the synapse is additionally taken into account (van Vreeswijk et al., 1994). Nevertheless, even in the asynchronous population an external stimulus in the ensemble can still lead to a concentration of their phases by simultaneously driving all oscillators and induce an accompanying increase of macroscopic energy, in analogy with the uncoupled model presented above.

Since PRCs are periodic functions of phase they can be expanded in the form of a Fourier series. Without loss of generality, we held only the first non-constant term of the expansion. Fourier modes of higher order can enrich the dynamics, for example introducing clustering (Sakaguchi et al., 1987). This intriguing phenomenon is independent of the effects described here and imposes further complications on the interpretation of macroscopic EEG/MEG signals (Tass, 2007).

In order to make the present model more realistic, we also introduced two types of phase noise to the model (see Methods – Section 5.2.1): individual noise independent for each oscillator ($F_i(t)$) and shared noise common for all oscillators ($G(t)$). The

former reflects the intrinsic noise sources within each neuron (White et al., 2000; Faisal et al., 2008), whereas the latter models unspecific "background" inputs arriving simultaneously at all oscillators (Shadlen and Newsome, 1998; Fontanini and Katz, 2008). The effect of the noise is the desynchronization of the oscillators after the stimulus is switched off, which results in the decay of the evoked response. In additional numerical simulations (not shown) we found that the amplitude of the individual noise mainly affects the decay time of ERs generated in the uncoupled population, whereas the amplitude of the shared noise shapes the decay of ERs in the coupled population. It is important to note that these are only quantitative differences without an influence on the accuracy of the main conclusions which would still hold even if one or both of the noise terms is dropped.

In our model we assume identical eigenfrequencies for all oscillators. This assumption could be easily generalized for the case where the frequencies are distributed over some range. It was shown that even in this case the phase oscillators can spontaneously synchronize their activities provided that the coupling is strong enough to overcome the variability of eigenfrequencies. In this case the oscillators will become spontaneously entrained to an ensemble oscillation with a net frequency (Kuramoto, 1984; Strogatz, 2000). Therefore, such a modification of our model, after the proper adjustment of the coupling coefficient, would not qualitatively affect our results.

Generality of the conclusions

In the discussed model, the key neuronal population property affected by the stimulus is the amount of synchronization between the neurons. This, in turn, relates to the strength of the measured electric/magnetic field, which was shown to be proportional to the number of synchronously firing neurons (Nunez and Srinivasan, 2005). In a given network the strength of spatial synchronization varies, which consequently leads to the fluctuations in the amplitude of ongoing oscillations.

For the purposes of the present study it is not important how exactly the synchronization between neurons is achieved. It can be based on direct excitatory connections between neurons or on the involvement of inhibitory neurons (Bibbig et al., 2002; Naruse et al., 2010). For the generation of EEG/MEG signals it is only important that a large number of neurons become synchronous and thus macroscopically measurable signals can be produced.

More detailed models that incorporate anatomical and electrophysiological data about a given system may help to elucidate the contributions of population synchrony and number of active oscillators to ERs generated in this specific system. For example, a detailed mathematical modeling of the alpha rhythm in primary visual cortex indicated that visually-evoked ERs might be caused predominantly by stimulus-induced changes in coherence (phase-locking) between multiple trials (Naruse et al., 2010) in agreement with a macroscopic phase reset model. Here, we abstract from such details to expose the general problem of ambiguity between microscopic and macroscopic phase reset and its far-reaching consequences for ERs.

In order to reinforce our conclusions, we complement the study by a theoretical

analysis (Appendix B) which is not bound to any specific mechanism of synchronization. In line with the simulation results, it shows that arbitrary ERs can be described equivalently in terms of amplitude or phase dynamics of oscillators involved in the generation of macroscopic EEG/MEG signals.

Reliable demonstration of microscopic phase reset in the central nervous system

An unambiguous demonstration of microscopic phase-reset has been provided in the work of (Reyes and Fetz, 1993) who studied phase-dependent effects of brief current pulses on the length of interspike intervals, while (Kazantsev et al., 2004) showed that oscillations of the membrane potential can also be reset by a current input. Similar phenomena have been observed across a variety of different neural system including the visual cortex (Stiefel et al., 2008), early somatosensory cortex (Tateno and Robinson, 2007) and hippocampus (Lengyel et al., 2005). Although such a level of description might not be viable in human neurophysiology, recording techniques, which are based on a very closely spaced set of recording electrodes, might be very useful when assessing the amount of spatial synchronization and thus more reliably drawing conclusions about the mechanisms of evoked responses (Ritter and Becker, 2009).

On the importance of differentiation between added-energy and phase-reset models

Evoked responses are among the most frequently used objective measures of human brain activity and are utilized for a description of different perceptual, motor and cognitive processes. Changes in evoked responses do show that neuronal processing is different between the conditions. Yet, if one is interested in knowing what these changes reflect, then the knowledge of how evoked responses are generated is of prime importance.

In the case of a phase-reset mechanism, changes in evoked responses might indicate adaptive fine-tuning of neuronal oscillations for current processing demands (Hanslmayr et al., 2006; Bonte et al., 2009). On the other hand, ER changes consistent with added-energy mechanism would reflect rather either the number of neurons being recruited for the current processing demands or their mean activity (Jones et al., 2007).

Since the macroscopic signals reflect summed activity of microscopic sources, the macroscopic phase dynamics is necessarily only a reflection of phase reorganization processes occurring in the underlying neuronal population. Therefore, macroscopic phase reset is a secondary phenomenon and thus it is mechanistically realized mainly through phase reset of microscopic oscillations. Pragmatically, one can refrain from the question of mechanisms and limit oneself rather to the analysis of correlations between macroscopic oscillations' phase or amplitude and some cognitive process or

behavior (Dustman and Beck, 1965; Sauseng et al., 2005). Nevertheless, in any phenomenological approach the investigation of phase reset and added energy models cannot elucidate specific mechanisms behind the registered EEG responses. Were such mechanisms pursued, one should focus on how other properties with a clear microscopic interpretation, such as synchrony, cortical geometry, neuronal morphology (Lindén et al., 2010) and trans-membrane currents (Murakami et al., 2003; Jones et al., 2009) shape ERs. The theoretical analysis and computer modeling presented here provide a well-controlled framework for such investigations.

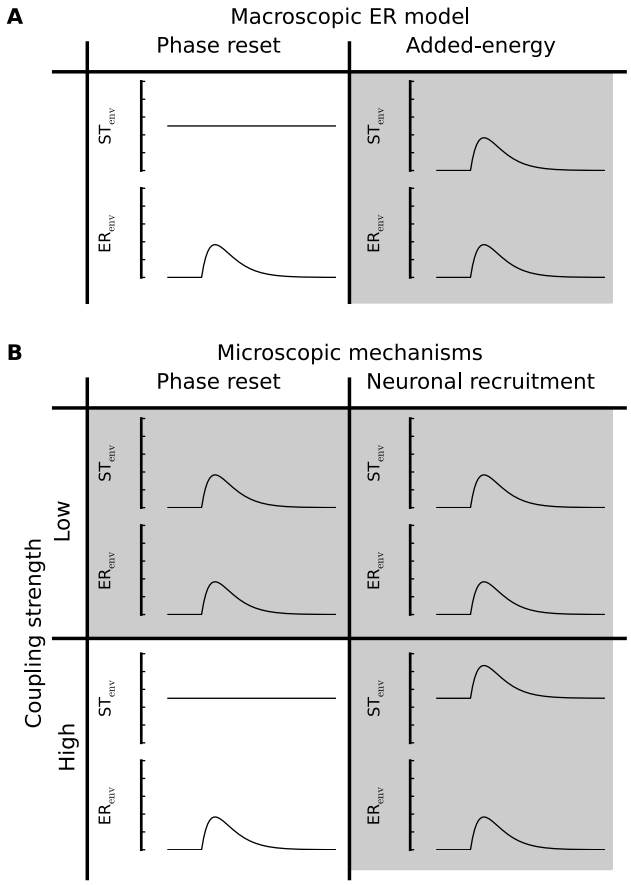

Figure 5.7.: Summary of predictions of macroscopic EEG/MEG response properties made by macroscopic ER models and their microscopic equivalents. (**A**) Schematic representation of two macroscopic EEG/MEG measures: envelope of ER (ER_{env}) and single-trial amplitude envelope (ST_{env}), as predicted by two models of ER generation. Although the average ERs produced by phase-reset and added-energy models (lower curve, ER_{env}) are similar, the added-energy model also predicts the presence of the stimulus-induced increase in the single-trial power (upper curve, ST_{env}). (**B**) The ERs produced by the microscopic equivalents of the models presented in (A). Microscopic phase reset (left column) can reproduce responses of either the added-energy model (first row) or the macroscopic phase-reset (second row) depending on the strength of neuronal coupling. For comparison, we also show ERs produced by activation of an additional neuronal population (right column, neuronal recruitment): independent of coupling the responses are consistent with the criteria of the added-energy model (the non-zero baseline at high coupling level could be accounted for by adding ongoing oscillations unaffected by the stimulus to the added-energy model responses). The gray shading marks all ER responses that are consistent with predictions of the added-energy model of ER generation.

6. Conclusions

In this thesis we were concerned with the relations between the activity of single neurons or small groups of neurons and the activity of large neuronal populations. In order to study the problem several experimental methods were compared, such as single-unit activity (Chapter 1 and 2) and epidural EEG recordings (Chapter 3). This heterogeneous dataset required the application of novel data analysis techniques many of which were developed for the purpose of this work (for example, spike pattern analysis and the metric-based autocorrelation function in Chapter 2, single-trial EEG analysis and correction for input variability in Chapter 3). The results from the analysis of experimental data were supplemented by modelling and theoretical arguments that helped to generalise the findings (Chapter 5) and test hypotheses driven by experimental observations (Chapter 4).

6.1. Crossing the scales

In Chapter 1 we emphasised the importance of comparing experimental methods and results at different spatial and temporal scales. In particular, we were interested whether the microscopic activity of single neurons can be inferred from the macroscopic activity of the whole population. We tried to identify the main questions that are critical to the problem. These questions have driven our research and we shall now summarise what was learnt from the results presented here.

How do microscopic and macroscopic scales differ? As discussed in the Introduction both microscopic and macroscopic activity reflect currents flowing through ion channels embedded in the cellular membrane. Although the physical processes behind the recorded potentials may be similar, their biological substrates depend on the dimensions of electrodes used for recordings and the distance of the recording sites from the current sources. Therefore electric potentials recorded at microscopic and macroscopic scales differ with respect to the number of contributing neurons, the spatial distribution of the recorded potentials, their frequency content and sensitivity to different neuronal processes, such as excitatory and inhibitory synaptic inputs or action potentials.

Which neuronal processes are microscopic and macroscopic activity sensitive to? Microscopic single-unit activity reflects the timing of action potentials emitted by single neurons. In addition, action potentials of cells recorded in the somatosensory cortex were found to form multiple temporal spike patterns, which potentially encode

the current state of the neuron or its synaptic inputs determined by the state of the local network in which the neuron was embedded (Chapter 2).

EEG is a macroscopic measure representing activities of large neuronal populations. It is mainly sensitive to slowly changing potentials that are coherent across large cortical areas, such as post-synaptic potentials (Chapter 1). However, high-frequency oscillations in EEG (hf-EEG), which were evoked by sensory stimulation, were tightly correlated with preferred spike timing of single cortical neurons. Mean amplitude of the oscillations co-varied significantly with single-neuron spike patterns, possibly reflecting the dynamic cortical computations (Chapter 3).

In the low-frequency range, we showed using computer simulations and analytical arguments that the amplitude of stimulus-evoked oscillations depends on the number of contributing neuronal sources and their mutual correlations (Chapter 5).

Under what conditions are the microscopic and macroscopic activities comparable? The major factor influencing the relations between microscopic and macroscopic scales is the range of signal frequencies of interest. While the low-frequency components that dominate the EEG power spectrum reflect activity from large cortical areas, the small amplitude high-frequency components are more likely to represent local neuronal activity close to electrodes (Chapter 1 and 3).

In addition, we identified the synchrony across neurons to be another factor influencing the relationship between the microscopic and macroscopic scales: at the high-synchrony level the two scales were found to be closely related while at low synchrony their relationship could not be confidently determined (Chapter 5). In Chapter 4 we analysed synchrony mediated by a common input and showed that the fluctuations of its intensity may coherently modulate the responses of large neuronal populations and thus render variations in their activity visible in EEG signals (cf. Chapter 3).

Is it possible to draw conclusions about processes happening at one of the scales from the findings about the other? Although in general it may be very difficult to establish a link between the microscopic and macroscopic scales, under specific conditions these two levels of neuronal organization may be closely related. In order to understand these complex relations it is necessary to experimentally investigate the neural systems at various scales and design computational models that can link the separate findings. Such an integrated approach will enable us, on the one hand, to understand how macroscopic activity arises from microscopic neuronal properties (see Chapter 2) and, on the other, to measure non-invasively how these properties change under different physiological and pathological conditions.

6.2. Outlook: Multiscale dynamics

The theoretical and experimental results presented in this thesis dealt with propagation of the electric activity from the microscopic sources to the macroscopic recording

electrodes. However, we did not discuss the dynamical features of the recorded signals and how they relate to neuronal function (da Silva, 2004). Computational models are essential for approaching this challenge since they allow us to study neuronal mechanisms and processes that are not directly observable (Deco et al., 2008). Models linking multiple scales may help us to understand how emergent behaviours stem from the properties of the constituting units (Robinson et al., 2005) and they can be used as forward models, which may be inverted given empirical data (Robinson et al., 2004; David et al., 2006).

Realistic neuronal networks are comprised of a large number of interconnected neurons. The underlying dynamics of such networks can be studied explicitly by a population of coupled model neurons. Although such large-scale simulations may help to reproduce a number of dynamical properties of real neural networks (Izhikevich and Edelman, 2008), they are computationally expensive and, due to high dimensionality of the models, their results are difficult to analyse and interpret. These difficulties may be overcome by means of grouping neurons into statistically similar populations and expresses their dynamics as a temporal evolution of the probability distribution of their states over the entire population (Deco et al., 2008).

In future, this and similar approaches may help to interpret the features of macroscopic EEG signals not only in terms of microscopic activity of individual neurons but also their dynamical interactions (Robinson et al., 2005; Nunez and Srinivasan, 2005). Results of such research may ultimately help us to bridge the gap between the microscopic neuronal dynamics and macroscopic brain activity.

A. Data set specifications

The following table contains a complete list of cells used in the analysis of Chapter 3 together with basic statistics characterising the cells.

Recording		Brainstem Recording	Sorting Quality		Spike Responses			
Cell ID	Subject		SNR_{spk}	IsoScore	# PSTH peaks	# patterns	# pairs	# trials
Cell 1	I	Yes	1.84	0.990	2	4	6	1084
Cell 2	I	Yes	3.02	0.998	2	3	3	1022
Cell 3	I	Yes	1.50	0.994	2	4	6	1105
Cell 4	I	Yes	1.78	0.962	4	6	15	1481
Cell 5	I	Yes	1.24	0.956	3	6	15	1279
Cell 6	I	Yes	1.38	0.961	2	4	6	1329
Cell 7	I	Yes	1.44	0.970	3	6	15	1329
Cell 8	I	Yes	1.44	0.929	3	4	6	1013
Cell 9	I	Yes	1.46	0.995	3	6	15	1013
Cell 10	I	Yes	1.46	0.955	2	4	6	1029
Cell 11	I	Yes	1.11	0.961	2	4	6	903
Cell 12	I	Yes	1.29	0.936	3	6	15	1005
Cell 13	I	Yes	1.74	0.989	2	3	3	148
Cell 14	I	Yes	1.55	0.997	3	6	15	1096
Cell 15	II	No	0.52	0.911	1	2	1	1596
Cell 16	II	Yes	1.30	0.904	2	4	6	150
Cell 17	II	No	1.58	0.934	3	8	28	956
Sum			–	–	–	80	167	–
Sum (with brainstem)			–	–	–	70	138	–
Mean/*Median*			1.51	0.961	*2*	*4*	*6*	*1029*
Std.dev.			0.48	0.030	0.7	1.5	6.7	372.0
Min			0.52	0.904	1	2	1	148
Max			3.02	0.998	4	8	28	1596

Table A.1.: Summary of the dataset used in the analysis. *Recording*: cell an subject index; *Brainstem Recording*: "Yes" indicates that another macroelectrode was injected into pyramidal tract to monitor subcortical input variations (see Methods); SNR_{spk}: spike signal-to-noise ratio (see Methods); *IsoScore*: isolation score (see Methods); *# PSTH peaks*: number of distinct peaks identified in overall PSTH histogram; *# patterns*: number of identified spike patterns; *# pairs*: number of different spike pattern pairs; *# trials*: total number of stimulation trials.

B. Ambiguity between phase and amplitude dynamics: analytical treatment

In this section we show on theoretical grounds that regardless of the exact models the same macroscopic EEG/MEG signals can be represented either in terms of microscopic amplitude or phase dynamics.

Oscillatory macroscopic EEG/MEG activity can be fully described by its amplitude $R(t)$ and phase $\phi(t)$:

$$y(t) = R(t)\cos\left[\phi(t)\right] = \Re(Z(t)), \tag{B.1}$$

where $Z(t) = R(t)\exp[i\phi(t)]$ is a complex variable fully describing the oscillations and $\Re(\cdot)$ denotes its real part.

As described in the method section, EEG and MEG signals contain only information about the total activity, so that they can be alternatively represented as a sum of individual microscopic oscillations:

$$Z(t) = \sum_{k=1}^{N} r_k(t)\exp\left[i\Psi_k(t)\right], \tag{B.2}$$

where N is the number of oscillators. Note that in addition to phase dynamics $\Psi_k(t)$ we also introduced the amplitude dynamics $r_k(t)$ of microscopic oscillators. For simplicity, the measurement noise term was dropped without loss of generality.

The reference frame for phase can be chosen arbitrary and we define it here as an angle of a vector representing the oscillation on a complex plane. Such representation, called analytical signal, can be obtained from real-valued EEG/MEG signal by means of a Hilbert transform (Bracewell, 1999). Since the observed macroscopic activity is a superposition of a large number of microscopic elements we can approximate it by an ensemble of infinitely many phase oscillators ($N \to \infty$). Consequently, we can substitute the sum in Equation (B.2) with an integral over the distribution of phases

and amplitudes:

$$Z(t) = \int_0^{2\pi} \int_0^{\infty} f(\psi, r, t) r \exp(i\psi) d\psi dr. \tag{B.3}$$

$f(\psi, r, t)$ is the joint probability density function (pdf), which must integrate to 1:

$$\int_0^{2\pi} \int_0^{\infty} f(\psi, r, t) d\psi dr = 1, \text{ for all times } t. \tag{B.4}$$

Since $f(\psi, r, t)$ is a periodic function of ψ it can be expanded in terms of Fourier series:

$$f(\psi, r, t) = \sum_{k \in \mathbb{Z}} \hat{f}(k, r, t) \exp(ik\psi), \tag{B.5}$$

where $\hat{f}(k, r, t) = \frac{1}{2\pi} \int_0^{2\pi} f(\psi, r, t) \exp(-ik\psi) d\psi$ are the Fourier series coefficients.

Since the probability density function is a real function integrating to 1 the following relations must be fulfilled for all times t:

$$\begin{aligned} \hat{f}(-k, r, t) &= \hat{f}(k, r, t)^* \\ \int_0^{\infty} \hat{f}(0, r, t) dr &= \frac{1}{2\pi} \end{aligned} \tag{B.6}$$

After substitution of the equation (B.5) into (B.3) we obtain that the ensemble variables are determined only by one Fourier mode of the pdf:

$$Z(t) = 2\pi \int_0^{\infty} \hat{f}(-1, r, t) r dr. \tag{B.7}$$

Note that in general both phase and amplitude can vary in time. However, in the phase-reset model it is assumed that the amplitude distribution remains constant whereas the phase distribution changes due to the stimulation. Conversely, in the added-energy model only the amplitude distribution of (partially) coherent oscillations needs to be modified by the stimulus.

First, let us consider the phase-reset model. In accordance with the model, we assume that the amplitude is independent of both the time and phase of the oscillations, so that the probability distribution can be factorised $f^{\mathrm{PR}}(\psi, r, t) = f_1^{\mathrm{PR}}(\psi, t) f_2^{\mathrm{PR}}(r)$ or equivalently in the Fourier domain:

$$\hat{f}^{\mathrm{PR}}(k, r, t) = \hat{f}_1^{\mathrm{PR}}(k, t) f_2^{\mathrm{PR}}(r) \tag{B.8}$$

Consequently, the equation (B.7) reduces to:

$$Z_{\mathrm{PR}}(t) = 2\pi \langle r \rangle \hat{f}_1^{\mathrm{PR}}(-1, t), \tag{B.9}$$

where $\langle r \rangle = \int_0^\infty f_2^{\mathrm{PR}}(r) r dr$ is the average amplitude of the microscopic oscillations. Comparing equations (B.2) and (B.9) we derive that the in the phase-reset model the ensemble amplitude is:

$$R_{\mathrm{PR}}(t) = 2\pi \langle r \rangle \left| \hat{f}_1^{\mathrm{PR}}(-1, t) \right| \tag{B.10}$$

and the ensemble phase is:

$$\phi_{\mathrm{PR}}(t) = \arg[\hat{f}_1^{\mathrm{PR}}(-1, t)]. \tag{B.11}$$

.

According to the added-energy model new oscillators with fixed phase are recruited by the stimulus. Consequently, the distribution of microscopic oscillation amplitudes is modulated by the stimulation independently of the phase. For simplicity, we assume here that the phase advances linearly, so that: $f^{\mathrm{AE}}(\phi, r, t) = f_1^{\mathrm{AE}}(\phi, t) f_2^{\mathrm{AE}}(r, t) = f_0^{\mathrm{AE}}(\phi_0 + \omega t) f_2^{\mathrm{AE}}(r, t)$ or in the Fourier domain $\hat{f}^{\mathrm{AE}}(k, r, t) = \exp(-ik\omega t) \hat{f}_0^{\mathrm{AE}}(k) f_2^{\mathrm{AE}}(r, t)$, where $\hat{f}_0^{\mathrm{AE}}(k) = \frac{1}{2\pi} \int_0^{2\pi} f_0^{\mathrm{AE}}(\phi) \exp(-ik\phi) d\phi$ is the Fourier-transformed initial phase distribution. In contrast with the phase-reset model the distribution over the amplitudes is time-dependent. Taking this into account the probability density function over the ensemble of oscillators can be written as:

$$\hat{f}^{\mathrm{AE}}(k, r, t) = \exp(-ik\omega t) \hat{f}_0^{\mathrm{AE}}(k) f_2^{\mathrm{AE}}(r, t). \tag{B.12}$$

Using equation (B.7) we obtain:

$$Z_{\mathrm{AE}}(t) = 2\pi \hat{f}_0^{\mathrm{AE}}(k) \exp(ik\omega t) \int_0^\infty f_2^{\mathrm{AE}}(r, t) r dr = 2\pi \hat{f}_0^{\mathrm{AE}}(-1) \exp(i\omega t) \langle r(t) \rangle . \tag{B.13}$$

Thus the ensemble amplitude and phase in the added-energy model are given by, respectively:

$$R_{\mathrm{AE}}(t) = 2\pi \langle r(t) \rangle \left| \hat{f}_0^{\mathrm{AE}}(-1) \right| \tag{B.14}$$

$$\phi_{\mathrm{AE}}(t) = \omega t + \arg[\hat{f}_0^{\mathrm{AE}}(-1)] \tag{B.15}$$

where $\langle r(t) \rangle = \int_0^\infty f_2^{\mathrm{AE}}(r, t) r dr$ is a time-dependent average amplitude.

B. Ambiguity between phase and amplitude dynamics: analytical treatment

Note that in both the phase-reset and added-energy models the ensemble amplitude and phase depend on variables which are not observed macroscopically, namely: the Fourier mode of the time-dependent phase distribution $\hat{f}_1^{\mathrm{PR}}(-1,t)$ and the amplitude distribution $f_2^{\mathrm{PR}}(r)$ in the case of the phase-reset model; and the Fourier mode of initial phase distribution $\hat{f}_0^{\mathrm{AE}}(-1)$ and time-dependent amplitude distribution $f_2^{\mathrm{AE}}(r,t)$ in the case of the added-energy model. Without any prior knowledge about these distributions it is always possible to construct both phase-reset and added-energy models which are consistent with the same macroscopic observations. To show that, let us assume that in an EEG or MEG experiment the following response to a presentation of a single stimulus was recorded (again the external noise was neglected):

$$y_{\mathrm{exp}}(t) = R_{\mathrm{exp}}(t)\cos(2\pi f_{\mathrm{exp}} t + \phi_0) \tag{B.16}$$

Note that depending on the amplitude modulation R_{exp}, frequency f_{exp} and initial phase ϕ_0 the model can encompass a large class of ERs. Now, we fit the added-energy model to the generic ER. Since we do not know anything about the microscopic distributions we are allowed to choose freely from all distributions which fulfill the conditions (B.6). For example, let $\omega = 2\pi f_{\mathrm{exp}}$ and:

$$\hat{f}_0^{\mathrm{AE}}(k) = \frac{1}{2\pi}\exp(-ik\phi_0) \tag{B.17}$$

$$f_2^{\mathrm{AE}}(r,t) = \begin{cases} \frac{1}{2R_{\mathrm{exp}}(t)} & \text{if } 0 \le r \le 2R_{\mathrm{exp}}(t)\,, \\ 0 & \text{otherwise.} \end{cases} \tag{B.18}$$

Using the above definitions and equations (B.13) and (B.1) it is easily shown that the measured response (B.16) is obtained.

Equivalently, if we choose the following distributions describing the phase-reset model:

$$\hat{f}_1^{\mathrm{PR}}(k,t) = \frac{1}{2\pi} R_{\mathrm{exp}}(t)^{|k|}\exp\left[-ik(2\pi f_{\mathrm{exp}} t + \phi_0)\right] \tag{B.19}$$

$$f_2^{\mathrm{PR}}(r) = \begin{cases} \frac{1}{2} & \text{if } 0 \le r \le 2\,, \\ 0 & \text{otherwise.} \end{cases} \tag{B.20}$$

and insert them into the equations (B.10) and (B.11) we recover the experimentally recorded ER.

In summary, we showed theoretically that macroscopically measured evoked responses can be described equally well by two general models: one governed only by the phase dynamics and the other governed by amplitude dynamics. These two models reflect two views on ER generation often discussed in the literature: phase-reset

and added-energy mechanisms, respectively. Our argument is not based on a specific realization of the dynamics and therefore applies to any model describing the oscillatory activity, such as the one presented in the main part of our manuscript. Therefore, we conclude that as a matter of principle it is not possible to distinguish between phase-reset and added-energy mechanisms without the knowledge of microscopic properties.

Bibliography

J. Acebron, L. Bonilla, C. J. P. Vicente, F. Ritort, and R. Spigler. The Kuramoto model: A simple paradigm for synchronization phenomena. *Reviews of Modern Physics*, 77:137–185, 2005.

E. D. Adrian and Y. Zotterman. The impulses produced by sensory nerve endings: Part 3. Impulses set up by touch and pressure. *Journal of Physiology*, 61(4):465–483, 1926.

C. Allen and C. Stevens. An evaluation of causes for unreliability of synaptic transmission. *Proceedings of the National Academy of Sciences of the USA*, 91(22): 10380, 1994.

A. Arieli, A. Sterkin, A. Grinvald, and A. Aertsen. Dynamics of ongoing activity: explanation of the large variability in evoked cortical responses. *Science*, 273: 1868–1871, 1996.

B. B. Averbeck, P. E. Latham, and A. Pouget. Neural correlations, population coding and computation. *Nature Reviews Neuroscience*, 7(5):358–366, 2006.

R. Azouz and C. M. Gray. Cellular mechanisms contributing to response variability of cortical neurons in vivo. *Journal of Neuroscience*, 19(6):2209–2223, 1999.

S. Baker, G. Curio, and R. Lemon. EEG oscillations at 600 Hz are macroscopic markers for cortical spike bursts. *Journal of Physiology*, 550:529–534, 2003.

S. N. Baker, R. Spinks, A. Jackson, and R. N. Lemon. Synchronization in monkey motor cortex during a precision grip task. I. Task-dependent modulation in single-unit synchrony. *Journal of Neurophysiology*, 85(2):869–885, 2001.

H. B. Barlow. Single units and sensation: a neuron doctrine for perceptual psychology? *Perception*, 1(4):371–394, 1972.

R. J. Barlow. *Statistics: A Guide to the Use of Statistical Methods in the Physical Sciences*. Wiley-Blackwell, Chichester, 1989.

R. J. Barry. Evoked activity and EEG phase resetting in the genesis of auditory Go/NoGo ERPs. *Biological Physiology*, 80:292–299, 2009.

D. Barth. Submillisecond synchronization of fast electrical oscillations in neocortex. *Journal of Neuroscience*, 23:2502–2510, 2003.

M. Bazhenov and I. Timofeev. Thalamocortical oscillations. *Scholarpedia*, 1(6):1319, 2006.

M. Bazhenov, I. Timofeev, M. Steriade, and T. J. Sejnowski. Model of thalamocortical slow-wave sleep oscillations and transitions to activated states. *Journal of Neuroscience*, 22(19):8691–8704, 2002.

R. Becker, P. Ritter, and A. Villringer. Influence of ongoing alpha rhythm on the visual evoked potential. *Neuroimage*, 39:707–716, 2008.

C. Bédard, H. Kröger, and A. Destexhe. Model of low-pass filtering of local field potentials in brain tissue. *Physical Review E*, 73(5):051911, 2006.

A. Belitski, A. Gretton, C. Magri, Y. Murayama, M. Montemurro, N. Logothetis, and S. Panzeri. Low-frequency local field potentials and spikes in primary visual cortex convey independent visual information. *Journal of Neuroscience*, 28:5696–5709, 2008.

J. Benda and A. V. M. Herz. A universal model for spike-frequency adaptation. *Neural Computation*, 15(11):2523–2564, 2003.

Y. Benjamini and Y. Hochberg. Controlling the false discovery rate: A practical and powerful approach to multiple testing. *Journal of the Royal Statistical Society B*, 57:289–300, 1995.

P. Berens, G. A. Keliris, A. S. Ecker, N. K. Logothetis, and A. S. Tolias. Comparing the feature selectivity of the gamma-band of the local field potential and the underlying spiking activity in primate visual cortex. *Frontiers in Systems Neuroscience*, 2:2, 2008.

H. Berger. Über das Elektrenkephalogramm des Menschen. *Archiv für Psychiatrie und Nervenkrankheiten*, 87:527, 1929.

M. Berry and M. Meister. Refractoriness and neural precision. *Journal of Neuroscience*, 18(6):2200, 1998.

W. Bialek and F. Rieke. Reliability and information transmission in spiking neurons. *Trends in Neurosciences*, 15(11):428 – 434, 1992.

A. Bibbig, R. D. Traub, and M. A. Whittington. Long-range synchronization of gamma and beta oscillations and the plasticity of excitatory and inhibitory synapses: a network model. *Journal of Neurophysiology*, 88:1634–1654, 2002.

M. Bonte, G. Valente, and E. Formisano. Dynamic and task-dependent encoding of speech and voice by phase reorganization of cortical oscillations. *Journal of Neuroscience*, 29:1699–1706, 2009.

R. Bracewell. *The Fourier Transform & Its Applications*. McGraw-Hill, Singapore, 1999.

A. Bragin, J. Engel, C. L. Wilson, I. Fried, and G. Buzsáki. High-frequency oscillations in human brain. *Hippocampus*, 9(2):137–142, 1999.

E. Brown, J. Moehlis, and P. Holmes. On the phase reduction and response dynamics of neural oscillator populations. *Neural Computation*, 16:673–715, 2004.

J. C. Brumberg, L. G. Nowak, and D. A. McCormick. Ionic mechanisms underlying repetitive high-frequency burst firing in supragranular cortical neurons. *Journal of Neuroscience*, 20(13):4829–4843, 2000.

R. M. Bruno and B. Sakmann. Cortex Is Driven by Weak but Synchronously Active Thalamocortical Synapses. *Science*, 312(5780):1622 –1627, 2006.

J. S. Buchwald, E. S. Halas, and S. Schramm. Comparison of multiple-unit and electroencephalogram activity recorded from the same brain sites during behavioural conditioning. *Nature*, 205(4975):1012–1014, 1965.

T. H. Bullock, M. C. McClune, J. Z. Achimowicz, V. J. Iragui-Madoz, R. B. Duckrow, and S. S. Spencer. EEG coherence has structure in the millimeter domain: subdural and hippocampal recordings from epileptic patients. *Electroencephalography and Clinical Neurophysiology*, 95:161–177, 1995.

G. Buzsaki. Large-scale recording of neuronal ensembles. *Nature Neuroscience*, 7: 446–451, 2004.

G. Buzsaki and A. Draguhn. Neuronal oscillations in cortical networks. *Science*, 304 (5679):1926–1929, 2004.

G. Buzsaki, Z. Horvath, R. Urioste, J. Hetke, and K. Wise. High-frequency network oscillation in the hippocampus. *Science*, 256(5059):1025–1027, 1992.

P. Celka, K. Le, and T. Cutmore. Noise reduction in rhythmic and multitrial biosignals with applications to event-related potentials. *IEEE Transactions on Biomedical Engineering*, 55(7):1809–1821, 2008.

F. Chance, L. Abbott, and A. Reyes. Gain modulation from background synaptic input. *Neuron*, 35(4):773–782, 2002.

C. Chapman, W. Jiang, and Y. Lamarre. Modulation of lemniscal input during conditioned arm movements in the monkey. *Experimental Brain Research*, 72: 316–334, 1988.

A. Compte, M. V. Sanchez-Vives, D. A. McCormick, and X. Wang. Cellular and network mechanisms of slow oscillatory activity (<1 Hz) and wave propagations in a cortical network model. *Journal of Neurophysiology*, 89(5):2707–2725, 2003.

T. M. Cover and J. A. Thomas. *Elements of information theory*. John Wiley and Sons, New Jersey, 2006.

R. Q. Cracco and J. B. Cracco. Somatosensory evoked potential in man: far field potentials. *Electroencephalography and Clinical Neurophysiology*, 41:460–466, 1976.

O. D. Creutzfeldt, S. Watanabe, and H. D. Lux. Relations between EEG phenomena and potentials of single cortical cells. I. Evoked responses after thalamic and erpicortical stimulation. *Electroencephalography and Clinical Neurophysiology*, 20 (1):1–18, 1966.

S. J. Cruikshank, T. J. Lewis, and B. W. Connors. Synaptic basis for intense thalamocortical activation of feedforward inhibitory cells in neocortex. *Nature Neuroscience*, 10(4):462–468, 2007.

G. Curio, B. Mackert, M. Burghoff, R. Koetitz, K. Abraham-Fuchs, and W. Härer. Localization of evoked neuromagnetic 600 Hz activity in the cerebral somatosensory system. *Electroencephalography and Clinical Neurophysiology*, 91:483–487, 1994.

F. L. da Silva. Dynamics of EEGs as signals of neuronal populations: Models and theoretical considerations. In E. Niedermeyer and F. L. D. Silva, editors, *Electroencephalography: Basic Principles, Clinical Applications, and Related Fields*, pages 85–106. Lippincott Williams & Wilkins, Philadelphia, 2004.

F. L. da Silva and A. van Rotterdam. Biophysical aspects of EEG and magnetoencephalogram generation. In E. Niedermeyer and F. L. D. Silva, editors, *Electroencephalography: Basic Principles, Clinical Applications, and Related Fields*, pages 108–125. Lippincott Williams & Wilkins, Philadelphia, 2004.

O. David, S. J. Kiebel, L. M. Harrison, J. Mattout, J. M. Kilner, and K. J. Friston. Dynamic causal modeling of evoked responses in EEG and MEG. *Neuroimage*, 30 (4):1255–1272, 2006.

G. Dawson. Cerebral responses to nerve stimulation in man. *British Medical Bulletin*, 6:326–329, 1950.

P. Dayan and L. Abbott. *Theoretical Neuroscience: Computational and Mathematical Modeling of Neural Systems*. MIT Press, Cambridge, 2001.

R. de Ruyter, G. Lewen, S. Strong, R. Koberle, and W. Bialek. Reproducibility and variability in neural spike trains. *Science*, 275:1805–1808, 1997.

R. deCharms and M. Merzenich. Primary cortical representation of sounds by the coordination of action-potential timing. *Nature*, 381:610–613, 1996.

G. Deco, V. K. Jirsa, P. A. Robinson, M. Breakspear, and K. Friston. The dynamic brain: From spiking neurons to neural masses and cortical fields. *PLoS Computational Biology*, 4:e1000092, 2008.

A. Destexhe, D. Contreras, and M. Steriade. Cortically-induced coherence of a thalamic-generated oscillation. *Neuroscience*, 92:427–443, 1999.

M. R. Deweese and A. M. Zador. Shared and private variability in the auditory cortex. *Journal of Neurophysiology*, 92(3):1840–1855, 2004.

R. E. Dustman and E. C. Beck. Phase of alpha brain waves, reaction time and visually evoked potentials. *Electroencephalography and Clinical Neurophysiology*, 18:433–440, 1965.

R. Eckhorn and U. Thomas. A new method for the insertion of multiple microprobes into neural and muscular tissue, including fiber electrodes, fine wires, needles and microsensors. *Journal of Neuroscience Methods*, 49:175–179, 1993.

R. Eckhorn, R. Bauer, W. Jordan, M. Brosch, W. Kruse, M. Munk, and H. J. Reitboeck. Coherent oscillations: a mechanism of feature linking in the visual cortex? multiple electrode and correlation analyses in the cat. *Biological Cybernetics*, 60 (2):121–130, 1988.

B. Efron and R. Tibshirani. *An Introduction to the Bootstrap*. Chapman & Hall/CRC, Boca Ratton, 1994.

A. K. Engel, P. Fries, and W. Singer. Dynamic predictions: oscillations and synchrony in top-down processing. *Nature Reviews Neuroscience*, 2(10):704–716, 2001.

T. A. Engel, L. Schimansky-Geier, A. Herz, S. Schreiber, and I. Erchova. Subthreshold membrane-potential resonances shape spike-train patterns in the entorhinal cortex. *Journal of Neurophysiology*, 100(3):1576–1589, 2008.

A. A. Faisal, L. P. J. Selen, and D. M. Wolpert. Noise in the nervous system. *Nature Reviews Neuroscience*, 9(4):292–303, 2008.

F. Farkhooi, M. F. Strube-Bloss, and M. P. Nawrot. Serial correlation in neural spike trains: Experimental evidence, stochastic modeling, and single neuron variability. *Physical Review E*, 79(2):021905, 2009.

J. Fell, T. Dietl, T. Grunwald, M. Kurthen, P. Klaver, P. Trautner, C. Schaller, C. E. Elger, and G. Fernández. Neural bases of cognitive ERPs: more than phase reset. *Journal of Cognitive Neuroscience*, 16:1595–1604, 2004.

J. M. Fellous, M. Rudolph, A. Destexhe, and T. J. Sejnowski. Synaptic background noise controls the input/output characteristics of single cells in an in vitro model of in vivo activity. *Neuroscience*, 122(3):811 – 829, 2003.

J.-M. Fellous, P. Tiesinga, P. Thomas, and T. Sejnowski. Discovering spike patterns in neuronal responses. *Journal of Neuroscience*, 24:2989–3001, 2004.

A. Fontanini and D. B. Katz. Behavioral states, network states, and sensory response variability. *Journal of Neurophysiology*, 100(3):1160–1168, 2008.

M. D. Fox, A. Z. Snyder, J. M. Zacks, and M. E. Raichle. Coherent spontaneous activity accounts for trial-to-trial variability in human evoked brain responses. *Nature Neuroscience*, 9(1):23–25, 2006.

A. Frien and R. Eckhorn. Functional coupling shows stronger stimulus dependency for fast oscillations than for low-frequency components in striate cortex of awake monkey. *European Journal of Neuroscience*, 12(4):1466–1478, 2000.

P. Fries, J. H. Reynolds, A. E. Rorie, and R. Desimone. Modulation of oscillatory neuronal synchronization by selective visual attention. *Science*, 291(5508):1560–1563, 2001.

K. Funke and N. Kerscher. High-frequency (300-800 Hz) components in cat geniculate (dLGN) early visual responses. *Journal of Physiology*, 94(5-6):411–425, 2000.

F. Gabbiani and C. Koch. Principles of spike train analysis. In C. Koch and I. Segev, editors, *Methods in Neural Modeling: From Ions to Networks*. MIT Press, Cambridge, 1999.

Z. Gil, B. Connors, and Y. Amitai. Differential regulation of neocortical synapses by neuromodulators and activity. *Neuron*, 19(3):679–686, 1997.

Z. Gil, B. Connors, and Y. Amitai. Efficacy of thalamocortical and intracortical synaptic connections: quanta, innervation, and reliability. *Neuron*, 23(2):385–397, 1999.

R. Gobbelé, T. D. Waberski, S. Kuelkens, W. Sturm, G. Curio, and H. Buchner. Thalamic and cortical high-frequency (600 Hz) somatosensory-evoked potential (SEP) components are modulated by slight arousal changes in awake subjects. *Experimental Brain Research*, 133(4):506–513, 2000.

C. M. Gray and D. A. McCormick. Chattering cells: Superficial pyramidal neurons contributing to the generation of synchronous oscillations in the visual cortex. *Science*, 274:109–113, 1996.

C. M. Gray and W. Singer. Stimulus-specific neuronal oscillations in orientation columns of cat visual cortex. *Proceedings of the National Academy of Sciences of the USA*, 86(5):1698–1702, 1989.

P. R. Gray. Conditional Probability Analyses of the Spike Activity of Single Neurons. *Biophysical Journal*, 7(6):759–777, 1967.

D. J. Griffiths. *Introduction to Electrodynamics*. Prentice Hall, New Jersey, 1999.

B. Gutkin, G. Ermentrout, and A. Reyes. Phase-response curves give the responses of neurons to transient inputs. *Journal of Neurophysiology*, 94:1623–1635, 2005.

R. Guttman, S. Lewis, and J. Rinzel. Control of repetitive firing in squid axon membrane as a model for a neuroneoscillator. *Journal of Physiology*, 305:377–395, 1980.

P. Halboni, R. Kaminski, R. Gobbelé, S. Züchner, T. D. Waberski, C. S. Herrmann, R. Töpper, and H. Buchner. Sleep stage dependant changes of the high-frequency part of the somatosensory evoked potentials at the thalamus and cortex. *Clinical Neurophysiology*, 111(12):2277–2284, 2000.

R. Hanajima, R. Chen, P. Ashby, A. M. Lozano, W. D. Hutchison, K. D. Davis, and J. O. Dostrovsky. Very fast oscillations evoked by median nerve stimulation in the human thalamus and subthalamic nucleus. *Journal of Neurophysiology*, 92(6): 3171–3182, 2004.

D. Hansel, G. Mato, and C. Meunier. Clustering and slow switching in globally coupled phase oscillators. *Physical Review E*, 48:3470–3477, 1993.

D. Hansel, G. Mato, and C. Meunier. Synchrony in excitatory neural networks. *Neural Computation*, 7(2):307–337, 1995.

S. Hanslmayr, W. Klimesch, P. Sauseng, W. Gruber, M. Doppelmayr, R. Freunberger, T. Pecherstorfer, and N. Birbaumer. Alpha phase reset contributes to the generation of ERPs. *Cereb Cortex*, 17:1–8, 2006.

I. Hashimoto, T. Mashiko, and T. Imada. Somatic evoked high-frequency magnetic oscillations reflect activity of inhibitory interneurons in the human somatosensory cortex. *Electroencephalography and Clinical Neurophysiology*, 100(3):189–203, 1996.

L. Hazan, M. Zugaro, and G. Buzsáki. Klusters, NeuroScope, NDManager: A free software suite for neurophysiological data processing and visualization. *Journal of Neuroscience Methods*, 155(2):207–216, 2006.

D. Holcman and M. Tsodyks. The emergence of up and down states in cortical networks. *PLoS Computational Biology*, 2(3):e23, 2006.

S. L. Hooper. Transduction of temporal patterns by single neurons. *Nature Neuroscience*, 1(8):720–726, 1998.

L. Hubert and P. Arabie. Comparing partitions. *Journal of Classification*, 2(1): 193–218, 1985.

J. Hunter, J. Milton, P. Thomas, and J. Cowan. Resonance effect for neural spike time reliability. *Journal of Neurophysiology*, 80:1427–1438, 1998.

B. Hutcheon, R. M. Miura, and E. Puil. Subthreshold membrane resonance in neocortical neurons. *Journal of Neurophysiology*, 76(2):683–697, 1996.

J. Huxter, N. Burgess, and J. O'Keefe. Independent rate and temporal coding in hippocampal pyramidal cells. *Nature*, 425(6960):828–832, 2003.

H. Ikeda, L. Leyba, A. Bartolo, Y. Wang, and Y. C. Okada. Synchronized spikes of thalamocortical axonal terminals and cortical neurons are detectable outside the pig brain with MEG. *Journal of Neurophysiology*, 87(1):626–630, 2002.

Y. Ikegaya, G. Aaron, R. Cossart, D. Aronov, I. Lampl, D. Ferster, and R. Yuste. Synfire chains and cortical songs: Temporal modules of cortical activity. *Science*, 304(5670):559–564, 2004.

E. M. Izhikevich. *Dynamical Systems in Neuroscience: The Geometry of Excitability and Bursting*. The MIT Press, Cambridge, Massachusetts, 2010.

E. M. Izhikevich and G. M. Edelman. Large-scale model of mammalian thalamocortical systems. *Proceedings of the National Academy of Sciences*, 105(9):3593–3598, 2008.

J. D. Jackson. *Classical Electrodynamics*. John Wiley and Sons, New York, 1998.

B. Jansen, G. Agarwal, A. Hegde, and N. Boutros. Phase synchronization of the ongoing EEG and auditory EP generation. *Clinical Neurophysiology*, 114:79, 2003.

J. D. Jirsch, E. Urrestarazu, P. LeVan, A. Olivier, F. Dubeau, and J. Gotman. High-frequency oscillations during human focal seizures. *Brain*, 129(6):1593–1608, 2006.

D. H. Johnson and A. Swami. The transmission of signals by auditory-nerve fiber discharge patterns. *Journal of Acoustical Society of America*, 74(2):493–501, 1983.

M. Jones, K. MacDonald, B. Choi, F. Dudek, and D. Barth. Intracellular correlates of fast (>200 Hz) electrical oscillations in rat somatosensory cortex. *Journal of Neurophysiology*, 84:1505–1518, 2000.

S. Jones, D. Pritchett, S. Stufflebeam, M. Hamalainen, and C. Moore. Neural correlates of tactile detection: a combined magnetoencephalography and biophysically based computational modeling study. *Journal of Neuroscience*, 27:10751–10764, 2007.

S. R. Jones, D. L. Pritchett, M. A. Sikora, S. M. Stufflebeam, M. Hamalainen, and C. I. Moore. Quantitative analysis and biophysically realistic neural modeling of the MEG mu rhythm: Rhythmogenesis and modulation of sensory evoked responses. *Journal of Neurophysiology*, 102:3554–3572, 2009.

M. Joshua, S. Elias, O. Levine, and H. Bergman. Quantifying the isolation quality of extracellularly recorded action potentials. *Journal of Neuroscience Methods*, 163 (2):267–282, 2007.

P. Kara, P. Reinagel, and R. C. Reid. Low Response Variability in Simultaneously Recorded Retinal, Thalamic, and Cortical Neurons. *Neuron*, 27(3):635–646, 2000.

R. Kass and V. Ventura. A spike-train probability model. *Neural Computation*, 13 (8):1713–1720, 2001.

S. Katzner, I. Nauhaus, A. Benucci, V. Bonin, D. L. Ringach, and M. Carandini. Local origin of field potentials in visual cortex. *Neuron*, 61:35–41, 2009.

L. Kaufman and P. Rousseeuw. *Finding Groups in Data: An Introduction to Cluster Analysis*. John Wiley and Sons, New York, 1990.

V. B. Kazantsev, V. I. Nekorkin, V. I. Makarenko, and R. Llinás. Self-referential phase reset based on inferior olive oscillator dynamics. *Proceedings of the National Academy of Sciences of the USA*, 101:18183–18188, 2004.

J. Keat, P. Reinagel, R. C. Reid, and M. Meister. Predicting every spike: a model for the responses of visual neurons. *Neuron*, 30(3):803–817, 2001.

T. Kenet, D. Bibitchkov, M. Tsodyks, A. Grinvald, and A. Arieli. Spontaneously emerging cortical representations of visual attributes. *Nature*, 425:954–956, 2003.

W. Klimesch, S. Hanslmayr, P. Sauseng, and W. R. Gruber. Distinguishing the evoked response from phase reset: a comment to Mäkinen et al. *Neuroimage*, 29: 808–811, 2006.

F. Klostermann, G. Nolte, and G. Curio. Independent short-term variability of spike-like (600 Hz) and postsynaptic (N20) cerebral SEP components. *Neuroreport*, 12 (2):349–352, 2001.

C. Koch. *Biophysics of computation: information processing in single neurons*. Oxford University Press, New York, 1999.

P. König, A. K. Engel, and W. Singer. Relation between oscillatory activity and long-range synchronization in cat visual cortex. *Proceedings of the National Academy of Sciences of the USA*, 92(1):290 –294, 1995.

S. Koyama and R. Kass. Spike train probability models for stimulus-driven leaky integrate-and-fire neurons. *Neural Computation*, 20(1776-1795):1776–1795, 2008.

R. Krahe and F. Gabbiani. Burst firing in sensory systems. *Nature Reviews Neuroscience*, 5(1):13–23, 2004.

A. Kumar, S. Rotter, and A. Aertsen. Spiking activity propagation in neuronal networks: reconciling different perspectives on neural coding. *Nature Reviews Neuroscience*, 11(9):615–627, 2010.

Y. Kuramoto. *Chemical Oscillations, Waves, and Turbulence*. Springer-Verlag, Berlin, 1984.

T. D. Lagerlund and G. A. Worrell. EEG source localization (model-dependent and model-independent methods). In E. Niedermeyer and F. L. D. Silva, editors, *Electroencephalography: Basic Principles, Clinical Applications, and Related Fields*, pages 829–844. Lippincott Williams & Wilkins, Philadelphia, 2004.

M. Le Van Quyen, J. Foucher, J. Lachaux, E. Rodriguez, A. Lutz, J. Martinerie, and F. J. Varela. Comparison of Hilbert transform and wavelet methods for the analysis of neuronal synchrony. *Journal of Neuroscience Methods*, 111(2):83 – 98, 2001.

M. Lengyel, J. Kwag, O. Paulsen, and P. Dayan. Matching storage and recall: hippocampal spike timing-dependent plasticity and phase response curves. *Nature Neuroscience*, 8:1677–1683, 2005.

M. S. Lewicki. A review of methods for spike sorting: the detection and classification of neural action potentials. *Network*, 9(4):53, 1998.

B. Li, K. Funke, F. Wörgötter, and U. T. Eysel. Correlated variations in EEG pattern and visual responsiveness of cat lateral geniculate relay cells. *Journal of Physiology*, 514(3):857–874, 1999.

H. Lindén, K. H. Pettersen, and G. T. Einevoll. Intrinsic dendritic filtering gives low-pass power spectra of local field potentials. *Journal of Computational Neuroscience*, 29(3):423–444, 2010.

J. Lisman. Bursts as a unit of neural information: making unreliable synapses reliable. *Trends in Neurosciences*, 20:38–43, 1997.

J. E. Lisman, S. Raghavachari, and R. W. Tsien. The sequence of events that underlie quantal transmission at central glutamatergic synapses. *Nature Reviews Neuroscience*, 8(8):597–609, 2007.

N. K. Logothetis, C. Kayser, and A. Oeltermann. In vivo measurement of cortical impedance spectrum in monkeys: Implications for signal propagation. *Neuron*, 55 (5):809–823, 2007.

W. Maass and A. M. Zador. Dynamic stochastic synapses as computational units. *Neural Computation*, 11(4):903–917, 1999.

Z. Mainen and T. Sejnowski. Reliability of spike timing in neocortical neurons. *Science*, 268:1503–1506, 1995.

S. Makeig, M. Westerfield, T. Jung, S. Enghoff, J. Townsend, E. Courchesne, and T. Sejnowski. Dynamic brain sources of visual evoked responses. *Science*, 295: 690–694, 2002.

V. Mäkinen, H. Tiitinen, and P. May. Auditory event-related responses are generated independently of ongoing brain activity. *Neuroimage*, 24:961–968, 2005.

J. Malmivuo and R. Plonsey. *Bioelectromagnetism: Principles and Applications of Bioelectric and Biomagnetic Fields.* Oxford University Press, New York, Oxford, 1995.

A. Mazaheri and O. Jensen. Posterior alpha activity is not phase-reset by visual stimuli. *Proceedings of the National Academy of Sciences of the USA*, 103:2948–2952, 2006.

A. Mazaheri and O. Jensen. Asymmetric amplitude modulations of brain oscillations generate slow evoked responses. *Journal of Neuroscience*, 28:7781–7787, 2008.

R.-M. Memmesheimer and M. Timme. Designing the dynamics of spiking neural networks. *Physical Review Letters*, 97:188101, 2006.

J. C. Middlebrooks, L. Xu, A. C. Eddins, and D. M. Green. Codes for sound-source location in nontonotopic auditory cortex. *Journal of Neurophysiology*, 80(2):863–881, 1998.

M. I. Miller. Algorithms for removing recovery-related distortion from auditory-nerve discharge patterns. *Journal of Acoustical Society of America*, 77(4):1452–1464, 1985.

U. Mitzdorf. Current source-density method and application in cat cerebral cortex: investigation of evoked potentials and EEG phenomena. *Physiological Reviews*, 65 (1):37–100, 1985.

V. B. Mountcastle. The columnar organization of the neocortex. *Brain*, 120(4): 701–722, 1997.

V. B. Mountcastle, H. J. Reitboeck, G. F. Poggio, and M. A. Steinmetz. Adaptation of the Reitboeck method of multiple microelectrode recording to the neocortex of the waking monkey. *Journal of Neuroscience Methods*, 36(1):77–84, 1991.

S. Murakami and Y. Okada. Contributions of principal neocortical neurons to magnetoencephalography and electroencephalography signals. *Journal of Physiology*, 575(3):925 –936, 2006.

S. Murakami, T. Zhang, A. Hirose, and Y. Okada. Physiological origins of evoked magnetic fields and extracellular field potentials produced by guinea-pig CA3 hippocampal slices. *Journal of Physiology*, 544(1):237, 2002.

S. Murakami, A. Hirose, and Y. C. Okada. Contribution of ionic currents to magnetoencephalography (MEG) and electroencephalography (EEG) signals generated by guinea-pig CA3 slices. *Journal of Physiology*, 553(Pt 3):975–985, 2003.

Y. Naruse, A. Matani, Y. Miyawaki, and M. Okada. Influence of coherence between multiple cortical columns on alpha rhythm: a computational modeling study. *Human Brain Mapping*, 31(5):703–715, 2010.

M. P. Nawrot, C. Boucsein, V. Rodriguez-Molina, A. Aertsen, S. Grün, and S. Rotter. Serial interval statistics of spontaneous activity in cortical neurons in vivo and in vitro. *Neurocomputing*, 70(10-12):1717 – 1722, 2007.

I. Nemenman, G. D. Lewen, W. Bialek, and R. R. de Ruyter van Steveninck. Neural coding of natural stimuli: Information at sub-millisecond resolution. *PLoS Computational Biology*, 4(3):e1000025, 2008.

E. Niedermeyer. The normal EEG of the waking adult. In E. Niedermeyer and F. L. D. Silva, editors, *Electroencephalography: Basic Principles, Clinical Applications, and Related Fields*, pages 167–192. Lippincott Williams & Wilkins, Philadelphia, 2004.

V. V. Nikulin, K. Linkenkaer-Hansen, G. Nolte, S. Lemm, K. R. Müller, R. J. Ilmoniemi, and G. Curio. A novel mechanism for evoked responses in the human brain. *European Journal of Neuroscience*, 25:3146–3154, 2007.

V. V. Nikulin, K. Linkenkaer-Hansen, G. Nolte, and G. Curio. Non-zero mean and asymmetry of neuronal oscillations have different implications for evoked responses. *Clinical Neurophysiology*, 121(2):186–193, 2010.

P. L. Nunez and R. Srinivasan. *Electric Fields of the Brain: The Neurophysics of EEG*. Oxford University Press, New York, 2005.

T. Pavlidis. *Biological Oscillators: Their Mathematical Analysis*. Academic Press Inc, 1974.

D. Perkel and T. Bullock. Neural coding. *Neurosciences Research Program Bulletin*, 1968.

R. S. Petersen, S. Panzeri, and M. E. Diamond. Population coding of stimulus location in rat somatosensory cortex. *Neuron*, 32(3):503–514, 2001.

R. S. Petersen, S. Panzeri, and M. E. Diamond. Population coding in somatosensory cortex. *Current Opinion in Neurobiology*, 12:441–447, 2002.

N. N. Peterson, C. E. Schroeder, and J. C. Arezzo. Neural generators of early cortical somatosensory evoked potentials in the awake monkey. *Electroencephalography and Clinical Neurophysiology*, 96(3):248–260, 1995.

K. H. Pettersen and G. T. Einevoll. Amplitude variability and extracellular low-pass filtering of neuronal spikes. *Biophysical Journal*, 94(3):784–802, 2008.

A. Pikovsky, M. Rosenblum, and J. Kurths. *Synchronization: A Universal Concept in Nonlinear Science*. Cambridge University Press, Cambridge, UK, 2002.

G. F. Poggio and L. J. Viernstein. Time series analysis of impulse sequences of thalamic somatic sensory neurons. *Journal of Neurophysiology*, 27:517–545, 1964.

C. M. Portas, G. Rees, A. M. Howseman, O. Josephs, R. Turner, and C. D. Frith. A specific role for the thalamus in mediating the interaction of attention and arousal in humans. *Journal of Neuroscience*, 18(21):8979–8989, 1998.

A. Rauch, G. L. Camera, H. Lüscher, W. Senn, and S. Fusi. Neocortical pyramidal cells respond as integrate-and-fire neurons to in vivo-like input currents. *Journal of Neurophysiology*, 90(3):1598 –1612, 2003.

S. Ray, N. E. Crone, E. Niebur, P. J. Franaszczuk, and S. S. Hsiao. Neural correlates of high-gamma oscillations (60-200 Hz) in macaque local field potentials and their potential implications in electrocorticography. *Journal of Neuroscience*, 28(45): 11526–11536, 2008.

D. S. Reich, J. D. Victor, and B. W. Knight. The power ratio and the interval map: Spiking models and extracellular recordings. *Journal of Neuroscience*, 18 (23):10090–10104, 1998.

D. S. Reich, F. Mechler, K. Purpura, and J. Victor. Interspike intervals, receptive fields, and information encoding in primary visual cortex. *Journal of Neuroscience*, 20:1964–1974, 2000.

D. S. Reich, F. Mechler, and J. D. Victor. Temporal coding of contrast in primary visual cortex: When, what, and why. *Journal of Neurophysiology*, 85(3):1039–1050, 2001.

A. D. Reyes and E. E. Fetz. Effects of transient depolarizing potentials on the firing rate of cat neocortical neurons. *Journal of Neurophysiology*, 69(5):1673–1683, 1993.

F. Rieke and D. Warland. *Spikes: exploring the neural code*. The MIT Press, Cambridge, USA, 1999.

P. Ritter and R. Becker. Detecting alpha rhythm phase reset by phase sorting: caveats to consider. *Neuroimage*, 47(1):1–4, 2009.

P. Ritter, F. Freyer, G. Curio, and A. Villringer. High-frequency (600 Hz) population spikes in human EEG delineate thalamic and cortical fMRI activation sites. *Neuroimage*, 42(2):483–490, 2008.

P. A. Robinson, C. J. Rennie, D. L. Rowe, and S. C. O'Connor. Estimation of multiscale neurophysiologic parameters by electroencephalographic means. *Human Brain Mapping*, 23(1):53–72, 2004.

P. A. Robinson, C. J. Rennie, D. L. Rowe, S. C. O'Connor, and E. Gordon. Multiscale brain modelling. *Philosophical Transactions of the Royal Society B: Biological Sciences*, 360(1457):1043 –1050, 2005.

M. Rosanova and I. Timofeev. Neuronal mechanisms mediating the variability of somatosensory evoked potentials during sleep oscillations in cats. *Journal of Physiology*, 562(2):569–582, 2005.

J. S. Rothman, L. Cathala, V. Steuber, and R. A. Silver. Synaptic depression enables neuronal gain control. *Nature*, 457(7232):1015–1018, 2009.

P. J. Rousseeuw. Silhouettes: A graphical aid to the interpretation and validation of cluster analysis. *Journal of Computational and Applied Mathematics*, 20:53–65, 1987.

A. Roxin, V. Hakim, and N. Brunel. The statistics of repeating patterns of cortical activity can be reproduced by a model network of stochastic binary neurons. *Journal of Neuroscience*, 28(42):10734–10745, 2008.

H. Sakaguchi, S. Shinomoto, and Y. Kuramoto. Local and global self-entrainments in oscillator lattices. *Progress of Theoretical Physics*, 77(5):1005–1010, 1987.

P. Sauseng, W. Klimesch, M. Doppelmayr, T. Pecherstorfer, R. Freunberger, and S. Hanslmayr. EEG alpha synchronization and functional coupling during top-down processing in a working memory task. *Human Brain Mapping*, 26(2):148–155, 2005.

P. Sauseng, W. Klimesch, W. R. Gruber, S. Hanslmayr, R. Freunberger, and M. Doppelmayr. Are event-related potential components generated by phase resetting of brain oscillations? a critical discussion. *Neuroscience*, 146:1435–1444, 2007.

B. M. Sayers, H. A. Beagley, and W. R. Henshall. The mechansim of auditory evoked EEG responses. *Nature*, 247:481–483, 1974.

H. J. Scheer, T. Sander, and L. Trahms. The influence of amplifier, interface and biological noise on signal quality in high-resolution EEG recordings. *Physiological Measurement*, 27(2):109–117, 2006.

H. G. Schuster and P. Wagner. A model for neuronal oscillations in the visual cortex. 1. Mean-field theory and derivation of the phase equations. *Biological Cybernetics*, 64:77–82, 1990.

P. Seliger, S. C. Young, and L. S. Tsimring. Plasticity and learning in a network of coupled phase oscillators. *Physical Review E*, 65:041906, 2002.

K. Sen, J. C. Jorge-Rivera, E. Marder, and L. F. Abbott. Decoding synapses. *The Journal of Neuroscience: The Official Journal of the Society for Neuroscience*, 16 (19):6307–6318, 1996.

M. Shadlen and W. Newsome. The variable discharge of cortical neurons: Implications for connectivity, computation, and information coding. *Journal of Neuroscience*, 18(10):3870–3896, 1998.

A. S. Shah, S. L. Bressler, K. H. Knuth, M. Ding, A. D. Mehta, I. Ulbert, and C. E. Schroeder. Neural dynamics and the fundamental mechanisms of event-related brain potentials. *Cerebral Cortex*, 14:476–483, 2004.

G. Shepherd. *The Synaptic Organization of the Brain.* Oxford University Press, New York, 2004.

H. Shimazu, R. Kaji, T. Tsujimoto, N. Kohara, A. Ikeda, J. Kimura, and H. Shibasaki. High-frequency sep components generated in the somatosensory cortex of the monkey. *Neuroreport*, 11:2821–2826, 2000.

Y. Shu, A. Hasenstaub, and D. McCormick. Turning on and off recurrent balanced cortical activity. *Nature*, 423(6937):288–293, 2003.

M. Siegel and P. König. A functional gamma-band defined by stimulus-dependent synchronization in area 18 of awake behaving cats. *Journal of Neuroscience*, 23 (10):4251–4260, 2003.

W. R. Softky and C. Koch. The highly irregular firing of cortical cells is inconsistent with temporal integration of random EPSPs. *Journal of Neuroscience*, 13(1):334–350, 1993.

H. Sompolinsky, D. Golomb, and D. Kleinfeld. Global processing of visual stimuli in a neural network of coupled oscillators. *Proceedings of the National Academy of Sciences of the USA*, 87:7200–7204, 1990.

E. Speckmann and C. E. Elger. Introduction to the neurophysiological basis of the eeg and dc potentials. In E. Niedermeyer and F. H. L. da Silva, editors, *Electroencephalography: Basic Principles, Clinical Applications, and Related Fields*, pages 17–31. Lippincott Williams & Wilkins, Philadelphia, 2004.

M. Steriade, I. Timofeev, and F. Grenier. Natural waking and sleep states: a view from inside neocortical neurons. *Journal of Neurophysiology*, 85(5):1969–1985, 2001.

P. Stern, F. A. Edwards, and B. Sakmann. Fast and slow components of unitary EPSCs on stellate cells elicited by focal stimulation in slices of rat visual cortex. *Journal of Physiology*, 449:247–278, 1992.

C. F. Stevens and A. M. Zador. Input synchrony and the irregular firing of cortical neurons. *Nature Neuroscience*, 1(3):210–217, 1998.

K. M. Stiefel, B. S. Gutkin, and T. J. Sejnowski. Cholinergic neuromodulation changes phase response curve shape and type in cortical pyramidal neurons. *PLoS One*, 3:e3947, 2008.

S. Strogatz. From Kuramoto to Crawford: exploring the onset of synchronization in populations of coupled oscillators. *Physica D*, 143:1–20, 2000.

H. A. Swadlow and A. G. Gusev. The impact of 'bursting' thalamic impulses at a neocortical synapse. *Nature Neuroscience*, 4(4):402–408, 2001.

A. Szucs, R. Pinto, M. Rabinovich, H. di Abarbanel, and A. Selverston. Synaptic modulation of the interspike interval signatures of bursting pyloric neurons. *Journal of Neurophysiology*, 89:1363–1377, 2003.

C. Tallon-Baudry, O. Bertrand, C. Delpuech, and J. Pernier. Stimulus specificity of phase-locked and non-phase-locked 40 Hz visual responses in human. *Journal of Neuroscience*, 16:4240–4249, 1996.

P. Tass. Estimation of the transmission time of stimulus-locked responses: modelling and stochastic phase resetting analysis. *Philosophical Transactions of the Royal Society B: Biological Sciences*, 360:995–999, 2005.

P. Tass. *Phase Resetting in Medicine and Biology: Stochastic Modelling and Data Analysis (Springer Series in Synergetics)*. Springer, Berlin, 2007.

T. Tateno and H. P. C. Robinson. Phase resetting curves and oscillatory stability in interneurons of rat somatosensory cortex. *Biophysical Journal*, 92:683–695, 2007.

B. Telenczuk, V. V. Nikulin, and G. Curio. Role of neuronal synchrony in the generation of evoked EEG/MEG responses. *Journal of Neurophysiology*, 104(6): 3557–67, 2010.

B. Telenczuk, S. N. Baker, A. V. Herz, and G. Curio. High-frequency eeg co-varies with spike burst patterns detected in cortical neurons. *Journal of Neurophysiology*, 2011.

F. Theunissen and J. P. Miller. Temporal encoding in nervous systems: a rigorous definition. *Journal of Computational Neuroscience*, 2(2):149–162, 1995.

P. Tiesinga and J. Toups. The possible role of spike patterns in cortical information processing. *Journal of Computational Neuroscience*, 18:275–286, 2005.

P. Tiesinga, J. Fellous, and T. J. Sejnowski. Regulation of spike timing in visual cortical circuits. *Nature Reviews Neuroscience*, 9(2):97–107, 2008.

R. D. Traub, J. G. Jefferys, R. Miles, M. A. Whittington, and K. Toth. A branching dendritic model of a rodent CA3 pyramidal neurone. *Journal of Physiology*, 481 (Pt 1):79–95, 1994.

R. D. Traub, E. H. Buhl, T. Gloveli, and M. A. Whittington. Fast rhythmic bursting can be induced in layer 2/3 cortical neurons by enhancing persistent Na^+ conductance or by blocking BK channels. *Journal of Neurophysiology*, 89(2):909–921, 2003.

M. Tsodyks and H. Markram. The neural code between neocortical pyramidal neurons depends on neurotransmitter release probability. *Proceedings of the National Academy of Sciences of the USA*, 94(2):719–723, 1997.

M. Tsodyks, T. Kenet, A. Grinvald, and A. Arieli. Linking spontaneous activity of single cortical neurons and the underlying functional architecture. *Science*, 286: 1943–1946, 1999.

M. Valencia, M. Alegre, J. Iriarte, and J. Artieda. High frequency oscillations in the somatosensory evoked potentials (SSEP's) are mainly due to phase-resetting phenomena. *Journal Neuroscience Methods*, 154:142–148, 2006.

C. van Vreeswijk and H. Sompolinsky. Chaos in neuronal networks with balanced excitatory and inhibitory activity. *Science*, 274(5293):1724–1726, 1996.

C. van Vreeswijk, L. F. Abbott, and G. B. Ermentrout. When inhibition not excitation synchronizes neural firing. *Journal of Computational Neuroscience*, 1(4): 313–321, 1994.

W. N. Venables and B. D. Ripley. *Modern Applied Statistics with S*. Springer, New York, 2002.

T. Verechtchaguina, I. M. Sokolov, and L. Schimansky-Geier. First passage time densities in non-Markovian models with subthreshold oscillations. *Europhysics Letters*, 73(5):691, 2006.

J. Victor and K. Purpura. Nature and precision of temporal coding in visual cortex: a metric-space analysis. *Journal of Neurophysiology*, 76:1310–1326, 1996.

J. Victor and K. Purpura. Metric-space analysis of spike trains: theory, algorithms and application. *Network*, 8:127, 1997.

T. P. Vogels and L. F. Abbott. Gating multiple signals through detailed balance of excitation and inhibition in spiking networks. *Nature Neuroscience*, 12(4):483–491, 2009.

H. Webster, I. Salimi, A. Myasnikov, and R. Dykes. The effects of peripheral deafferentation on spontaneously bursting neurons in the somatosensory cortex of waking cats. *Brain research*, 750:109–121, 1997.

G. Werner and V. Mountcastle. The variability of central neural activity in a sensory system, and its implications for the central reflection of sensory events. *Journal of Neurophysiology*, 26:958–977, 1963.

J. A. White, J. T. Rubinstein, and A. R. Kay. Channel noise in neurons. *Trends in Neurosciences*, 23(3):131–137, 2000.

E. M. Whitham, K. J. Pope, S. P. Fitzgibbon, T. Lewis, C. R. Clark, S. Loveless, M. Broberg, A. Wallace, D. DeLosAngeles, P. Lillie, A. Hardy, R. Fronsko, A. Pulbrook, and J. O. Willoughby. Scalp electrical recording during paralysis: quantitative evidence that EEG frequencies above 20 Hz are contaminated by EMG. *Clinical Neurophysiology*, 118(8):1877–1888, 2007.

B. L. Whitsel, R. C. Schreiner, and G. K. Essick. An analysis of variability in somatosensory cortical neuron discharge. *Journal of Neurophysiology*, 40(3):589–607, 1977.

K. Whittingstall and N. K. Logothetis. Frequency-band coupling in surface EEG reflects spiking activity in monkey visual cortex. *Neuron*, 64(2):281–289, 2009.

A. Winfree. *The Geometry of Biological Time*. Springer, New York, 1980.

Y. Yang, M. R. DeWeese, G. H. Otazu, and A. M. Zador. Millisecond-scale differences in neural activity in auditory cortex can drive decisions. *Nature Neuroscience*, 11 (11):1262–1263, 2008.

List of Figures

Acknowledgments

Like every scientists I have done the research presented in this thesis with the hope that someday its results will make a difference. However, the people I could share my thoughts with have already made my efforts worthwhile. I would like to thank them all for their continuous support.

First of all, I would like to thank my two supervisors Prof. Gabriel Curio and Prof. Andreas Herz who believed in me even when I flattered. I am grateful to Andreas especially for showing me that the making of a scientist is not only that of knowledge but also of spirit and Gabriel for taking me on one of the most exciting adventures in my life. I am also obliged to Prof. Richard Kempter who adopted me into his group and provided necessary encouragement in the final period of my studies.

I would like to thank to our experimental partner, Prof. Stuart Baker from Newcastle University, for sharing his data and teaching me how to do experiments and link them with theory. I also profited from the help of my colleagues from Movement Laboratory in particular Karen Fisher, Demetris Soteropoulos, Elizabeth Williams and Claire Witham.

I have been lucky to find myself in one of the most stimulating environments one could think of. I am very grateful to all colleagues from Institute of Theoretical Biology at Humboldt University and Neurophysics Group at Charité where I have found home for most of my studies. In particular, Jan-Hendrik Schleimer, Robert Schmidt, Susanne Schreiber, Henning Sprekeler and Niko Wilbert always provided me with stimulating ideas and extended my horizons. I should never forget the amazing people I shared an office with: Katherina von Carlowitz, Felix Cruetzig, Márton Danóczy, Tommaso Fedele, Marco Hackenberg, Agnes Hahn, Yu Hien, Friederike Hohlefeld and Uwe Röhner. Thank you for making the long overtime enjoyable.

The results presented in the thesis would never be possible without many interesting discussions with my collaborators among them with Vadim Nikulin and Gunnar Waterstraat. I am also grateful to all participants of the Models of Neural Systems course at Bernstein Center of Computational Neuroscience in Berlin and anonymous reviewers of my manuscripts for always demanding more of me.

Last but not least I would like to say many thanks to my close friends who were always there when I needed them: Maria Kramarek, Katrin Krüger, Florian Thiel, Max Homilius, Noam Peled, Sacha Bärtschi, Berit Wenk and many others. I am short of words to say how much I owe you.

I also acknowledge the financial support of two funding agencies: Deutsche Forschungsgemeinschaft (SFB 618, project B4) and Wellcome Trust, UK.

Selbständigkeitserklärung

Ich erkläre, dass ich die vorliegende Arbeit selbständig und nur unter Verwendung der angegebenen Literatur und Hilfsmittel angefertigt habe.

Berlin, den 17. Mai 2011 Bartosz Marek Teleńczuk